A 2D AXIS-SYMMETRIC WOUND ROLL MODEL

INCLUDING NIP EFFECTS

By

CAGRI MOLLAMAHMUTOGLU

Bachelor of Science in Civil Engineering
Istanbul Technical University
Istanbul, Turkey
2002

Master of Science in Civil Engineering
Istanbul Technical University
Istanbul, Turkey
2005

Submitted to the Faculty of the
Graduate College of the
Oklahoma State University
in partial fulfillment of
the requirements for
the Degree of
DOCTOR OF PHILOSOPHY
December, 2009

A 2D AXIS-SYMMETRIC WOUND ROLL MODEL

INCLUDING NIP EFFECTS

Dissertation Approved:

Dr. J. Keith Good
Dissertation Adviser

Dr. Raman P. Singh

Dr. Wei Yin

Dr. Rifat Bulut

Dr. A. Gordon Emslie
Dean of the Graduate College

ACKNOWLEDGEMENT

First and foremost I would like to thank god who gave the strength to complete this study.

I would like to thank my advisor and mentor Dr. J.K. Good not only for his invaluable helps but also his peerless personality and his discretion. Without his understanding and patient this thesis would never be a reality.

I would like to thank for committee members Dr. R.P. Singh, Dr. W. Yin and Dr. R. Bulut for their continuous support and understanding.

I would like to thank Mr. R. Markum for his efforts and patient during experimental works.

I am very thankful to WHRC for supporting my graduate works here in OSU.

I am very thankful to my friends for their helps

I would like to thank my mother and father for their continuous support and love.

Finally I would like to thank my wife Asli for understanding and supporting me with love.

TABLE OF CONTENTS

LIST OF SYMBOLS

A_β	BETA-gage CMD Data Area
AVM	Axisymmetric Wound Roll Model
α, β	Benson's Material Constants
α_i	Angle for i^{th} Contact Node
β	BETA-gage Zigzag Angle
B	Strain-Displacement Matrix
BSM	Beam Spring Model
CMD	Cross Machine Direction
c_i, d_i	Spring Constants
d_{ave}, d_{max}	Average and Maximum Distances Between Consequtive BETA-gage DATA
Δ_i	Lateral Shift of i^{th} Layer due to Oscillation
D	Differential Operator matrix
D_i	Distance of i^{th} Layer
δ_i^s	Gap for i^{th} Contact Node for s^{th} State
E_r, E_θ, E_z	Young's Modulus in Radial, Tangential, CMD Directions Respectively
E	Green-Lagrange Strain Tensor
FEM	Finite Elements Method
F_{nip}	Nip Load
F_c^i	Total Contact Force for i^{th} State

F_j	Nip Load for j^{th} Contact Node
F	Deformation Gradient
G_{rz}	Shear Modulus for r-z Plane
$G_{r\theta}$	Shear Modulus for r-θ Plane
H	Initial Layer thickness
h	Current Layer thickness
h_i	Spring Height for i^{th} Sector
$h_{i,s}$	Layer Thickness for i^{th} Sector's s^{th} BETA-gage
$\bar{h}_{i,j}$	Model Layer Thickness for i^{th} Layer's j^{th} Sector
K_1, K_2	Pfeiffers Material Constants
κ	Proportionality Constant
λ	Wave Length, Parameter
J_θ	Tangential Modulus for Nonlinear Analysis
J_{CMD}	Axial Modulus for Nonlinear Analysis
J_{core}	Core Material Modulus for Nonlinear Analysis
K_e	Element Stiffness Matrix
k_i	Spring Stiffness for i^{th} Spring
L_i	Length of i^{th} Layer
M_e	Element Material Matrix
MD	MachineDirection
N	Normal Force
NIT_j	Nip Induced Tension for j^{th} Sector
n_c	Number of Contacting Nodes

P	Pressure
PK1	1st Piola Kirchoff Stresses
PK2	2nd Piola Kirchoff Stresses
P	1st Piola Kirchoff Stress Tensor
P_0	Initial 1st Piola Kirchoff Stress Tensor
P_O	Oscillation Period
R,r	Radial Positions for Initial and Current Configurations Respectively
$\overline{R},\overline{r}$	Center Radial Positions for Initial and Current Configurations Respectively
r_c	Core Outer Radius
RCM	Roll Compression Model
R	Rotation Matrix
S	2nd Piola Kirchoff Stress Tensor
S_0	Initial 2nd Piola Kirchoff Stress Tensor
T_w	Web line tension
u_e^*	Element Displacement Field Vector
$\vec{u}_e^*$	Nodal Element Displacement Vector
u_i	Radial Displacement for ith node
w_i	Axial Displacement for ith node
θ_i	Orientation for ith Contact Node
X,Y	Initial Cartesian Coordinates
x,y	Current Cartesian Coordinates
η,ξ	Natural Coordinates
σ	Stress Vector

σ_0	Initial Stress Vector
σ_r , σ_θ , σ_z	Stress Components in Radial, Tangential and Axial Directions Respectively
σ_{rz}	Shear Stress
$\nu_{rz}, \nu_{r\theta}, \nu_{z\theta}$	Out-of-plane and in-plane Poisson's Ratios Respectively
ν_{core}	Core Material Poisson's Ratio
ε	Strain Vector
ε_r , ε_θ , ε_z	Strain Components in Radial, Tangential and Axial Directions Respectively
ε_{rz}	Shear Strain
μ	Coefficient of Friction
γ_{rz}	Engineering Shear Strain
Φ	Shape Functions Matrix
ϕ_i	Shape Function for i^{th} Element Node
V_{MD}	Machine Direction Speed
V_{CMD}	Cross Machine Direction Speed
v_c^i	Total Displacement for i^{th} Contact State
w_m	Sector Width
w_s	Sector Width in Beam Spring Model
w_β	BETA-Gage Sector Width
WOT_j	Wound-on-Tension for j^{th} Sector
W_{int}, W_{int}	Internal and External Energy Respectively
δW_{int}	Variation of Internal Energy
δW_{ext}	Variation of External Energy

$D_{\Delta u}\delta W_{\text{int}}$	Directional Derivative of 1st Variation of Internal Energy
z_j	CMD Coordinate for j^{th} BETA-gage Data

LIST OF FIGURES

Figure Page

LIST OF TABLES

Table Page

1. INTRODUCTION

1.1 Description of Subject

Materials which are produced in continuous strip forms are called web materials. Aluminum sheets, newspapers, magnetic tapes etc. are some common samples for web materials. The unique characteristic of web materials' shape makes these materials very flexible. This situation causes difficulties and requires special considerations about production operations, storage and transportation of these materials. The most convenient way to store and transport flexible materials is to wind them. The winding operation forces the flat web material to accept a shell like structure about an axis. This operation, under tension, also forces individual web shells (layers) to interact and form a completely different accretive structure, called a wound roll. In figure 1 a typical wound roll is depicted with its common directions which are used to address various physical quantities:

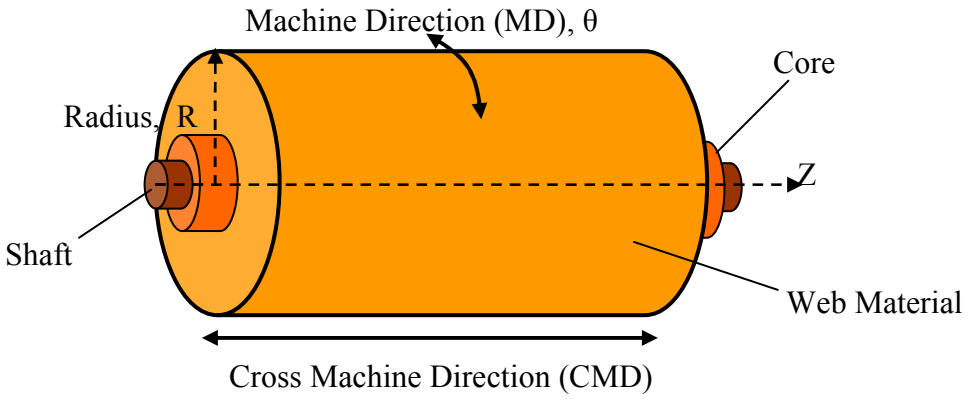

Figure 1. 1 General Wound Roll Layout

The winding operation is done with the machines called winders. There are several types of winders based on the number of drums used. Single drum, multiple drum and belt-reel winders are the most common types. One of the most used of these types is the single drum winder and it can be divided into sub categories depending on the position of application of winding torque. Figure 2 depicts various single drum winding setups with the applied torque and/or nip roller.

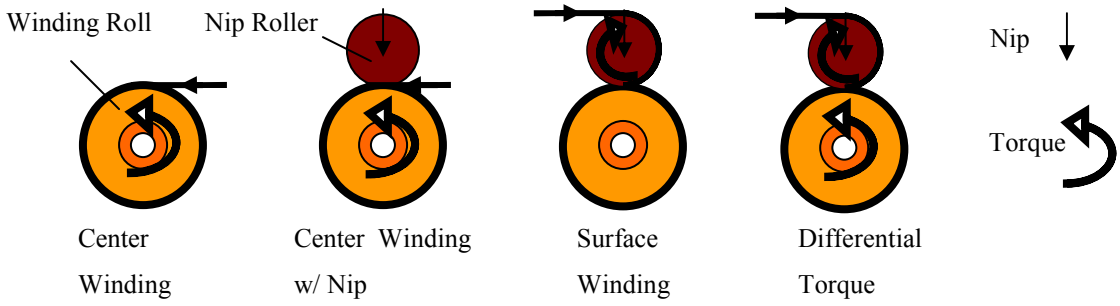

Figure 1. 2 General Single Drum Winding Setups

In the center winding case there is not a nip roller which applies pressure to the outer surface of the winding roll. Thus the torque is applied at the only possible place: the core. Center winding with a nip includes a nip roller pressing to the winding roll but again the torque necessary for winding is applied at the center of core of winding roll. Surface winding has the same setup with center winding but the torque is applied to the nip roller. Finally in the differential torque case, torque is applied both to the core and to the nip roller as seen from the figure. Most of the winding is done with a nip roller for some desired effects of the nip. Two prominent of these desired effects are the exclusion of air during winding and the increase in winding tension in the web beyond the web line stress. These will improve the structural stability and integrity of a wound roll. Regardless of the winding setup used winding introduces stress and displacement fields into the wound roll structure and also changes the response of web material to environmental effects. Moreover because of state dependency of some material properties the situation gets even more complex. Because of introduced stresses and material complexities it is natural that the quality of web material is directly affected from winding. Some of the common types of defects can be seen in the figure 3.

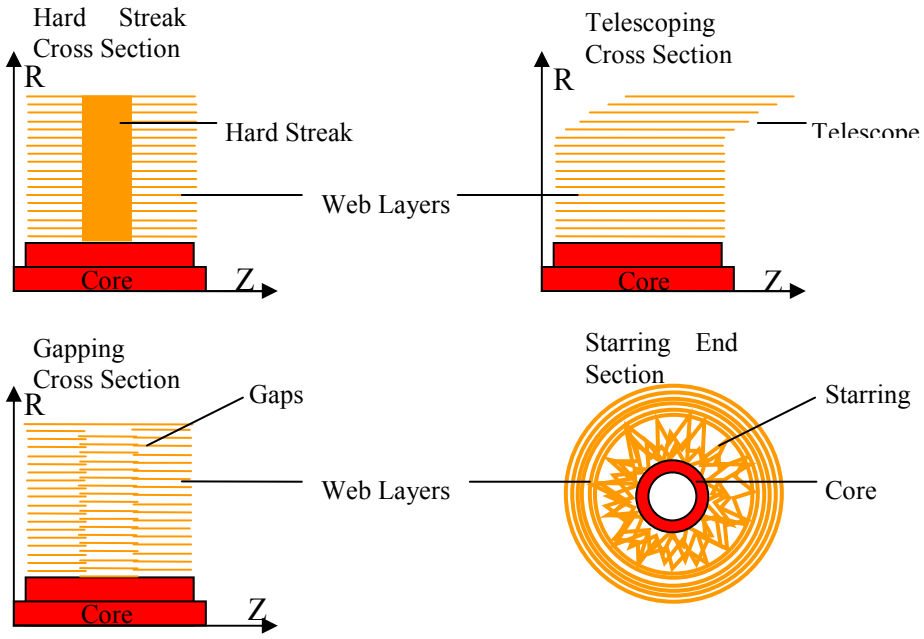

Figure 1. 3 General Single Drum Winding Setups

All of these faults are somehow related with the combined effect of winding parameters, material and geometrical properties of web which forms the wound roll structure. Since these combined effects manifest themselves as stresses and displacements, a clear understanding of physical state of wound roll structure is crucial to prevent faults. A scientific approach requires that stress and displacement fields should be related to the parameters of a roll in an exact and objective manner. This is done via mathematical models. The research field related with wound roll production, transportation and various other related issues is called web handling. Winding mechanics is one aspect of web handling which is a science concerned with the transport of thin media, webs, through web processes where value is added to the web. Wound roll models can be traced back to 40 years ago in the literature [1]. As new stemming ideas have been deduced from

experiments these models have evolved. Today with the help of modern computer technology and advanced numerical techniques one can deal even more complex models which results in huge amounts of calculation. In this situation solution techniques and algorithms directly affect a model's success.

1.2 Scope and Purpose of Current Study

In this study we will develop a consistent and computationally efficient 2D wound roll model which includes the simulation of nip effects. First of all we have extensively studied the validity of small deformation theory for the wound rolls. For this purpose we have developed a very effective large deformation model based on the pre-stress formulation and we have verified our nonlinear model via experiments. We concluded that small deformation theory is valid for web materials.

After verifying that small deformation theory is suitable for general wound roll modeling we have extensively studied elements of a 2D axisymmetric wound roll with nip effects. We have considered that there should be three sub components or models for the complete wound roll model with nip effects. We have decomposed the general model into: 1) a center winding 2D axisymmetric wound roll model (AWM) for the calculation of internal stresses once the tension profile along CMD is given, 2) a wound roll contact model (RCM) which calculates wound roll radial stiffness in an effective and consistent manner once the wound roll properties are given, 3) a nip and wound roll contact model based on a analogy of beam and springs (BSM) which calculates the nip induced pressures versus the CMD once the wound roll profile and radial stiffness along CMD is given. It is known that these nip induced pressures can increase the winding tension and

thus the three models must interact with each other. We have identified three steps towards the final goal:

In the first step we have completed a pre-stress formulation for center winding simulations of 2D axisymmetrical wound rolls. The 2D model (AWM) we have developed can simulate geometrical and material non-uniformities along CMD in case of center winding only. This model is verified by comparing with the literature. The second step completed in this study is a consistent and efficient contact model for the wound rolls pressed under a nip. We have utilized a plane stress finite element formulation which can account for material nonlinearity for the contact analysis of nips with wound rolls. Contact stresses and deformations developed in the wound roll are calculated in a very effective manner. These results are then used to calculate the nonlinear radial contact stiffness of wound rolls. A curve fit is done with 2nd order polynomials to characterize the radial contact stiffness. This model (RCM) is also verified via experiments. The third step done is the completion of a beam – spring analog model (BSM) of the contact of a wound roll and nip. In this model we have represented the wound roll and nip as beams which are composed of linear beam elements and the radial stiffness of wound roll via springs with nonlinear characters which resulted from the second step. In this model the contact pressures between the nip roller and the wound roll are calculated across the roll width (CMD) for the given spring properties and wound roll geometrical and material properties

It should be understood that these sub components work together in a recursive manner for the simulation of nip effects on the wound rolls as shown in figure 4. The AWM provides internal stresses and the roll radius profile for the RCM and BSM. The RCM

computes constants of springs along CMD for the nonlinear radial characterization of the wound roll. The BSM provides the nip induced pressures versus the CMD for a given total nip load. The nip induced pressures profile is received by the AWM and then used to calculate wound-on-tension versus CMD location and then computes internal stresses. Together these 3 models produce a computational algorithm which can simulate winding with a nip roller.

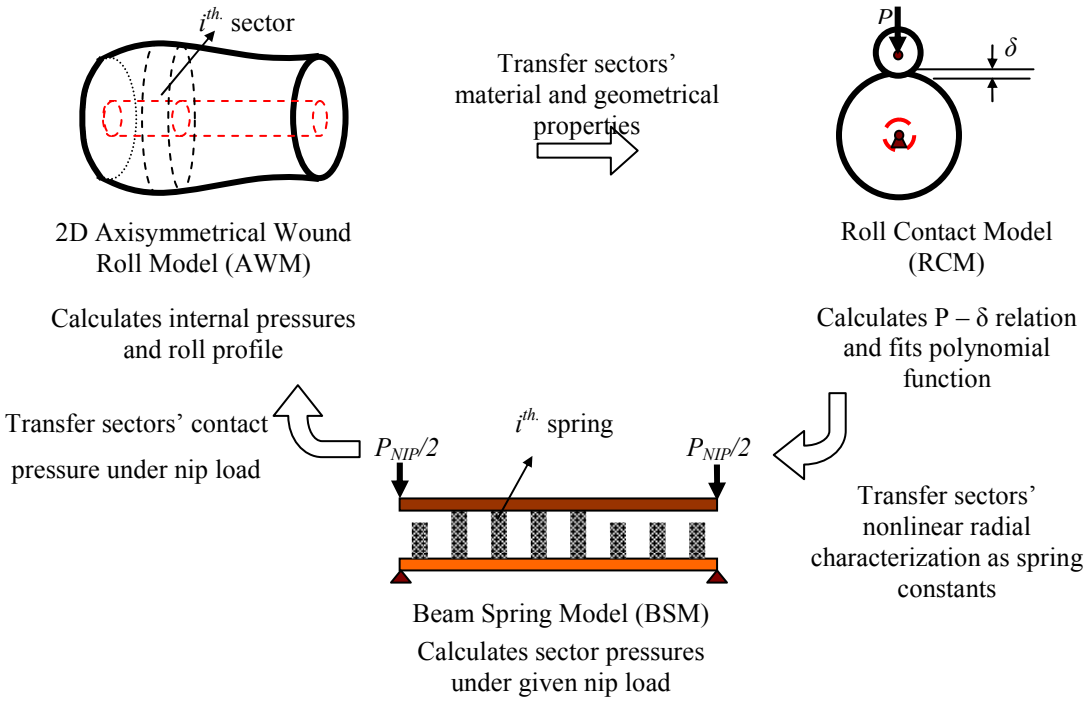

Figure 1. 4 2D Wound Roll Model w/NIP Decomposition

2. LITERATURE REVIEW

2.1 Review of Previous Works

Wound roll models begun to appear 40 years ago. These early models appeared as 1D models with radial variation only. Gutterman [1] and Catlow & Walls [2] were initial works. In these models analytical methods were employed for calculation of internal stresses of a wound roll. They were assuming a linear isotropic material and used stress formulas developed from the elasticity solutions of thick cylinders. The solution procedure of these models directly resembles the accretive structure of a wound roll. Instead of the actual spiral form the wound roll was considered as a stack of concentric cylindrical layers. During winding a layer they represented the roll with a thick elastic cylinder and they represented the winding layer with a thin elastic layer. This thin elastic layer's tangential stress was taken to be equal to web line stress. Using thin pressure vessel formula (1) a corresponding radial pressure (Pout) was calculated. This pressure was then used as an input for the thick elastic cylinder formulas as outer surface pressure type boundary condition. The formulas provided the incremental stresses occurring at certain radial positions due to that particular layers addition (pressure increment effect). Finally they summed all incremental stresses for a generic point to find the total stress of that point.

$$P_{out} = \frac{T_w h}{r} \tag{2.1}$$

Early 1D models were good at capturing the accretive behavior of a wound roll but they lack the required material complexity because of the anisotropy and radial nonlinearity. Later Pfeiffer addressed radial nonlinearity of wound roll material in a cornerstone study [3]. He conducted stack compression experiments with web materials and produced his widely used nonlinear material model. From the stack tests he concluded that radial pressure at a point is linearly related with the radial modulus of that point:

$$E_r = K_2(P + K_1) \tag{2.2}$$

Here K_1 and K_2 are material specific parameters obtained by curve fitting to the experimental data. P is the pressure applied on the stack. Pfeiffer also conducted sound experiments with the rolls in order to measure in roll stresses. Although he addressed the general form of stress distributions he was unable to rigorously predict the stresses according to roll's geometrical, material parameters and winder operation conditions. In another study Altmann [4] considered the effect of anisotropy. He considered basic linear elasticity equations for thick cylinders and modified them for anisotropic materials. He derived two expressions: one for radial pressure and the other for hoop tension. He applied the same principles of linear isotropic model but because of anisotropy at the summation procedure of the incremental stresses, he came up with closed form integrals. These integrals are appeared impossible to compute for some combination of anisotropic constants and a numerical analysis at the time of the study were not available or feasible due to lack of efficient computers. Although Altmann's study was rigorous because of the

above limitation he was not able to produce accurate results. This situation leaded to some misunderstandings. Yagoda [5] found that radial and circumferential stresses change sharply near the vicinity of the core and he concluded that Altmann did not take into account core's effect but this was not true. Altmann's analysis included both deformation compatibility and pressure equilibrium at the core surface. Nevertheless Yagoda produced a non dimensional version of Altmann's model and he applied hyper-geometric series for solution. This approach was very efficient especially if the web tension is expressed as a polynomial function of radius. Due to this method it is sufficient to produce accurate results up to 7 decimals with retaining only a few terms of the hyper-geometric series. Modeling considerations for anisotropic linear materials continued. Recently Burns et al [6] derived a linear anisotropic model. Their formulation was similar with Altmann's except they used a different outer boundary condition. They assumed that in-roll stresses are caused by residual strains. They claimed that tensioned layers are relaxing in the wound roll and resulting in the stress developments in the rolls. Their results were different from the results derived by using Altmann's model. Their model was showing over relaxation of tangential stress of roll's outer layer. They argued that this was the result of compressibility of wound roll. In a previous study [7] we have carefully derived their model and test for extreme cases. We input a very high radial modulus of elasticity which will prevent the compressibility and will cause the web to act as rigid. Their model still showed considerable relaxation which was not physically expected. We concluded that Altmann's outer boundary formulation is more realistic. One of the most important steps in the wound roll modeling history was Hakiel's work [8]. He developed a nonlinear anisotropic model. He used Altmann's formulation and

incorporated Pfeiffer's nonlinear material model. He obtained a second order differential equation in terms of incremental radial stresses:

$$r^2 \frac{d^2 \delta\sigma_r}{dr^2} + 3r \frac{d\delta\sigma_r}{dr} - \left(\frac{E_\theta}{E_r} - 1 \right) \delta\sigma_r = 0 \tag{2.3}$$

Since this is a 2nd order differential equation it is required two boundary conditions for the solution so he utilized outer and inner boundary conditions like Altmann: The outer boundary condition comes from the thin pressure vessel formula

$$\delta\sigma_r \big|_{r=s} = -\frac{T_w \big|_{r=s}}{s} h \tag{2.4}$$

The inner boundary condition is the compatibility of the deformation of the core and first layer of wound roll:

$$\left. \frac{d\delta\sigma_r}{dr} \right|_{r=r_c} = \left(\frac{E_\theta}{E_c} - 1 + \nu_{r\theta} \right) \left. \frac{\delta\sigma_r}{r_c} \right|_{r=r_c} \tag{2.5}$$

Here E_c is the core stiffness and can be calculated by thick cylinder formulas for any given geometry and linear anisotropic material. The pressure dependent E_r renders the differential equation intractable with analytical methods so Hakiel employed a finite difference scheme. His algorithm was simply following the steps in order: Solving numerically the problem of addition of a layer, computing the incremental stresses due to addition of the layer, summing incremental stresses with previous total stresses to obtain current total stresses and finally updating material properties due to current total stress state. This procedure is applied until all laps are wound. Hakiel verified his model with

experiments and obtained much better agreement when compared with linear models. Hakiel's model is producing quite acceptable results for hard (high K_2) materials. When soft materials are encountered Good et al [9] showed that experimental pressure data is considerably lower than the Hakiel's model's output. They argued that this was due to outer layer's relaxation because of the significant compaction of the soft wound roll. Good et al modified Hakiel's thin pressure vessel type outer boundary formulation by incorporating the tension loss which is caused by relaxation:

$$\delta\sigma_r\big|_{r=s} = -\left(T_w + \frac{u}{s}E_\theta\right)\frac{h}{s} \tag{2.6}$$

Here u is the radial deformation at the current outer radius (s) of wound roll. This is divided by s in order obtain strain loss term. The strain loss term will give the stress loss when multiplied by tangential modulus (E_θ). The loss term is summed with web line stress T_w because u is always negative (radially inward). Good et al conducted experiments and verified their model. Another study concerning compaction of the wound rolls is the work by Benson [10]. Benson produced a 1D material and geometrical nonlinear formulation based on continuum mechanics and solved the resulting equations in the same way as Hakiel did. He derived a nonlinear material model which was based on Pfeiffer's material constants. He also neglected the Poisson's ratio ($v_{r\theta}=0$) so that his material model became suitable for numerical analysis (finite difference) he employed. In his material model he replaced linear strains with log strains and ended up with two

constants α and β which were counterpart to Pfeiffer's constants K_1 and K_2. His constitutive model for radial direction was:

$$P = \alpha\left(\left(\frac{X}{x}\right)^{\beta} - 1\right) \tag{2.7}$$

Where X is unloaded stack height and x is the stack height under pressure level P. Although his mathematical formulation is straight forward he did not give any information about how to find or derive α and β when K_1 and K_2 is given. This is important because Pfeiffer's method is the most common among other characterizations. We have derived his model and coded in the background of VBA Excel. The code gives the same results when the given α and β is used. We also developed a curve fit algorithm for the derivative of radial modulus to find α and β from given K_1 and K_2 .This issue will be discussed in detail in chapter 2 where we discussed geometrical nonlinearity. Benson also produced results which were in good agreement with Good et al's results.

Other modeling considerations in 1D model arena mainly deal with adapting the models for analysis of environmental effects such as relaxation[11], thermal[12] or for analysis effects of air entrapment [13]. There are also 1D models which take into account nip effects [14]. We will talk about the 1D winding model with nip in detail in the following pages where we gave the literature for the nip mechanics.

We see that additional efforts in one dimensional modeling which dealt with geometrical nonlinearity [9], [10], material relaxation effects [11], air entrapment effects [13], centrifugal [15], [16] and thermal effects [12] are mainly built on the structure of

previously mentioned two important studies [3], [8]. While all of these efforts were major successes in understanding the state of wound roll and they truly give an insight in one dimension for different situations (relaxation, air entrapment etc.) it is obvious that one dimensional models can only capture variations in the state of wound roll with radial position. When cross web non uniformities become important and/or physical models dictate finite widths for wound roll (for example air leakage from sides of wound roll) one dimensional models simply become insufficient and one of the earlier assumptions, plane elasticity, must be removed. This means in this case we are modeling wound roll as a cylinder with finite width. A very limited number of existing wound roll models [17], [18], [19], [20],[21] fall in this category and they are called two dimensional models since they allow stress variations in two dimensions; across finite width (CMD) and radial directions. Thus in theory they can incorporate any kind of cross web non uniformity and mostly they deal with cross web caliper variations which is generally most common and important situation when cross web caliper non uniformities are length wise persistent. Early two dimensional models [17], [18] in fact, might be described as pseudo two dimensional models because they consider roll's finite width with segmentation to thin slices and treating each slice as a discrete one dimensional model. This is an approximation because it neglects displacement continuity across the slices and it is not able to threat wound roll as a whole. The web tension is allocated as a function of the radius of the outer layer which is a function of the widthwise location and the mechanical equilibrium at the current outer layer. These early models mainly differ in the method of allocation of the tension at the outer layer. In his formulation Hakiel [17] introduced the notion of relaxation radius: the radius at which the layer of web has zero

tension. This layer is expanded through roll profile and then allowed to shrink fit over the roll. Hakiel considered n sectors along CMD which were modeled with 1D models. He calculated the tangential strain of the $i^{th.}$ sector using the unknown relaxation radius (r_o). The tangential force contributions (T_{wi}) were then calculated and summed in order to obtain the total tangential force which in turn should be equal to web line force (T_w) because of the mechanical equilibrium:

$$T_w = \sum_{i=1}^{n} T_{wi} = \frac{Ebh_{avg}}{n(1-\nu^2)} \sum_{i=1}^{n} \frac{r_i - r_o}{r_o} \tag{2.8}$$

Here r_i is the outer radius of the $i^{th.}$ sector. If the calculated total tangential force is greater/smaller than the given web line force then a greater/smaller relaxation radius should be selected for less/more compression. The process of finding the correct relaxation radius which will put the layer in mechanical equilibrium turns out to be an iterative procedure. After the correct value for the relaxation radius is found tangential stresses for each sector can be directly calculated and these values can be used in corresponding 1D models. Hakiel also calculated incremental strains and then calculated incremental radial displacements by integrating them. These incremental radial deformations were then used to update the roll profile. Kedl's [18] method for allocating tension across the roll was based on the fact that roll has a constant angular velocity through CMD. His first estimate was of the form:

$$T_{wi} = E_\theta \left[1 - \frac{r_{avg}}{r_i} (1 - \varepsilon_{avg}) \right] \tag{2.9}$$

Where

$$\varepsilon_{avg} = \frac{T_w}{AE_\theta} \tag{2.10}$$

and r_{avg} is the average roll radius. Summing up the contributions from all sectors Kedl obtained total tangential force. Since r_{avg} and r_i are changing due to deformation total force will not be equal to given web line force. Thus this procedure requires an iterative approach like Hakiel's. The output of the pseudo two dimensional models developed by Cole and Hakiel [17] and Kedl [18] were limited to the outputs of the one dimensional models they employed. Thus the outputs of these models were the radial and circumferential stresses which were now known as a function of radius and across the web width in sectors represented by the series of one dimensional models. When modeling web thickness variation across the web width the web would be divided into sectors of equal width. Thickness profiles would then be averaged within the sector to provide a sector web thickness which could be input to the one dimensional winding model for that sector. If these average thicknesses were rearranged the stresses output would be identical but also rearranged in the same manner. Thus the value of the pseudo two dimensional models was in determining the maximum and minimum pressures and circumferential stresses within a roll and then relating these stresses to associated defects. For instance localized blocking could be predicted due to localized pressures in excess of the blocking pressure. Local yielding of the web could be predicted if the circumferential stresses exceeded the yield stress of the web. As mentioned before an artifact of employing multiple one dimensional models was that the radial continuity of a web layer was not ensured between the sectors. The deformed radial locations of the layers computed were at assumed to exist at the widthwise center of each sector. Hakiel

designed a segmented core in which each segment was instrumented with strain gages such that the pressure between the first lap and the core could be monitored throughout the winding. He also developed a device for measuring the radial location of an outer lap across the width of a roll. The segmented core was a deviation from the cores used commercially that are continuous across the roll width. It could be argued that a segmented core was the best means of verifying a pseudo 2D model [37]. As mentioned previously these models provided no assurance of radial continuity of a layer but nor did they assume continuity of the core.

Later two dimensional models [19], [20], [21] removed this approximation by using more powerful modeling and solution techniques. They use the Finite Element Method (FEM) and conveniently represent wound roll geometry in two dimensions with axisymmetric formulations. This advanced treatment requires more efficient solution algorithms in order to model effects of cross web non uniformities (existing models only dealt with caliper variations and CMD stiffness variations) with desired accuracy in a reasonable time. The FEM formulation which Lee and Wickert [19] developed can model the roll in two dimensions and can give stress concentration effects due to core and web CMD stiffness variations. In the case of cross web thickness variation it is assumed that current roll profile of the radius of the outer lap across the width does not have any effect on tension variation in the incoming layer. This assumption clearly contradicts experimental studies [22]. Later Hoffecker and Good [20] developed a comprehensive two dimensional model in which they considered that current roll profile effects tension allocation in the outer layer. Their model and code is very capable but it is not computationally efficient and robust. They used multi point constraints (MPC) in order to shrink fit an outer layer

on the roll. MPC requires that additional dof to be introduced hence solution times become longer. Also Hoffecker's code was developed in Fortran which is not considered user friendly in terms of common industrial usage. There is a need to develop more efficient axisymmetric models with more robust algorithms in user friendly environments. In chapter 3 a pre-stress type formulation based on a novel axisymmetric finite element wound roll model will be introduced. The most recent 2D wound roll model using axisymmetric finite elements were due to Arola [21]. He developed a large deformation type 2D model. In his work he adopted Total-Lagrangian approach with Newton-Raphson algorithm for the solution of nonlinear equations. Arola's material model is based on Pfeiffer's nonlinear model. Pfeiffer's model uses engineering stress and strains for the calculation of K_1 and K_2 where as Arola is using 2nd Piola-Kirchoff stresses and Green-Lagrange strains in his formulations. Using material models developed for linear elasticity in the nonlinear formulations is not consistent [36]. We have developed a simple and effective large deformation model and also coded Arola's material model for the comparison issues in the chapter 2. In this context we also compared results of Hakiel's original model, Benson's large deformation model and a linear tension loss model based on pre-stress formulation. Finally we concluded that the geometrical nonlinearity can be modeled with a linear tension loss model hence 2D axisymmetric models based on tension loss are valid.

One of the complicating effects in winding is that of a "rider" or "nip" roll. The primary effect of nip roll is the increase of the outer layer's tension beyond the incoming web line tension [23], [24]. This increase is called nip induced tension and abbreviated as NIT. The total tension of the outer layer can be found by simply summing web line tension and

the NIT and it is called wound on tension or abbreviated as WOT. In the absence of NIT WOT will be equal to web line tension. A more precise definition for WOT would be that it is the outer layer's final level of tension. Almost all winding models discussed previously apply only center winders which are forming a small group. By far the largest group of winders has some sort of a nip roller impinged into the winding roll. There are two main reasons for this application. First winding with a nip decreases the amount of air that is entrained and second it increases the tension in the web above the incoming web line tension thus increases the final product's structural stability and integrity [22]. One of the earliest models in order understand NIT development mechanism is due to Good and Wu [25]. They used a finite element model to show that NIT was the result of MD strains developing in the outer layer as it passes through between the nip and winding roll. Early suggestions for the calculation of the nip were based on Amontons-Coulomb law of friction (ACLF) [14].

$$NIT = \mu N \tag{2.11}$$

Where μ is the coefficient of friction and N is the nip induced pressure. Experimental studies showed that this approach is valid up to a level of nip load [25]. Later some theoretical studies clearly indicate that a more sophisticated analysis is required for the calculation of NIT because of the slip and stick zones which are developing between outer layer and beneath layer [26], [27]. Most recently Kandadai [28] removed the restrictions of the previous analytical works by employing commercial finite element software ABAQUS. He verified his findings with experiments. He concluded the validity of the Amontons-Coulomb law of friction (ACLF) for small to moderate nip loads. For high nip loads he found that ACLF yields higher NIT because of the stick zones. Finally

Good [22] concluded that expressions based on ACLF may work well for a generic web up to a nip load level. Unfortunately for the generic web this load level is not known and also sophisticated approaches based on contact mechanics are required beyond this level. It was natural that NIT calculations were coupled with winding models to investigate the nip effect on the stress field of a roll. Good et al [14] incorporated an ACLF based model with the Hakiel's center winding model [8]. They modified the outer boundary condition by simply adding NIT to present web line stress. Hakiel's outer boundary condition was modified using kinetic coefficient of friction of web/web μ and nip pressure N:

$$\delta\sigma_r\big|_{r=s} = -\left(T_w + \frac{\mu N}{h}\right)\frac{h}{s} \tag{2.12}$$

Thus they obtained nip effect. They verified their model with experiments done with winding polypropylene film, rolls of light weight coated paper. In another study [29] it is shown that this approach also worked well for bond paper. Good et al's model was a 1D model which can only simulate nip effects through radial direction. In the 2D model arena there is only Hoffecker's model [30] which incorporates nip effects. Hoffecker expanded his base axisymmetric model for nip contact analysis. He also assumed the ACLF approach of Good et al when calculating the NIT. Since his model was a 2D model it was expected to include NIT CMD nonuniformities (i.e. NIT is changing as a functions of CMD position). Hoffecker was using quadrilateral elements for his axisymmetric model. he considered each stack of quadrilateral elements in radial direction as a sector and he assumed that NIT was constant over a sector. The problem here is that for the NIT calculation at a sector, the amount of average nip pressure (N) occurring at that sector should be calculated first. This is clearly a contact problem

between nip roll and winding roll at every instance of winding. Hoffecker assumed that peripheral contact will remain same because nip is contacting at every angle as the roll is rotating. Thus taking into account axisymmetry he simplified the 3D problem of contacting cylinders to a 2D counterpart: problem of a beam on elastic foundation. In this 2D representation he represented the bending stiffness characteristics of wound roll and nip roll with beams and he used Winkler foundation springs attached to the roll beam in order to represent the radial stiffness characteristics of the wound roll. He employed FEM for solution of the representative 2D beam on foundation model and obtained CMD pressure profile to use in NIT calculation. The crucial point here is to obtain spring stiffness representation of the Winkler foundation because the radial response of wound roll is nonlinear. He adopted the theoretical work of Hertzian contact which is given in Johnson [31] for the calculation of nonlinear spring stiffness. When modeling nip roll and nonlinear wound roll contact analytical Hertzian approach and Winkler foundation representation were providing the simplicity for the coupling with an axisymmetrical model but they were also considered as severe idealizations. A real contact analysis of two cylinders which will be based on numerical analysis and which will take into account nonlinear radial stiffness characteristic of wound roll would be much more accurate and consistent. This should be done in such a way that the resulted approach should be sufficient to catch the real behavior (verified by experiments) but also it should be computationally efficient and compatible for implementation with a winding model. In chapter 5 a material nonlinear model which is consistent for wound rolls will be incorporated in 2D contact analysis of a wound roll and a nip. Also experimental verification will be shown. In this way consistent and accurate representation of a wound

roll's radial stiffness is obtained.

2.2 Summary

Up to date 2D axisymmetric formulation of wound rolls remains matchless in terms of numerical stability, usage simplicity and effectiveness. Although there are sophisticated 3D models which require expensive and complicated commercial software packages they are far from being optimal for industrial simulation purposes. 2D axisymmetric formulations can realistically model basic features of a generic wound roll model such as material nonlinearity and CMD nonuniformities. There is currently only Hoffecker's model which truly incorporates material nonlinearity and CMD nonuniformities in a realistic manner. Hoffecker uses multi point constraints (MPC) in his formulation. It is well known that MPC type formulation not only affects stability because of its complicated nature, it also increases the number of dofs significantly hence the computational time becomes costly. In the competitive industrial environment quick solutions to the simulation problems are very valuable. Thus model development research has also a great tendency in rendering numerical algorithms, solution techniques more effective. It can be said that model developments should also continue in terms of computational efficiency and robustness. A new compact, faster, robust and effective 2D axisymmetric model based on novel formulations would be greatly appreciated in the web handling industrial community.

Most of the wound rolls are wound by the winders occupied with nip mechanisms. Thus the combination of a 2D axisymmetric wound roll model including nip effects would be a very important and useful instrument for understanding of various physical quantities of a

wound roll wound with a nip. Again only available model is due to Hoffecker. Hoffecker's model can be decomposed into three sub models. These are:

1. A 2D axismmetrical base model based on MPC formulation which computes in-roll stresses.

2. A model calculating the radial stiffness of wound roll versus CMD. The radial stiffness of wound roll versus CMD is calculated from the Hertzian contact theory of elastic cylinders and material nonlinearity is incorporated with the nonlinear radial modulus. The output of this model (radial stiffness) is used as input in the beam on elastic foundation contact model.

3. A 2D contact model based on beams on elastic foundation formulation. This model again uses MPC formulation for the modeling of the contact between roll beam and nip beam and it calculates contact pressures versus CMD for a given total nip load.

Structurally this decomposition seems to be an optimal definition of a realistic wound roll model with nip effects. However for a total realistic, efficient and robust model these sub components should also be realistic, efficient and robust. We have talked about the first component: base model and disadvantages of MPC formulation. The second component: 2D contact model based on beam on elastic foundation formulation uses an iterative procedure in order to calculate contact pressures versus CMD. In the iterative solution procedure total nip load is divided into equal portions and thus load levels are formed. In every step the system is solved and updated for a load level towards final load. Once the convergence obtained the algorithm moves to next load level. This is a complicated and

time consuming process. A new type of algorithm which is faster and more reliable would be much more effective. The third component is the most crucial part of the combined model because it strongly affects the calculation of the nip induced tension. In this part Hoffecker considered nip roll and wound roll as isotropic cylinders under the conditions of Hertzian contact theory. He utilized this theory to define the relation between load and deformation for the compression of isotropic cylinders. He incorporated radial nonlinearity by simply using nonlinear radial modulus of the wound roll in the expressions derived for linear elastic materials. In reality the wound roll is not isotropic and it is not linear elastic. His formulation also lacks the effect of radii of cylinders because his load deformation relation does not include any terms related with geometrical properties of cylinders. He also did not verify his radial stiffness model as a standalone model. A more realistic radial stiffness analysis which takes into account the orthotropic properties and real contact conditions between nip cylinder and roll cylinder would be much more accurate in the calculation of the nip pressure versus CMD. This analysis should also directly take into account the nonlinear radial character of the wound roll.

2.3 Research Objectives

In this study the focus area will be the development of a more realistic and efficient combined 2D axisymmetrical model including nip effects. As in Hoffecker's model the combined model will be formed up with three components:

1. A stand alone 2D axisymmetric wound roll model which is based on pre-stress type formulation thus avoiding cumbersome and time consuming MPC type

formulation.

2. A model calculating radial stiffness of the wound roll. This model's output will be the nonlinear spring stiffness parameters for the beam spring model. The model is based on finite element formulation of the contact of two orthotropic cylinders. The cylinder representing the wound roll will have material nonlinear character. Since this is an actual numerical contact simulation the effect of geometrical properties of cylinders will be truly reflected in the radial stiffness analysis. Finally the same quasilinearization technique will be employed for rapid solution.

3. A beam and spring model which is a representation of the contact of a nip and a wound roll. In this model wound rolls radial stiffness are represented with nonlinear springs along CMD and also the nonuniform roll profile of the wound roll is taken into account. A very compact and efficient algorithm based quasilinearization is applied for rapid solution instead of time consuming iterative procedures.

These fundamental elements for the proposed combined model will be explained in detail in the subsequent chapters:

- In chapter 3 we will derive a compact fully nonlinear formulation and compare results with experimental tests. We will show that small strain based formulations are valid for axisymmetric wound roll modeling.

- In chapter 4 a pre-stress type formulation based on small strain assumptions of linear elasticity will be developed. We will show that the new formulation, when combined with 2D axisymmetric finite element

formulation, results in a faster and reliable 2D axisymmetric wound roll model (AWM). The new model's results will be compared to existing literature for verification.

- In chapter 5 a realistic radial stiffness calculation method will be demonstrated. Nip and wound roll cylinders will be modeled with plane finite elements and their geometrical and material properties will be truly reflected in the contact analysis. A very simple and efficient algorithm based on quasilinearization will be explained. The results of this model (RCM) will be verified by comparing with experimental data. Also the effect of radii of the nip and wound roll will be showed.

- In chapter 6 an analog beam spring model (BSM) for the calculation of the nip induced pressure versus CMD will be given. A simple and very effective algorithm based on quasilinearization will be produced. Consistent results of the algorithm will be showed.

- In chapter 7 an efficient wound roll model with nip effects, which is a combination of the works done in previous chapters, will be proposed.

- In chapter 8 experimental verification of the model is provided. The methodology of the experimental work is given and the results are discussed.

- In chapter 9 final conclusions are made. Also potential future research directions are pointed and recommendations are given for the research area

3. LARGE DEFORMATION WOUND ROLL MODELS

Material characteristics of webs play an important role on the final state of the wound rolls. Among other parameters which are dictating hardness of the roll, radial compressibility dramatically affects the physical state of the wound roll via controlling the radial pressures. Radial pressures between layers should be low enough to avoid material damage and collapse but also they must be high enough to maintain wound roll structural integrity and stability. Thus a precise knowledge of pressures is important. [22]

Most of the web materials exhibit nonlinear character along the radial direction. Material models incorporate this nonlinearity by defining radial modulus of elasticity dependent on radial pressure. One of the most widely accepted model is Pfeiffer's [3]. He defined two material constants (K_1, K_2) to model the radial material response:

$$J_R = K_2(P_R + K_1) \tag{3.1}$$

Here P_R ,is the radial pressure which is taken positive and J_R is tangent radial modulus. As seen from the relation initial modulus is given as K_1K_2 and the springiness can be represented by K_2 . Also it is easily understood that as the parameters increases hardness/rigidity will also increase. This material nonlinear model can be used with the linear balance (equilibrium) laws of elasticity by employing iterative solution techniques based on layer-wise analysis of wound roll.

Linear balance laws are always written and solved over the initial configurations of mechanical systems. Hence if the displacements and/or strains are small one can always employ this type of formulation. Linear elasticity or so called small strain assumptions are considered to be valid or good approximations up to %1 strain. Above this value one should incorporate a formulation which takes into account the deformed shape of the body. This type of problems need special considerations and generally called geometrically nonlinear problems. This is because the final geometry or the configuration of the mechanical system is not known a priori. This final configuration is also one of the unknowns of the problem along with the stresses.

Web materials with low K_1 and K_2 values exhibit significant radial compaction during winding. Meanwhile radial strains are usually getting bigger than %1. Depending on the winder parameters typically values smaller than (10,2) for (K_2 , K_1) results in the above situations. In this perspective wound roll models using linear balance laws become insufficient and one should take into account additional considerations related with the geometrical nonlinearity for realistic modeling. In this study we will demonstrate a simple and efficient finite element method which takes into account material nonlinearity as well as geometrical nonlinearity. We will compare existing approaches to the problem and finally discuss the importance of the phenomenon.

3.1 Nonlinear Geometrical Formulation

We will introduce a reduced 2x2 finite element which can be used in the modeling of geometrical and material nonlinear phenomena in axisymmetrical analysis. The starting point of development is the virtual work expression. This can be stated as the equality of virtual internal and external works for all configurations:

$$\delta W_{\text{int}} = \delta W_{ext} \tag{3.2}$$

For the current configuration the internal virtual work can be given as the virtual works of real or true or Cauchy stress field over the virtual strains:

$$\delta W_{\text{int}} = \int_v \delta\varepsilon^T (\sigma - \sigma_0) dv \tag{3.3}$$

Here $\delta\varepsilon$, σ , σ_0 are virtual strain vector, current Cauchy stress vector and Cauchy counterpart of the initial stress vector respectively. The integration is done for the current configuration. External virtual work can be given as the sum of external forces' works over corresponding virtual displacements:

$$\delta W_{ext} = \int_v \delta u^T b \; dv + \int_a \delta u^T q \; da \tag{3.4}$$

Here *q* is the external distributed loads acting over surface element and *b* is the body force component acting over volume element. In the nonlinear geometrical analysis there is a certain difference between the various configurations of the body. Thus we have to take in to account the deformation of the system and define the physical quantities according to a selected configuration. As mentioned before above virtual work expression is written for the current configuration. Hence the stresses are Cauchy stresses and the

strains are small displacement strain components which are work conjugate of each other. One of the most common virtual work structures for the nonlinear finite element analysis is to write virtual work expression in terms of initial coordinates. If we convert above virtual work expressions we get the following counterparts for the initial configuration:

$$\delta W_{\text{int}} = \int_V (S - S_0) : \delta E \; dV \tag{3.5}$$

$$\delta W_{\text{int}} = \int_V (P - P_0) : \delta F \; dV \tag{3.6}$$

$$\delta W_{ext} = \int_V \delta u^T B \; dV + \int_A \delta u^T Q \; dA \tag{3.7}$$

Here the majuscule indexes denote that the quantity is written in terms of initial coordinates i.e. *v* is for current and *V* is for initial volume. Generally there are two forms for the initial counterpart of the internal virtual work expression. During first transformation (3.6) from current to initial coordinates the Cauchy stresses (σ) are converted to 1st Piloa-Kirchoff stresses (*P*) and the small strains (ε) are converted into deformation gradient (*F*). The second transformation (3.5) turns Cauchy stresses to 2nd Piloa-Kirchoff stresses (*S*) and small strains to Green-Lagrange strains (*E*). These two transformations are identical to each other but they have own advantages. For example while first transformation is allowing simpler numerical formulations the second protects symmetry in numerical formulations. In order to facilitate derivations, we have written the internal work expression as an inner product of stress and strain tensors rather then the previous vector multiplication employed for the current configuration. Since the current configuration is unknown the virtual work expression is highly nonlinear in terms

of displacements. In general it is impossible to find an analytical solution for the nonlinear virtual work expression so it is linearized in terms of displacements and iterative techniques are employed. The linearization is carried out by means of directional derivative which is based on the notion of Taylor series expansion in multiple dimensions. Both internal and external work may depend on displacement field and also the stress strain relations may be nonlinear as in the example of web materials. Considering this fact we can write internal and external forces as a function of displacement field u:

$$\delta W_{\text{int}} = \delta W_{\text{int}}(u), \delta W_{ext} = \delta W_{ext}(u) \tag{3.8}$$

Taking the directional derivative of $\delta W_{\text{int}}(u)$ $\delta W_{ext}(u)$ in the direction of u we obtain

$$\delta W_{\text{int}} + D_{\Delta u}\delta W_{\text{int}} = \delta W_{ext} + D_{\Delta u}\delta W_{ext} \tag{3.9}$$

Here directional derivative is given as:

$$D_{\Delta u}\delta W = \left.\frac{d\delta W(u+\lambda\Delta u)}{d\lambda}\right|_{\lambda=0} \tag{3.10}$$

After rearranging the virtual work expression, we arrived at the linear form in terms of incremental displacement vector Δu :

$$D_{\Delta u}\delta W_{\text{int}} - D_{\Delta u}\delta W_{ext} = -\delta W_{\text{int}} + \delta W_{ext} \tag{3.11}$$

The right hand side is known for a given configuration i.e. for a given field u and we will show explicitly the left hand side is linear in terms of unknown incremental displacement vector Δu .This can lead the solution for incremental displacements and after updating total displacements a new configuration can be calculated towards final configuration of

mechanical system.

3.2 Compact Axisymmetrical Formulation

We are considering the wound roll as an axisymmetric body which is formed by the accumulation of the concentric hoops. In the formulation we will use the notion of initial stress. We will assume that the hoops/layers are initially stressed due to web line stress. This initial stress will be the only source of load. In this case external virtual work will vanish and the general linearized form with the directional derivative will be:

$$D_{\Delta u}\delta W_{\text{int}} = -\delta W_{\text{int}} \tag{3.12}$$

In this study we will develop two nonlinear finite element models based on two different material models. These two models will share the common compact finite element formulation. In the first model we will adopt the material law proposed by Arola and this requires us to start with the first virtual (4.A) work expression. Axisymmetrical counterpart of the first virtual work expression takes the following form:

$$\delta W_{\text{int}} = \int_A tr\left[(S - S_0).\delta E^T\right] RdRdZ \tag{3.13}$$

In the expression we drop the 2π factor because of axisymmetry. We will adopt a compact finite element formulation in which we consider the wound roll under plane strain conditions. This assumption dictates that CMD direction strains and shear strains all vanish. In this case Green Lagrange strain tensor takes a simple form:

$$E = \frac{1}{2}\begin{bmatrix} \left(\frac{\partial r}{\partial R}\right)^2 - 1 & 0 \\ 0 & \left(\frac{r}{R}\right)^2 - 1 \end{bmatrix} \tag{3.14}$$

If we take variation with respect to displacement field we obtain the variation of Green Lagrange strain tensor:

$$\delta E = \begin{bmatrix} \delta\left(\frac{\partial r}{\partial R}\right)\frac{\partial r}{\partial R} & 0 \\ 0 & \delta\left(\frac{r}{R}\right)\frac{r}{R} \end{bmatrix} \tag{3.15}$$

Since all shear strains and CMD strains vanish and the virtual work will be done only by radial and tangential stresses and thus stress tensor takes the following simple form:

$$S = \begin{bmatrix} S_R & 0 \\ 0 & S_\theta \end{bmatrix} \tag{3.16}$$

The initial stress tensor will have only one nonzero component: the initial tangential stress component which is directly equal to negative of web line stress $-T_w$:

$$S_0 = \begin{bmatrix} 0 & 0 \\ 0 & -T_w \end{bmatrix} \tag{3.17}$$

Now we can easily express the inner product of variation of internal energy as:

$$\delta W_{\text{int}} = \int_A \left(\frac{\partial r}{\partial R} S_R \delta\left(\frac{\partial r}{\partial R}\right) + \frac{r}{R}(S_\theta + T_w)\delta\left(\frac{r}{R}\right)\right) R dR dZ \tag{3.18}$$

In our compact finite element formulation we have used reduced quadrilateral elements with unit thickness and as seen from the Figure 3.1 and Figure 3.2 a typical element has

two degrees of freedom: the radial displacements at the edges u_1 and u_2 .

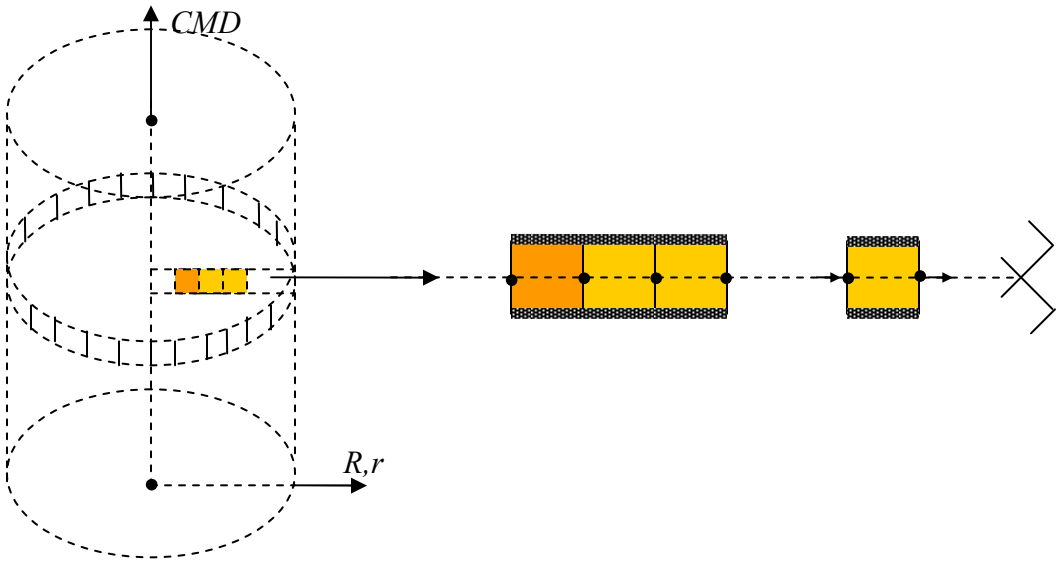

Figure 3.1 Compact Plane Strain Formulation

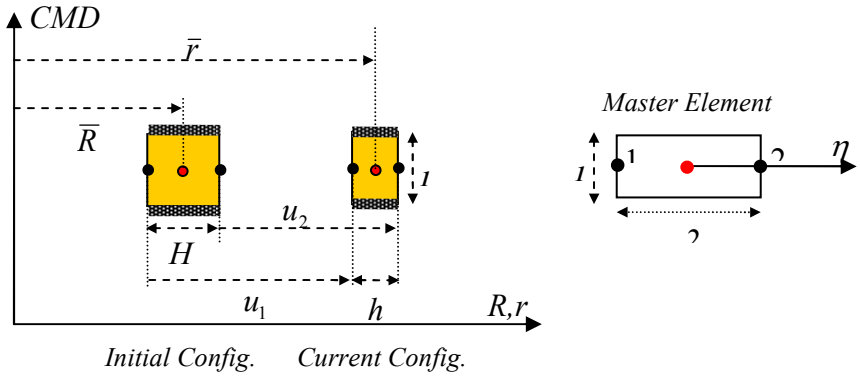

Figure 3.2 Compact Axisymmetric Element Formulation

We implemented isoparametric formulation with well known linear shape functions:

$$u = u_1 \frac{1-\eta}{2} + u_2 \frac{1+\eta}{2} \tag{3.19}$$

$$R = \overline{R} + \eta \frac{H}{2} \tag{3.20}$$

$$r = \bar{r} + \eta \frac{h}{2} \tag{3.21}$$

Here $\bar{r}$ and $\overline{R}$ are radial coordinates of the mid point of an element for current and initial configurations respectively. Similarly as seen from the figure *h* and *H* are thicknesses of an element for current and initial configurations respectively. Using nodal displacements the geometrical relations between initial and current configurations can be easily written from the figure 3.2:

$$\bar{r} = \overline{R} + \frac{u_1 + u_2}{2} \tag{3.22}$$

$$h = H + u_2 - u_1 \tag{3.23}$$

Now we can approximate the variation of the Green Lagrange strain components:

$$\frac{\partial r}{\partial R} = \frac{h}{H} \tag{3.24}$$

$$\frac{r}{R} = \frac{2\bar{r} + \eta h}{2\overline{R} + \eta H} \tag{3.25}$$

Inserting above expressions and taking into account unit thickness we found after rearrangement:

$$\delta W_{\text{int}} = \int_{-1}^{1} \left(\frac{h}{H} S_R \frac{(\delta u_2 - \delta u_1)}{H} + \frac{r}{R} (S_\theta + T_w) \frac{\delta u_2 + \delta u_1 + \eta(\delta u_2 - \delta u_1)}{2R} \right) R \frac{H}{2} d\eta \tag{3.26}$$

At this stage it is very easy to apply directional derivative directly by simply taking differentials of stress components S_R and S_θ :

$$D_{\Delta u}\delta W_{\text{int}} = \int_{-1}^{1}\left(D_{\Delta u}(hS_R)\frac{(\delta u_2 - \delta u_1)}{H^2} + D_{\Delta u}(rS_\theta + rT_w)\frac{\delta u_2 + \delta u_1 + \eta(\delta u_2 - \delta u_1)}{2R^2}\right) R\frac{H}{2}d\eta \tag{3.27}$$

The differentials for directional derivative can be given as Taylor series expansions retaining on linear terms:

$$D_{\Delta u}(hS_R) = \left(h\frac{\partial S_R}{\partial u_1} - S_R\right)\Delta u_1 + \left(h\frac{\partial S_R}{\partial u_2} + S_R\right)\Delta u_2 \tag{3.28}$$

$$D_{\Delta u}(rS_\theta + rT_w) = \left(r\frac{\partial S_\theta}{\partial u_1} + \frac{S_\theta + T_w}{2}\right)\Delta u_1 + \left(r\frac{\partial S_\theta}{\partial u_2} + \frac{S_\theta + T_w}{2}\right)\Delta u_2 \tag{3.29}$$

Here the term $D_{\Delta u}T_w$ vanishes because it is independent from the displacements. We also used the fact that:

$$\partial h/\partial u_1 = -\partial h/\partial u_2 = -1 \tag{3.30}$$

$$\partial r/\partial u_1 = \partial r/\partial u_2 = 1/2 \tag{3.31}$$

Inserting differentials and after rearranging we obtain the following linearized form of virtual work expression in terms of incremental displacements Δu_1 , Δu_2 :

$$\delta u_1\left\{\int_{-1}^{1} A_1 d\eta\right\} + \delta u_2\left\{\int_{-1}^{1} A_2 d\eta\right\} = 0 \tag{3.32}$$

Where

$$A_1 = -\frac{R}{2H}\left(\left(h\frac{\partial S_R}{\partial u_1} - S_R\right)\Delta u_1 + \left(h\frac{\partial S_R}{\partial u_2} + S_R\right)\Delta u_2\right)$$
$$+\frac{H(1-\eta)}{4R}\left(\left(r\frac{\partial S_\theta}{\partial u_1} + \frac{S_\theta + T_w}{2}\right)\Delta u_1 + \left(r\frac{\partial S_\theta}{\partial u_2} + \frac{S_\theta + T_w}{2}\right)\Delta u_2\right) - \frac{RhS_R}{2H} + \frac{rH(1-\eta)}{4R}(S_\theta + T_w) \tag{3.33}$$

$$A_2 = \frac{R}{2H}\left(\left(h\frac{\partial S_R}{\partial u_1} - S_R\right)\Delta u_1 + \left(h\frac{\partial S_R}{\partial u_2} + S_R\right)\Delta u_2\right)$$
$$+\frac{H(1+\eta)}{4R}\left(\left(r\frac{\partial S_\theta}{\partial u_1} + \frac{S_\theta + T_w}{2}\right)\Delta u_1 + \left(r\frac{\partial S_\theta}{\partial u_2} + \frac{S_\theta + T_w}{2}\right)\Delta u_2\right) + \frac{RS_R}{2H} + \frac{rH(1+\eta)}{4R}(S_\theta + T_w) \tag{3.34}$$

Since the virtual displacements are arbitrary, in order to satisfy linearized form of virtual work, it is required that:

$$\int_{-1}^{1} A_1 d\eta = 0 \tag{3.35}$$

$$\int_{-1}^{1} A_2 d\eta = 0 \tag{3.36}$$

If we rearrange again and use matrix notation we obtain element stiffness equations:

$${}^{II}K^e \Delta u = {}^{II}F^e \tag{3.37}$$

Where

$${}^{II}K^e_{11} = \int_{-1}^{1} -\frac{R}{2H}\left(h\frac{\partial S_R}{\partial u_1} - S_R\right) + \frac{H(1-\eta)}{4R}\left(r\frac{\partial S_\theta}{\partial u_1} + \frac{S_\theta + T_w}{2}\right)d\eta \tag{3.38}$$

$${}^{II}K^e_{22} = \int_{-1}^{1} \frac{R}{2H}\left(h\frac{\partial S_R}{\partial u_2} + S_R\right) + \frac{H(1+\eta)}{4R}\left(r\frac{\partial S_\theta}{\partial u_2} + \frac{S_\theta + T_w}{2}\right)d\eta \tag{3.39}$$

$$ {}^{II}K_{12}^{e} = \int_{-1}^{1} -\frac{R}{2H}\left(h\frac{\partial S_R}{\partial u_2} + S_R \right) + \frac{H(1-\eta)}{4R}\left(r\frac{\partial S_\theta}{\partial u_2} + \frac{S_\theta + T_w}{2} \right) d\eta \tag{3.40} $$

$$ {}^{II}K_{21}^{e} = \int_{-1}^{1} \frac{R}{2H}\left(h\frac{\partial S_R}{\partial u_1} - S_R \right) + \frac{H(1+\eta)}{4R}\left(r\frac{\partial S_\theta}{\partial u_1} + \frac{S_\theta + T_w}{2} \right) d\eta \tag{3.41} $$

$$ {}^{II}F_{1}^{e} = \frac{RhS_R}{2H} - \frac{rH(1-\eta)}{4R}(S_\theta + T_w) \tag{3.42} $$

$$ {}^{II}F_{2}^{e} = -\frac{RhS_R}{2H} - \frac{rH(1+\eta)}{4R}(S_\theta + T_w) \tag{3.43} $$

And $\Delta u = \begin{bmatrix} \Delta u_1 & \Delta u_2 \end{bmatrix}^T$

Here ${}^{II}K^{e}$, ${}^{II}F^{e}$ are 2x2 element tangent stiffness matrix and load vector respectively. The left superscript *II* indicates that the quantities are derived for 2nd Piola Kirchoff stresses. Now the finite element formulation is ready to implement material model. As we mentioned the first material model we will use is due to Arola. Here we will employ a simplified version of his model which is suitable for plane analysis. Furthermore we are omitting Poisson ratios other than in-plane ratio because they are reported to be small in the literature. In fact in his study Arola never mentioned it explicitly but as seen from his formulations and calculations he assumed a constitutive law which relates 2nd Piola Kirchoff stresses and Green Lagrange strains just like small strain theory. Due to this, his radial material model directly comes from Pfeiffer:

$$ S_R = K_1(1 - \exp(-K_2 E_R)) \tag{3.44} $$

And plane strain counterpart (with only nonzero in-plane Poisson ratio) of his tangential material model is:

$$S_\theta = \frac{J_\theta J_{CMD}}{J_{CMD} - J_\theta \nu_{CMD\theta}^2}(E_\theta) \tag{3.45}$$

Here J_θ, J_{CMD} and $\nu_{CMD\theta}$ are tangential and CMD modulus of elasticity and in-plane Poisson ratio respectively and they are measured with nominal stresses and linear strains. K_1 and K_2 are Pfeiffer's constants. Although using small strain constants with Green Lagrange strains are inappropriate we still use the formulation for comparison. The material model can be written explicitly over nodal displacements by using definitions of Green Lagrange strains:

$$E_R = \frac{1}{2}\left(\left(\frac{H + u_2 - u_1}{H}\right)^2 - 1\right) \tag{3.46}$$

$$E_\theta = \frac{1}{2}\left(\left(\frac{2R + u_2 + u_1}{2R}\right)^2 - 1\right) \tag{3.47}$$

Using chain rule and taking derivatives with respect to nodal displacements we can easily find:

$$\frac{\partial S_R}{\partial u_1} = -\frac{\partial S_R}{\partial u_2} = -{}^{II}J_R \frac{h}{H^2} \tag{3.48}$$

$$\frac{\partial S_\theta}{\partial u_1} = \frac{\partial S_\theta}{\partial u_2} = J_\theta^* \frac{r}{2R^2} \tag{3.49}$$

Where

$${}^{II}J_R = K_2(K_1 - S_R) \tag{3.50}$$

$$J_\theta^* = \frac{J_\theta J_{CMD}}{J_{CMD} - J_\theta \nu_{CMD\theta}^2} \tag{3.51}$$

Inserting the derivatives into stiffness terms and taking derivative will complete the complete nonlinear finite element formulation of a typical element. For the sake of simplicity if we retain constant strain over element and thus setting $\eta = 0$ we will obtain the following simple form for the element tangent stiffness matrix and element force vector:

$$^{II}K^e = \begin{bmatrix} \frac{R}{H}\left(\frac{^{II}J_R h^2}{H^2} + S_R\right) + \frac{H}{2R}\left(\frac{J_\theta^* r^2}{2R^2} + \frac{S_\theta + T_w}{2}\right) & -\frac{R}{H}\left(\frac{^{II}J_R h^2}{H^2} + S_R\right) + \frac{H}{2R}\left(\frac{J_\theta^* r^2}{2R^2} + \frac{S_\theta + T_w}{2}\right) \\ sym. & \frac{R}{H}\left(\frac{^{II}J_R h^2}{H^2} + S_R\right) + \frac{H}{2R}\left(\frac{J_\theta^* r^2}{2R^2} + \frac{S_\theta + T_w}{2}\right) \end{bmatrix} \tag{3.52}$$

$$^{II}F^e = \begin{bmatrix} \frac{Rh}{H}S_R - \frac{Hr}{2R}(S_\theta + T_w) \\ -\frac{Rh}{H}S_R - \frac{Hr}{2R}(S_\theta + T_w) \end{bmatrix} \tag{3.53}$$

In the second formulation which we will propose here originally, we will start with the second virtual work expression:

$$\delta W_{\text{int}} = \int_A tr\left[(P - P_0).\delta F^T\right] RdRdZ \tag{3.54}$$

The plane strain assumption dictates that CMD direction strains and shear strains all vanish as previously and in this case deformation gradient tensor takes a simple form:

$$F = \begin{bmatrix} \left(\frac{\partial r}{\partial R}\right) & 0 \\ 0 & \left(\frac{r}{R}\right) \end{bmatrix} \tag{3.55}$$

If we take variation with respect to displacement field we obtain the variation of deformation gradient tensor:

$$\delta F = \begin{bmatrix} \delta\left(\frac{\partial r}{\partial R}\right) & 0 \\ 0 & \delta\left(\frac{r}{R}\right) \end{bmatrix} \tag{3.56}$$

Again in case of plane strain all shear strains and CMD strains vanish and the virtual work will be done only by radial and tangential stresses and thus the 1st Piola Kirchoff stress tensor takes the following simple form:

$$P = \begin{bmatrix} P_R & 0 \\ 0 & P_\theta \end{bmatrix} \tag{3.57}$$

As before, the initial stress tensor will have only one nonzero component: the initial tangential stress component which is directly equal to negative of web line stress $-T_w$:

$$P_0 = \begin{bmatrix} 0 & 0 \\ 0 & -T_w \end{bmatrix} \tag{3.58}$$

Now we can easily express the inner product of variation of internal energy as:

$$\delta W_{\text{int}} = \int_A \left(P_R \delta\left(\frac{\partial r}{\partial R}\right) + (P_\theta + T_w)\delta\left(\frac{r}{R}\right)\right) R dR dZ \tag{3.59}$$

Again using the same isoparametric formulation we arrive at the following expression for

the variation of the virtual work:

$$\delta W_{\text{int}} = \int_{-1}^{1} \left(P_R \frac{(\delta u_2 - \delta u_1)}{H} + (P_\theta + T_w) \frac{\delta u_2 + \delta u_1 + \eta(\delta u_2 - \delta u_1)}{2R} \right) R \frac{H}{2} d\eta \tag{3.60}$$

Linearization will be carried out in the same way. We will directly take the derivatives with respect to nodal displacements and retain on linear terms:

$$D_{\Delta u}\delta W_{\text{int}} = \int_{-1}^{1} \left(D_{\Delta u}(P_R) \frac{(\delta u_2 - \delta u_1)}{H} + D_{\Delta u}(P_\theta + T_w) \frac{\delta u_2 + \delta u_1 + \eta(\delta u_2 - \delta u_1)}{2R} \right) R \frac{H}{2} d\eta \tag{3.61}$$

$$D_{\Delta u}(P_R) = \frac{\partial P_R}{\partial u_1}\Delta u_1 + \frac{\partial P_R}{\partial u_2}\Delta u_2 \tag{3.62}$$

$$D_{\Delta u}(P_\theta) = \frac{\partial P_\theta}{\partial u_1}\Delta u_1 + \frac{\partial P_\theta}{\partial u_2}\Delta u_2 \tag{3.63}$$

Inserting differentials and after rearranging we again obtain the following linearized form of virtual work expression in terms of incremental displacements Δu_1 , Δu_2 :

$$\delta u_1 \left\{ \int_{-1}^{1} B_1 d\eta \right\} + \delta u_2 \left\{ \int_{-1}^{1} B_2 d\eta \right\} = 0 \tag{3.64}$$

Where

$$B_1 = -\frac{R}{2}\left(\frac{\partial P_R}{\partial u_1}\Delta u_1 + \frac{\partial P_R}{\partial u_2}\Delta u_2 \right) + \frac{H(1-\eta)}{4}\left(\frac{\partial P_\theta}{\partial u_1}\Delta u_1 + \frac{\partial P_\theta}{\partial u_2}\Delta u_2 \right) - \frac{RP_R}{2} + (P_\theta + T_w)\frac{H(1-\eta)}{4} \tag{3.65}$$

$$B_2 = \frac{R}{2}\left(\frac{\partial P_R}{\partial u_1}\Delta u_1 + \frac{\partial P_R}{\partial u_2}\Delta u_2 \right) + \frac{H(1+\eta)}{4}\left(\frac{\partial P_\theta}{\partial u_1}\Delta u_1 + \frac{\partial P_\theta}{\partial u_2}\Delta u_2 \right) + \frac{RP_R}{2} + (P_\theta + T_w)\frac{H(1+\eta)}{4} \tag{3.66}$$

Using the principle of virtual work we again conclude that:

$$\int_{-1}^{1} B_1 d\eta = 0 \tag{3.67}$$

$$\int_{-1}^{1} B_2 d\eta = 0 \tag{3.68}$$

These equations can be arranged in the matrix form as previously:

$${}^{I}K^{e}\Delta u = {}^{I}F^{e} \tag{3.69}$$

Where

$${}^{I}K_{11}^{e} = -\frac{R}{2}\frac{\partial P_R}{\partial u_1} + \frac{H(1-\eta)}{4}\frac{\partial P_\theta}{\partial u_1} \tag{3.70}$$

$${}^{I}K_{22}^{e} = \frac{R}{2}\frac{\partial P_R}{\partial u_2} + \frac{H(1+\eta)}{4}\frac{\partial P_\theta}{\partial u_2} \tag{3.71}$$

$${}^{I}K_{12}^{e} = -\frac{R}{2}\frac{\partial P_R}{\partial u_2} + \frac{H(1-\eta)}{4}\frac{\partial P_\theta}{\partial u_2} \tag{3.72}$$

$${}^{I}K_{21}^{e} = \frac{R}{2}\frac{\partial P_R}{\partial u_1} + \frac{H(1+\eta)}{4}\frac{\partial P_\theta}{\partial u_1} \tag{3.73}$$

$${}^{I}F_{1}^{e} = \frac{RP_R}{2} - (P_\theta + T_w)\frac{H(1-\eta)}{4} \tag{3.74}$$

$${}^{I}F_{2}^{e} = -\frac{RP_R}{2} - (P_\theta + T_w)\frac{H(1+\eta)}{4} \tag{3.75}$$

Here ${}^{I}K^{e}$, ${}^{I}F^{e}$ are 2x2 element tangent stiffness matrix and load vector respectively. The left superscript *I* indicates that the quantities are derived for 1st Piola Kirchoff stresses.

The material model we will propose uses the 1st Piola Kirchoff stresses and the linear strains. This is convenient because in the material characterization experiments (stack compression and MD modulus test) the stresses are always calculated over initial dimensions of the specimens. Thus the stresses used to model material behavior are nominal stresses or simply the 1st Piola Kirchoff stresses used in our analysis. Using this fact we employ:

$$P_R = K_1(1 - \exp(-K_2(F_R - 1))) \tag{3.76}$$

$$P_\theta = \frac{J_\theta J_{CMD}}{J_{CMD} - J_\theta \nu_{CMD\theta}^2}(F_\theta - 1) \tag{3.77}$$

Where K_1 and K_2 are Pfeiffer's constants, J_θ, J_{CMD} and $\nu_{CMD\theta}$ are tangential and CMD modulus of elasticity and in-plane Poisson ratio respectively as before and they are actually measured with nominal stresses (here 1st Piola Kirchoff stresses) and linear strains. F_R and F_θ are deformation gradient components for radial and tangential direction respectively and they are simply related with the corresponding linear strain components ε_R and ε_θ:

$$\varepsilon_R = F_R - 1 = \frac{u_2 - u_1}{H} \tag{3.78}$$

$$\varepsilon_\theta = F_\theta - 1 = \frac{u_2 + u_1}{2R} \tag{3.79}$$

In order to complete finite element formulation we take derivatives of material relations with respect to nodal displacements. Using chain rule we obtain:

$$\frac{\partial P_R}{\partial u_1} = -\frac{\partial P_R}{\partial u_2} = -\frac{{}^I J_R}{H} \tag{3.80}$$

$$\frac{\partial P_\theta}{\partial u_1} = \frac{\partial P_\theta}{\partial u_2} = \frac{J_\theta^*}{2R} \tag{3.81}$$

Where

$${}^I J_R = K_2(K_1 - P_R) \tag{3.82}$$

$$J_\theta^* = \frac{J_\theta J_{CMD}}{J_{CMD} - J_\theta \nu_{CMD\theta}^2} \tag{3.83}$$

Inserting the derivatives into stiffness terms will complete the complete nonlinear finite element formulation of a typical element for the material modal *I*. For the sake of simplicity if we retain constant strain over element and thus setting $\eta = 0$ we will obtain the following simple form for the element tangent stiffness matrix and element force vector:

$${}^I K^e = \begin{bmatrix} \frac{R\,{}^I J_R}{H} + \frac{H J_\theta^*}{4R} & -\frac{R\,{}^I J_R}{H} + \frac{H J_\theta^*}{4R} \\ sym. & \frac{R\,{}^I J_R}{H} + \frac{H J_\theta^*}{4R} \end{bmatrix} \tag{3.84}$$

$${}^I F^e = \begin{bmatrix} P_R R - (P_\theta + T_w)\frac{H}{2} \\ -P_R R - (P_\theta + T_w)\frac{H}{2} \end{bmatrix} \tag{3.85}$$

3.3 Numerical Procedure

The finite element formulations developed above can be easily implemented into a wound roll algorithm. Since the tangent stiffness matrices are 2x2 and symmetric the usual finite element assemblage procedure will result in a very compact form especially if they are stored in rectangular matrices. Wound roll model will include the core structure. Core structure can be easily modeled as web structure only by changing material constants. In our calculations core is considered to be composed of linear orthotropic material. We can give the general frame work of algorithm. The key for the algorithm is the definition of a state during calculation. State *(j,i)* in the algorithm means the state (configuration, material properties) of the system for $i^{th.}$ iteration step during the addition of the $j^{th.}$ layer. After desired accuracy is obtained for adding a layer the code decides if there is enough space for the next layer. If there is enough space then the code calculates the initial coordinates of the new layer and places it at the top of current configuration and the iteration procedure will start again. A linear form of the nonlinear model can be obtained if the iteration decision is always omitted. In this case for every lap there will be only single iteration. In fact for hard materials the nonlinear code indeed goes for only a few iterations. For very soft materials on the other hand there might be no convergence so there is a limit ($i_{max} = 100$) on the iteration counter i. When the code hits this limit the process will be terminated. Our model (model with left superscript *I*) shows a much more stable and computationally efficient character while solving for some imaginary very soft materials. The second model (model *II*) based on Arola's material assumptions needs iteration limiters for avoiding infinite loops.

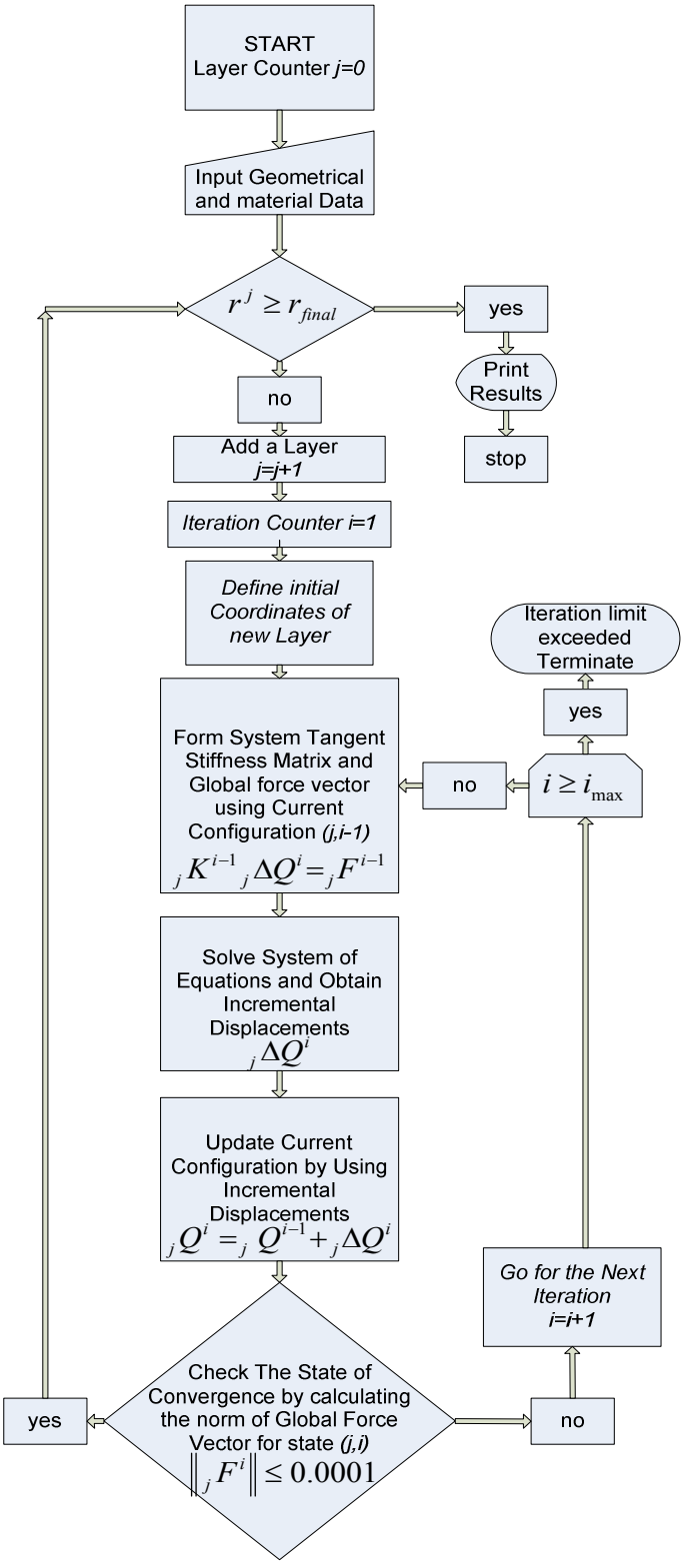

Figure 3.3 Numerical Solution Algorithm

3.4 Results and Discussion

In this section the results of the nonlinear models (model *I* and *II*) (which are denoted as PK1 and PK2 in the graphs), the linear models (which are denoted as LINEAR and LINEAR TL), Benson's large deformation model and Hakiel's classic model will be compared. The results from models will also be compared with experimental results which were collected in winding tests of spun-bond nonwoven polypropylene and bath tissue webs that are fine examples of webs with very high radial compressibility. Finally results were compared with the previous experimental work done on newsprint by Good et al [2]. Before the comparison can precede the details of linear models and Benson's material model require review.

The results for simple linear models which are based on the same compact finite element formulation but derived for small strain assumptions will also be compared. Model results with a "LINEAR TL" tag corresponds to small strain version of PK1 and it can be easily obtained if the actual PK1 allowed iterating only for once per model layer. Here TL stands for "tension loss" which is a feature built in the model instinctively because of the pre-stress formulation. In this situation the final tension of a winding layer will be lower than the web line stress as expected. The model with "LINEAR" tag is basically same with the "LINEAR TL" but it iterates for the winding layer's tension in order to obtain the web line tension level. In this situation the final tension of a winding layer will be equal to the web line stress after iteration. Since the material properties are kept constant during addition of a layer the "LINEAR" model needs only one solution and than a factor can be computed such that when multiplied with incremental strains and

stresses desired configuration can be obtained.

In his study Benson used true strain with the Cauchy stresses. Benson started with Pfeiffer's famous radial material model:

$$P_R^{Benson} = K_1\left(e^{K_2\varepsilon_R} - 1\right) \tag{3.86}$$

Here P_R^{Benson} and ε_R are the compressive Cauchy stress and compressive linear strain in radial direction. Using the initial and current thickness (*H* and *h* respectively) the linear strain is given as:

$$\varepsilon_R = \frac{H-h}{H} \tag{3.87}$$

Benson assumed a similar radial material law such that:

$$P_R^{Benson} = \alpha\left(e^{\beta\varepsilon_R^{NL}} - 1\right) \tag{3.88}$$

where α and β are material constants Benson employed instead of K_1 and K_2 because of his choice of strain measure. Here ε_R^{NL} is the true strain and it is given as:

$$\varepsilon_R^{NL} = \ln\left[\frac{H}{h}\right] \tag{3.89}$$

Inserting the true strain expression and after algebraic operations Benson obtained:

$$P_R^{Benson} = \alpha\left(\left(\frac{h}{H}\right)^{-\beta} - 1\right) \tag{3.90}$$

Benson's material model in the tangential direction is the usual small strain material

model. He also omitted the Poisson ratios by arguing that they are small. His formulation assumed plane stress conditions so there is no coupling between the CMD and θ directions either. The relation between K_1, K_2 and α, β does not allow any analytical solution and Benson did not propose any method to obtain α, β based upon known values of K_1 and K_2. One solution would be to perform stack compression experiments and curve fit with the relation written in terms of ε_R^{NL} which involves α and β. This is not practical since the K_1, K_2 type measurement has been adapted widely in radial modulus characterization so a numerical conversion algorithm was developed. The development begins by defining the inverse of the compaction ratio of a stack of material which has an initial thickness H:

$$y = \frac{H}{h} \tag{3.91}$$

where h is the thickness under the pressure level P^{SCT}. The superscript SCT stands for Stack Compression Test. For a given material the relation between P^{SCT} and y is known if K_1 and K_2 are known for that material:

$$P^{SCT} = K_1(e^{K_2\left(1-\frac{1}{y}\right)} - 1) \tag{3.92}$$

Taking the derivative of this expression (59) relation with respect to *y* yields:

$$\frac{\partial P^{SCT}}{\partial y} = \left(P^{SCT}\right)' = \frac{K_2 K_1 (e^{K_2\left(1-\frac{1}{y}\right)})}{y^2} \tag{3.93}$$

This relation can be used to produce *n* data points by defining y_i : $i^{th.}$ step of compaction:

$$y_i = \frac{1}{\bar{h}_i} \tag{3.94}$$

where $\bar{h}_i$ is the $i^{th.}$ normalized stack height. It can be given as:

$$\bar{h}_i = 1 - (i-1)/100 \tag{3.95}$$

The $i^{th.}$ derivative of the compressive pressure $\left(P^{SCT}\right)'_i$ can be obtained which corresponds to the normalized stack height $\bar{h}_i$ by substituting y_i into expression (93):

$$\left(P^{SCT}\right)'_i = \frac{K_2 K_1 (e^{K_2\left(1-\frac{1}{y_i}\right)})}{y_i^2} \tag{3.96}$$

This is repeated for *i = 1* to *n* and thus *n* data points are obtained:

$$\left\{y_i, \left(P^{SCT}\right)'_i\right\} \text{ for } i=1,2,...,n \tag{3.97}$$

The counterpart relation for Benson's model is:

$$P_{SCT} = \alpha(y^{\beta} - 1) \tag{3.98}$$

If the derivative is taken as before:

$$\frac{\partial P^{SCT}}{\partial y} = \left(P^{SCT}\right)' = \alpha\beta(y)^{\beta-1} \tag{3.99}$$

A given functional relation written in terms of known K_1 and K_2 constants has been discretized in order to obtain data points for a least square fit of a functional relation written in terms of α and β which are unknown. Taking the logarithms of both sides

yields:

$$\ln\left[\left(P^{SCT}\right)'\right] = \ln[\alpha\beta] + (\beta - 1)\ln[y] \tag{3.100}$$

Now linear regression can be employed over the $\ln\left[\left(P^{SCT}\right)'\right]$ and $\ln[y]$ terms to obtain Benson's material model coefficients β and α:

$$\beta = \frac{\left(\sum_{i=1}^{n} i\right)\left(\sum_{i=1}^{n} \ln\left[\left(P^{SCT}\right)'_i\right]\ln[y_i]\right) - \left(\sum_{i=1}^{n}\ln[y_i]\right)\left(\sum_{i=1}^{n}\ln\left[\left(P^{SCT}\right)'_i\right]\right)}{\left(\sum_{i=1}^{n} i\right)\left(\sum_{i=1}^{n}\ln[y_i]^2\right) - \left(\sum_{i=1}^{n}\ln[y_i]\right)^2} + 1 \tag{3.101}$$

$$\alpha = \frac{1}{\beta} Exp\left\{\frac{\left[\left(\sum_{i=1}^{n}\ln\left[\left(P^{SCT}\right)'_i\right]\right) - (\beta - 1)\left(\sum_{i=1}^{n}\ln[y_i]\right)\right]}{\left(\sum_{i=1}^{n} i\right)}\right\} \tag{3.102}$$

Both models were coded. The stresses presented for the models developed here are the Cauchy stresses since they are the actual stresses measured. For the 1st Piola Kirchoff radial stresses the Cauchy stresses are calculated as:

$${}^{I}\sigma_R = \frac{\bar{R}}{\bar{r}} P_R \tag{3.103}$$

From the 2nd Piola Kirchoff radial stresses the Cauchy stresses are calculated as:

$${}^{II}\sigma_R = \frac{\bar{R}h}{\bar{r}H} S_R \tag{3.104}$$

The results are calculated for plane stress case by simply taking the in plane ratio zero.

This is done in order to compare with the Benson's and Hakiel's models which were developed for plane stress case. In the charts that follow the Cauchy stresses are plotted versus the final radial positions of layers ($\bar{r}$). The first comparison was performed on a spun-bond non-woven polypropylene material which was 0.152 mm in thickness. The geometric and web material data are provided in Table 3.1. The test and model results are shown for web line stress level (T_w) of 115 KPa in Figure 3.4.The pressure data was collected in all cases by winding in pull tabs that extended over the width of the roll and protruded out both sides of the roll. These tabs consist of steel shim enveloped in brass shim to provide a low coefficient of friction. The tabs were inserted in stacks of the non-woven and tissue web. The stacks were subjected to varied pressure and the force required to cause the steel shim to slip within the brass shim was measured. In this way calibration curves were developed for each pull tab. The pull tabs were then wound into test rolls and after winding completed the force required to cause each pull tab to slip was measured and from the calibration charts the pressure was then known at that roll radius.

Core inner radius	1.27 cm	$\mathbf{J_{CMD}}$	16550 KPa
Core outer radius	5.08 cm	$\mathbf{J_{core}}$	6.9 10^8 KPa
Roll final radius	24.1 cm	$\mathbf{\nu_{core}}$	0.3
$\mathbf{K_1}$	1.32 KPa	$\boldsymbol{\alpha}$	2.25 KPa
$\mathbf{K_2}$	13.39	$\boldsymbol{\beta}$	9.6
$\mathbf{J_0}$	55160 KPa	$\mathbf{T_w}$	115 KPa

Table 3.1 Material and geometric properties for Spun-bond Non-Woven Polypropylene

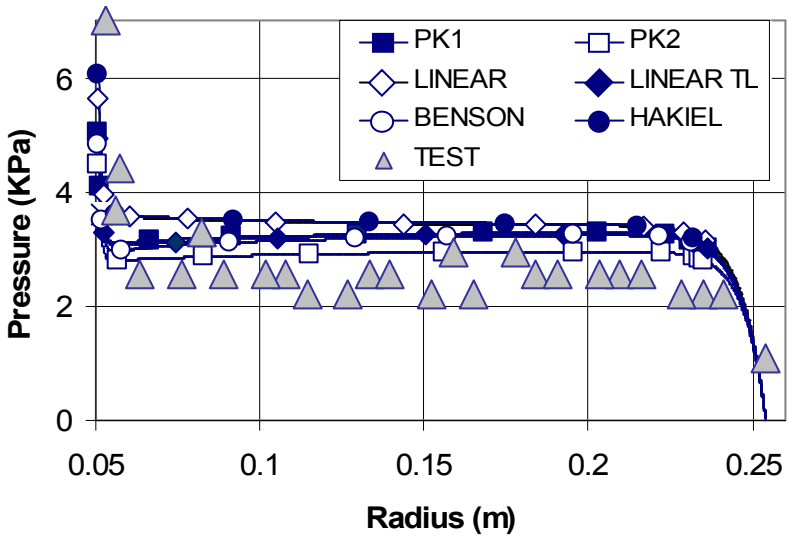

Figure 3.4 Radial Pressures for Spun-bond Non-Woven – T_w=*115* KPa

Tests and simulations were also conducted for a bath tissue which was 0.182 mm in thickness. Note the inputs required to execute the models are provided in Table 3.2. Also note that the tests and simulations were conducted for two winding tensions. Results for a web line tension of 92.4 KPa are presented in Figure 3.5 and results for a web line tension of 59.2 KPa are presented in Figure 3.6.

Core inner radius	1.27 cm	J_{CMD}	3337 KPa
Core outer radius	4.45 cm	J_{core}	6.9 10^8 KPa
Roll final radius	19 and 22.9 cm	ν_{core}	0.3
K_1	0.258 KPa	α	0.44
K_2	13.474	β	9.67
J_0	3337 KPa	T_w	59.2 and 92.4 KPa

Table 3.2 Material and geometrical properties for Bath Tissue

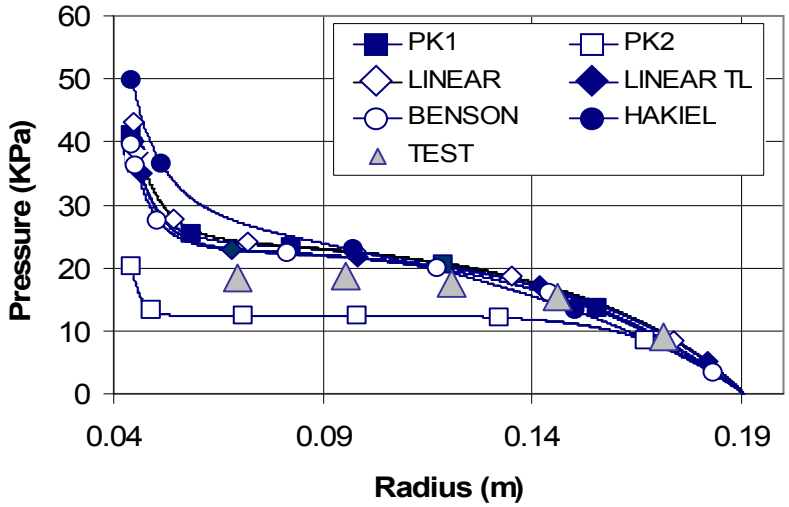

Figure 3.5 Radial Pressures for Bath Tissue– T_w=*92.4* KPa

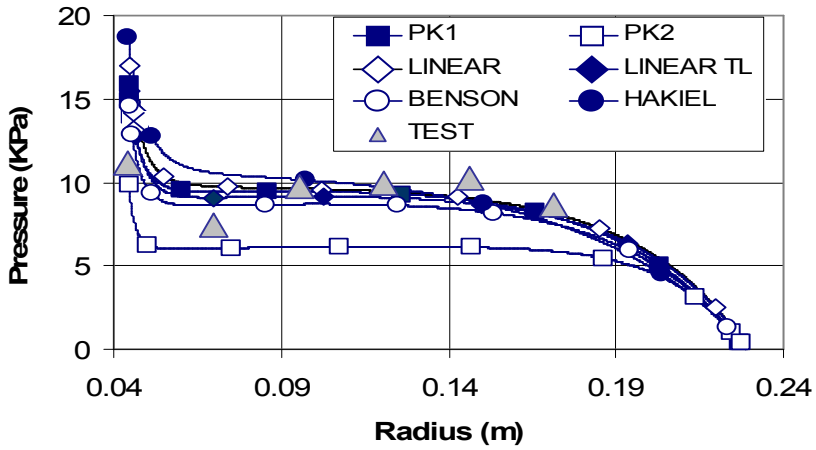

Figure 3.6 Radial Pressures for Bath Tissue– T_w=*59.2* KPa

The material and geometrical data for the newsprint which was 0.071 mm in thickness is given in Table 3.3. Newsprint results are shown for two levels of web line stress: 5.17

and 3.45 MPa in Figures 3.7 and 3.8 respectively.

Core inner radius	1 cm	J_{CMD}	3.37GPa
Core outer radius	4.45 cm	J_{core}	6.9 10^8 KPa
Roll final radius	13.35 cm	ν_{core}	0.3
K_1	1.175 KPa	α	1.54 KPa
K_2	45.14	β	39.72
J_0	3.37 GPa	T_w	3.45, 5.17 MPa

Table 3.3 Material and geometrical properties for Newsprint

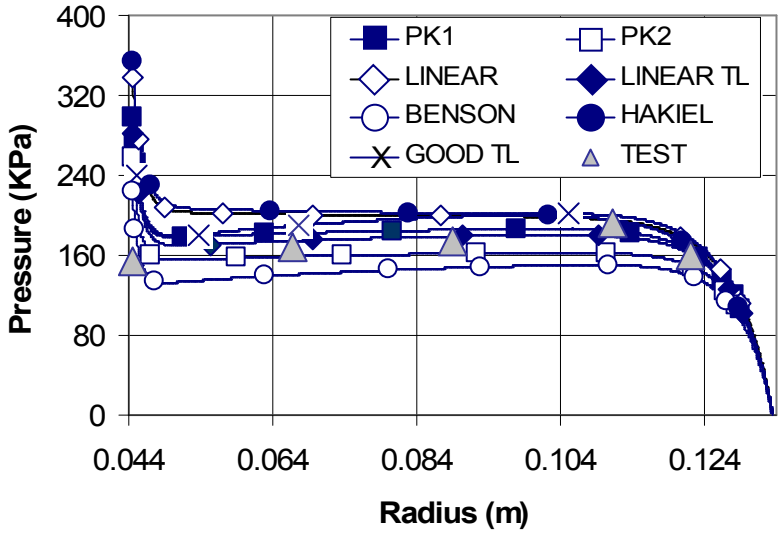

Figure 3.7 Radial Pressures for Newsprint– T_w=*5.17.* MPa

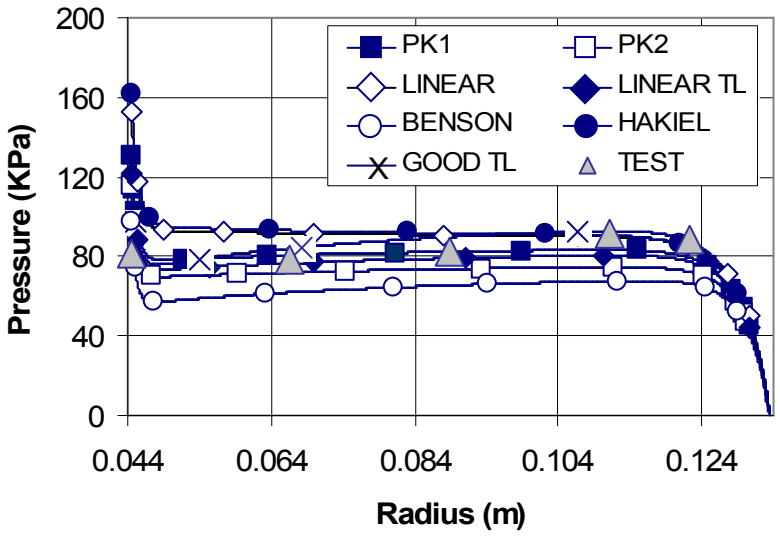

Figure 3.8 Radial Pressures for Newsprint– T_w=*3.45* MPa

Mean absolute error tables have been produced for the cases shown here in order to clearly understand the models prediction capabilities in comparison to the test data. Tables 3.4, 3.5 and 3.6 are calculated for the spun-bond non-woven, the bath tissue and newsprint, respectively.

Spun-bond	**Mean Absolute Error (KPa)**
Models	**Tw=115. (KPa)**
PK1	0.124
Linear	0.139
Linear TL	0.122
PK2	0.094
Benson	0.120
Hakiel	0.139

Table 3.4 Mean Absolute Error for Spun-bond Non-Woven

Bath Tissue	Mean Absolute Error (kPa)	
Models	Tw= 92.4 (kPa)	Tw=59.2 (kPa)
PK1	0.653	0.140
Linear	0.701	0.132
Linear TL	0.585	0.152
PK2	0.610	0.455
Benson	0.530	0.189
Hakiel	0.689	0.180

Table 3.5 Mean Absolute Error for Bath Tissue

Newsprint	Mean Absolute Error (kPa)	
Models	Tw= 3.45 (mPa)	Tw=5.17 (mPa)
PK1	8.81	13.0
Linear	19.7	51.5
Linear TL	13.6	30.5
PK2	16.7	34.0
Benson	17.0	31.2
Hakiel	22.0	54.8
Good TL	12.5	41.9

Table 3.6 Mean Absolute Error for Newsprint

In Table 3.6 we have also included results from tension loss model (Good TL) [2].

3.5 Conclusions

Based on comparison of error levels from tables from all the nonlinear models for all web materials studied it cannot be said that one nonlinear model is superior to another. From Table 3.4 it is seen that PK2 is best for Spun-bond Nonwoven , from Table 3.5 its is seen that PK1 and Benson's models predicted better for bath tissue and finally from Table 3.6 it is clear that PK1 works better for newsprint. It can be concluded that all these nonlinear

models produced similar results.

An important question would be why do the results of the nonlinear models and the linear model that accounts for tension loss agree so well? When a layer of web material is added to the outside of a winding roll the majority of the deformation occurs in an outer few laps. Both the nonlinear Model I and the linear model are pre-stress formulations that allow the loss of tension in the outer layer reported by Good et al [2]. It must be concluded that the interaction between stress and deformation in the layers beneath the outer lap are inconsequential on the final stress or pressure distributions in the roll. Still intriguing are the levels of radial strain wound into these rolls. To demonstrate the total radial strain for the spun-bond non-woven, computed using the nonlinear Model I, is shown in Figure 3.9. As shown these strains are much in excess of the 1% that is conventionally held as the limit for linear small strain analyses. Although it is possible that nonlinear models may show benefit for materials with yet lower K_1 and K_2 values it must also be said that the spun-bond non-woven and tissue webs for which results were reported herein have some of the lowest K_1 and K_2 values the authors have ever witnessed among a host of web materials. So it is unknown if yet more compressible webs exist that would require the use of a nonlinear wound roll model. That being said all the wound roll models discussed herein account for material nonlinearity.

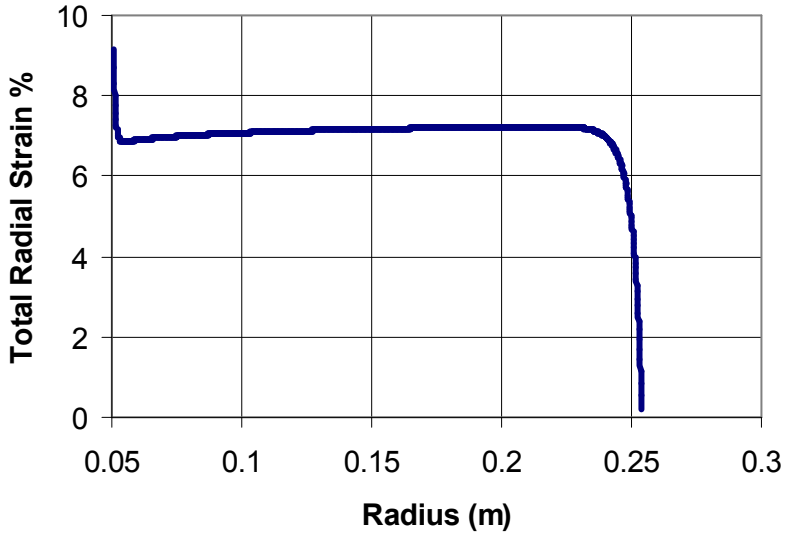

Figure 3.9 Total Radial Strain from Model I for Spun-Bond Non-Woven – T_w=*115* KPa

The findings herein are important as wound roll models have already evolved to 2D axisymmetric codes such that the effects of thickness and length nonuniformities can be examined. This has caused a dramatic increase in problem size and if nonlinearity was important iteration would be required and huge investments of computation time would be required to solve problems where the web compressibility was high. The finding that linear models that account for tension loss (such as the pre-stress axisymmetric code - described herein as Linear TL) produce accurate results for even these highly compressible materials will help to greatly reduce computational time in the 2D codes.

4. WOUND ROLL PRE-STRESS FORMULATION

Axisymmetric wound roll models provide the greatest definition of wound roll internal stresses to date. Simple one dimensional models can provide the user with radial profiles of pressure and circumferential stress as a function of radius. These models later evolved into pseudo two dimensional models where for the first time the impact of web nonuniformities such as thickness and web length could be studied across the web width. These models are described as pseudo two dimensional models because they were a series of the earlier one dimensional models. As such the outputs were limited to the pressure and circumferential stress outputs of one dimensional models but could also be used to predict the shape of the wound roll. Axisymmetric models provide outputs of pressure, circumferential stress, axial stress, and shear stress as a function of radius and cross machine direction location throughout a wound roll. As such these models are capable of describing more types of roll defects than all previous winding models. This chapter will focus on the development of a new two dimensional axisymmetric wound roll model based upon a pre-stress formulation. This new model is thought as (AWM): one of the three core internal components of the proposed combined model.

4.1 Pre-Stress Finite Element Formulation

The concept of a pre-stress type formulation will be introduced. In the wound roll model development the incoming layer has an initial stress called the web line stress. A key feature of a pre-stress type formulation is to incorporate this stress as a source of load for the general roll structure system. The formulation begins with basic concepts of stress and strain relations in linear elasticity:

$$\sigma - \sigma_0 = M\varepsilon \tag{4.1}$$

Here $\sigma, \sigma_0, \varepsilon$ are vectors including ordered components of final stress, initial stress and the strain that result from the stress state difference ($\sigma - \sigma_0$) between initial and final configurations respectively. M is the symmetric orthotropic material stiffness matrix which relates the axisymmetric stresses to the corresponding strains. An energy expression which defines the total potential energy of the system will be developed. In the derivation of the total potential energy generally there are two sources. One source is the potential energy produced by the internal forces (stresses) and while the second is the potential of the external forces. There is not an explicit external force for the wound roll winding process. The total potential energy arises only from internal forces. The strain ε which resulted from the stress difference $\sigma - \sigma_0$ will perform work. For a unit volume of the body the elastic potential energy produced by the stress difference can be given as:

$$PE_1 = \frac{1}{2}(\sigma - \sigma_0)^T \varepsilon \tag{4.2}$$

The factor of ½ results from the linear dependency of the strains on the stress difference. There will also be work performed by the strains ε and the initial stresses σ_o. Since the

initial stresses σ_0 existed prior to the development of the strains which resulted from the stress difference there is no factor of ½ :

$$PE_2 = \sigma_0^T \varepsilon \tag{4.3}$$

The total potential produced in a unit volume will be:

$$TP = \frac{1}{2}(\sigma - \sigma_0)^T \varepsilon + \sigma_0^T \varepsilon \tag{4.4}$$

and the total potential energy for the entire body can be given by the following volume integral:

$$TPE = \int_V \left(\frac{1}{2}(\sigma - \sigma_0)^T \varepsilon + \sigma_0^T \varepsilon \right) dV \tag{4.5}$$

This can be solely expressed in terms of the strain and the known initial stress by using constitutive properties which relate the stress difference and the strain (XX). Substituting yields:

$$TPE = \int_V \left(\frac{1}{2} \varepsilon^t M \varepsilon + \sigma_0^t \varepsilon \right) dV \tag{4.6}$$

where *M* is the symmetric matrix representing orthotropic material behavior. The final energy expression is potential energy of a system with initial stress applied only. Equilibrium will be satisfied when the first variation of the potential energy vanishes with respect to strain. Substituting yields:

$$\delta TPE = \int_V \left(\delta\varepsilon^T M \varepsilon + \delta\varepsilon^T \sigma_0 \right) dV = 0 \tag{4.7}$$

The finite element method will be used to form a numerical solution of these equations. In the finite element method the body will be divided into sub-bodies with simple

geometric characteristics and the unknown variables (displacements herein) will be defined only for the nodes on the boundaries of the sub bodies. These sub bodies are called elements. The total displacement field within the element is then represented by interpolation of the unknown nodal values over the domain of the elements. The same interpolation equations (called shape functions) will be used for all elements. A typical element will have *N* nodes on the boundary of element. Every node will have a certain number of degrees-of-freedom (dof) required by the mathematical model. For example for the wound roll models based on axisymmetrical considerations there will 2 dof for each node of the element in the (*r,z*) coordinate system. These dofs will correspond to the *u* and *w* displacements of each node. The displacement vector within the domain of an element will be defined as:

$$\vec{u}_e = \left[u_e(r,z) \quad w_e(r,z)\right]^T \tag{4.8}$$

It is assumed that there are *N* representative points or nodes on the boundary of the element. In order to represent the elemental displacement field as an interpolation of the nodal values the unknown vector of nodal displacements is first defined:

$$\vec{u}_e^* = \left[u_1 \quad w_1 \quad \ldots\ldots \quad u_N \quad w_N\right]^T \tag{4.9}$$

The interpolation or shape functions will be denoted as $\phi_i(r,z)$ i=1,…,N, thus the deformation anywhere within the domain of an element can be written in terms of the nodal deformations as:

$$\vec{u}_e = \Phi\ \vec{u}_e^* \tag{4.10}$$

The same shape functions are commonly used to interpolate both the u and w deformations and thus:

$$\Phi = \begin{bmatrix} \phi_1 & 0 & ..... & \phi_N & 0 \\ 0 & \phi_1 & ..... & 0 & \phi_N \end{bmatrix} \tag{4.11}$$

These functions must satisfy some conditions. First the elemental deformation should yield the nodal deformation at the nodal locations. This is ensured by forcing the shape functions to take a value of unity at the node they are associated with and zero at all other nodes. This can be stated mathematically as:

$$\phi_i(r_j, z_j) = \delta_{ij} \; for\; j=1,2,...N \tag{4.12}$$

where δ_{ij} is the Kronecker delta. The second condition is that the shape functions should be as sufficiently smooth as the mathematical model requires. The second condition ensures that derivatives exist in the discrete numerical representation of the mathematical model. Now the strain components can be derived from displacements. Using the differential operator D the element strain vector is:

$$\varepsilon_e = D\bar{u}_e \tag{4.13}$$

where

$$D = \begin{bmatrix} \partial/\partial r & 0 & \partial/\partial z & 1/r \\ 0 & \partial/\partial z & \partial/\partial r & 0 \end{bmatrix}^T \tag{4.14}$$

$$\varepsilon_e = \begin{bmatrix} \varepsilon_r & \varepsilon_z & \gamma_{rz} & \varepsilon_\theta \end{bmatrix}^T \tag{4.15}$$

Since the nodal values of deformation are not functions of position the strains can be written in terms of nodal displacements as:

$$\varepsilon_e = (D\Phi)\vec{u}_e^* \tag{4.16}$$

In this situation the variation of the strain will be simply given with the variation of the nodal displacements:

$$\delta\varepsilon_e = (D\Phi)\delta\vec{u}_e^* \tag{4.17}$$

Where nodal displacement vector is given as:

$$\delta\vec{u}_e^* = \begin{bmatrix}\delta u_1 & \delta w_1 & ..... & \delta u_N & \delta w_N\end{bmatrix}^T \tag{4.18}$$

The potential energy expression is written for whole body. Since we are working with finite elements we simply assume that total potential is the sum of the potential energies of the individual elements:

$$\delta W = \sum_e \int_{V_e} \delta\varepsilon_e{}^t M_e \varepsilon_e + \delta\varepsilon_e{}^t \sigma_0 dV_e \tag{4.19}$$

Here for the sake of simplicity every element is assumed to have the same initial stress. If we substitute these discretized strain and its variation into variation of potential energy for a typical element the discretized form of equilibrium is obtained:

$$\delta W = \sum_e \delta\left(\vec{u}_e^*\right)^T \left(\int_{V_e} B^T M B dV_e \vec{u}_e^* + \int_{V_e} B^T \sigma_0 dV_e \right) = 0 \tag{4.20}$$

Here B is the matrix which includes the derivatives of the interpolation functions:

$$B = D\Phi \tag{4.21}$$

The matrix vector form of elemental equations can be written in terms of element stiffness matrix and element nodal force matrix:

$$\delta W = \sum_e \delta\left(\vec{u}_e^*\right)^T \left(K_e \vec{u}_e^* - F_e\right) = 0 \tag{4.22}$$

$$K_e = \int_e B^T M_e B dV_e \tag{4.23}$$

$$F_e = -\int_{V_e} B^T \sigma_0 dV_e \tag{4.24}$$

The elements are connected together at boundaries by the nodes. A model of the body can be developed using the general finite element assembly procedure. The global stiffness matrix, global displacement vector and global force vector replace the summation over elements:

$$\delta W = \delta\left(\vec{u}^*\right)^T \left(K\vec{u}^* - F\right) = 0 \tag{4.25}$$

Finally since the variations are arbitrary, equilibrium can be satisfied by forcing $K\vec{u}^* - F$ to vanish. Thus the famous general system of equations for the finite element formulation:

$$K\vec{u}^* = F \tag{4.26}$$

4.2 Pre-Stress Axisymmetric FEM Wound Roll Model

The general finite element equations for the pre-stress formulation of an axisymmetrical solid body have been written. The axisymmetrical wound roll formulation is based on the accumulation of the web layers as concentric hoops. To solve the complete winding problem as the roll is wound from the core to the final radius requires the solution for the incremental strains and stresses that resulted from the addition of each layer. These increments are summed within each layer to produce the total strains and stresses in that layer. Most web materials have a radial modulus which is dependent on pressure that requires the material properties to be updated as a function of the total pressure after a layer is added. A general geometric view of wound roll model is given in Figure 1. Identical rectangular elements aligned along the *z* direction for represent a layer. Since all elements in this case are identical this configuration would correspond to a uniform thickness case. By employing elements with different side heights in the radial direction, a non-uniform web thickness case across *z* direction can be modeled.

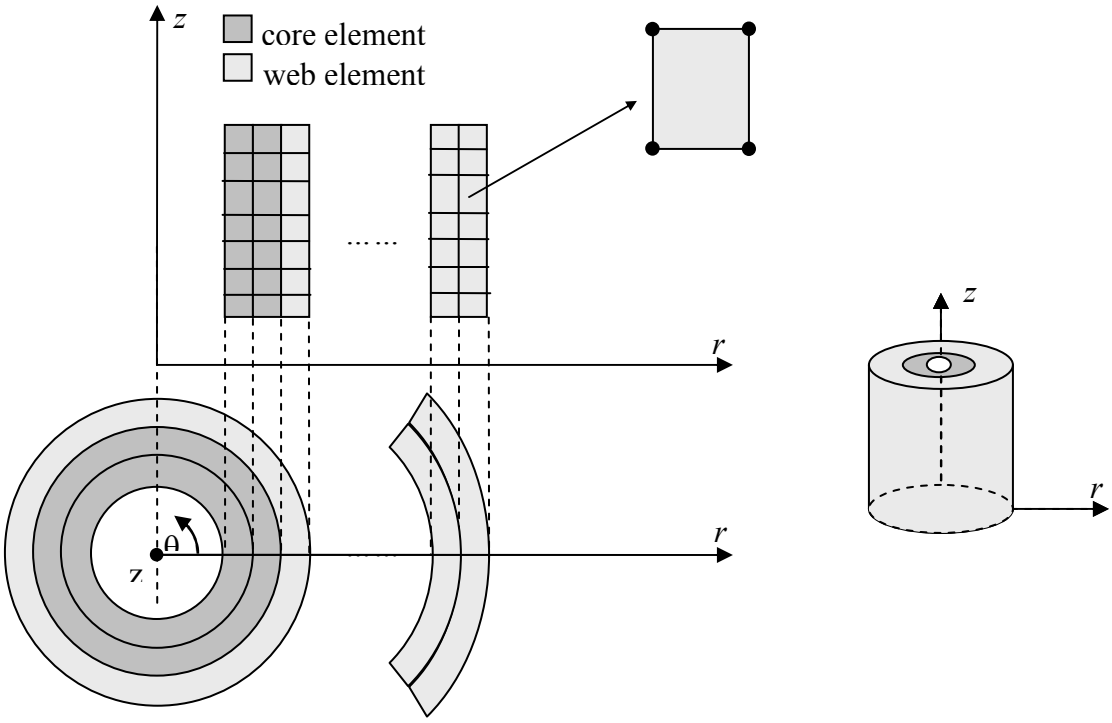

Figure 4.1 Modeling of Wound Rolls with Axisymmetric Finite Elements

Most webs are quite thin and the assumption that the stresses are nearly constant throughout the element is reasonable. Quadrilateral elements are optimum in terms of computational time and accuracy and thus were chosen. A typical element has 4 nodes at the corners with linear sides connecting them. Instead of defining the element in the (r,z) coordinate system a natural coordinate system (η,ξ) will be employed which simplifies numerical integration. An isoparametric formulation was employed. This means that the shape functions used to map the element deformations are identical to the functions which define the transformation from original to natural coordinate system. A general quadrilateral element in (r,z) and its mapped counterpart in (η,ξ) coordinates are shown in Figure 2. The related mathematical operations are briefly defined below.

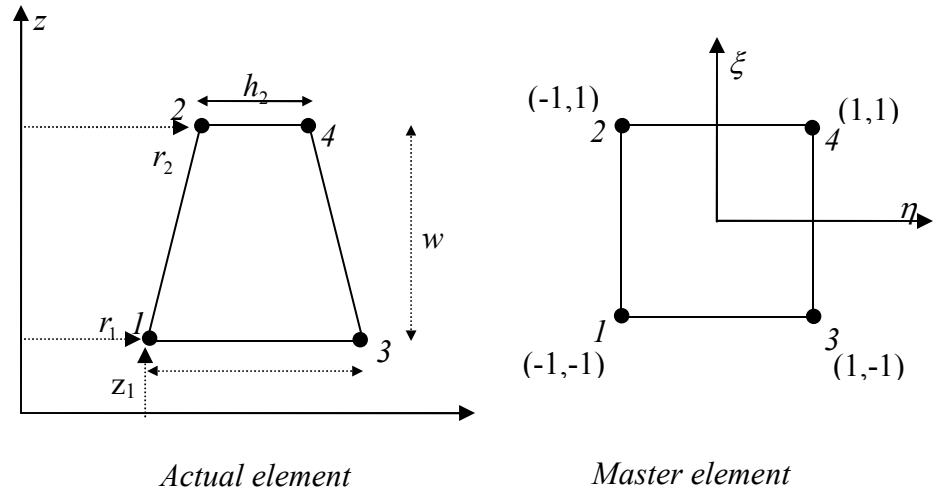

Figure 4.2 Actual r-z and Natural η-ξ Coordinates for and Axisymmetric Finite Element

The actual coordinates of a point within the element are expressed in terms of nodal coordinates and shape functions. The (r,z) coordinates of the nodes are:

$$\vec{r} = \left[r_1, r_2, r_1 + h_1, r_2 + h_2\right]^T \tag{4.27}$$

$$\vec{z} = \left[z_1, z_1 + w, z_1, z_1 + w\right]^T \tag{4.28}$$

The (r,z) coordinates of a point inside the domain of the quadrilateral element are:

$$r(\eta,\xi) = \sum_{j=1}^{4} \bar{r}_j \phi_j(\eta,\xi) \tag{4.29}$$

$$z(\eta,\xi) = \sum_{j=1}^{4} \bar{z}_j \phi_j(\eta,\xi) \tag{4.30}$$

For quadrilateral elements the shape functions are easily written in terms of the natural coordinates:

$$\{\Phi\} = \begin{Bmatrix} \phi_1 \\ \phi_2 \\ \phi_3 \\ \phi_4 \end{Bmatrix} = \begin{Bmatrix} \frac{1}{4}(1-\xi)(1-\eta) \\ \frac{1}{4}(1-\xi)(1+\eta) \\ \frac{1}{4}(1+\xi)(1-\eta) \\ \frac{1}{4}(1+\xi)(1+\eta) \end{Bmatrix} \tag{4.31}$$

With shape functions defined the Jacobian J and its inverse J^{-1} can be formed.

$$\begin{bmatrix} \frac{\partial \phi}{\partial \eta} \\ \frac{\partial \phi}{\partial \xi} \end{bmatrix} = \begin{bmatrix} \frac{\partial r}{\partial \eta} & \frac{\partial z}{\partial \eta} \\ \frac{\partial r}{\partial \xi} & \frac{\partial z}{\partial \xi} \end{bmatrix} \begin{bmatrix} \frac{\partial \phi}{\partial r} \\ \frac{\partial \phi}{\partial z} \end{bmatrix} = [J] \begin{bmatrix} \frac{\partial \phi}{\partial r} \\ \frac{\partial \phi}{\partial z} \end{bmatrix} \tag{4.32}$$

$$J^{-1} \begin{bmatrix} \frac{\partial \phi}{\partial \eta} \\ \frac{\partial \phi}{\partial \xi} \end{bmatrix} = \begin{bmatrix} \frac{4}{(1-\xi)h_1 + (1+\xi)h_2} & 0 \\ \frac{2\left[(1+\eta)(h_1 - h_2) + 2(r_1 - r_2)\right]}{w\left[(1-\xi)h_1 + (1+\xi)h_2\right]} & \frac{2}{w} \end{bmatrix} \begin{bmatrix} \frac{\partial \phi}{\partial \eta} \\ \frac{\partial \phi}{\partial \xi} \end{bmatrix} = \begin{bmatrix} \frac{\partial \phi}{\partial r} \\ \frac{\partial \phi}{\partial z} \end{bmatrix} \tag{4.33}$$

Components of the inverted Jacobian are used for the transformation of derivatives in the D matrix.

$$D^* = \begin{bmatrix} J_{11}^{-1}\frac{\partial}{\partial \eta} + J_{12}^{-1}\frac{\partial}{\partial \xi} & 0 \\ 0 & J_{21}^{-1}\frac{\partial}{\partial \eta} + J_{22}^{-1}\frac{\partial}{\partial \xi} \\ J_{21}^{-1}\frac{\partial}{\partial \eta} + J_{22}^{-1}\frac{\partial}{\partial \xi} & J_{11}^{-1}\frac{\partial}{\partial \eta} + J_{12}^{-1}\frac{\partial}{\partial \xi} \\ \frac{1}{r(\eta,\xi)} & 0 \end{bmatrix} \tag{4.34}$$

The transformation of the integral for the element stiffness matrix is completed by substituting D^* instead of D and converting the infinitesimal volume element dV_e to the natural coordinates.

$$B = D^{*}\Phi \tag{4.35}$$

$$dV_e = 2\pi \det[J] r d\eta d\xi \tag{4.36}$$

$$K_e = 2\pi \int_{-1}^{1}\int_{-1}^{1} B^T M_e B \det[J] r d\eta d\xi \tag{4.37}$$

These elemental stiffness terms will be evaluated by employing numerical integration. In this case Gauss Quadrature with 2X2 Gauss points was used for computational efficiency and accuracy. Here the *(p,s)* component of 8x8 axisymmetrical quadrilateral element stiffness matrix is shown:

$$\left(K_e\right)_{ps} = 2\pi \sum_{q=1}^{2}\sum_{j=1}^{2} \omega_q \omega_j B^{t}_{pk(g_q,g_j)} \left(M_e\right)_{kl} B_{ls(g_q,g_j)} r(\eta,\xi) \det[J]_{(g_q,g_j)} \tag{4.38}$$

where ω_q and ω_j are the Gauss weights for the q^{th} Gauss point in the η direction and j^{th} Gauss point in the ξ direction, respectively. The parenthesizes denote the associated value is calculated at the (g_q, g_j) Gauss point. A similar calculation is carried out for the elemental force vector.

$$F_e = -2\pi \int_{-1}^{1}\int_{-1}^{1} B^{t}\sigma_0 \det[J] r d\eta d\xi \tag{4.39}$$

$$\left(F_e\right)_p = -2\pi \sum_{q=1}^{2}\sum_{j=1}^{2} \omega_q \omega_j B^{t}_{pk(g_q,g_j)} \left(\sigma_0\right)_k r(\eta,\xi) \det[J]_{(g_q,g_j)} \tag{4.40}$$

Web materials also exhibit state dependent behavior. The radial modulus of elasticity E_r is a function of the radial stress σ_r. One of the most common constitutive relations used is the model of Pfeiffer. He proposed to establish the the following expression for E_r:

$$E_r = K_2(-\sigma_r + K_1) \tag{4.41}$$

Here K_2 and K_1 are Pfeiffer's material constants which are obtained via stack compression experiments for a particular material. Taking into account Maxwell relations, the elastic compliance matrix C which is the inverse of M can be given explicitly as:

$$\{\varepsilon\} = \begin{Bmatrix} \varepsilon_r \\ \varepsilon_z \\ \gamma_{rz} \\ \varepsilon_\theta \end{Bmatrix} = \begin{bmatrix} 1/E_r & -\nu_{rz}/E_z & 0 & -\nu_{r\theta}/E_\theta \\ -\nu_{rz}/E_z & 1/E_z & 0 & -\nu_{z\theta}/E_\theta \\ 0 & 0 & 1/G_{rz} & 0 \\ -\nu_{r\theta}/E_\theta & -\nu_{z\theta}/E_\theta & 0 & 1/E_\theta \end{bmatrix} \begin{Bmatrix} \sigma_r \\ \sigma_z \\ \tau_{rz} \\ \sigma_\theta \end{Bmatrix} = [C]\{\sigma\} \tag{4.42}$$

$$M = C^{-1} \tag{4.43}$$

Each finite element will have a different radial modulus E_r depending on the radial stress in that element. This situation makes the problem nonlinear and requires utilizing linearization techniques. Rather then using more complicated and processor time consuming Newton-Raphson methods an ad-hoc approach which is very compatible and sufficient assumes E_r of all elements remain at constant levels during the addition a layer. The system of linear finite element equations can be solved and the incremental stresses due to the addition of the most recent layer can be calculated. Finally the stress state of all elements was updated using the incremental stresses and using the updated stresses E_r for all elements is updated prior to the addition of the next web layer.

This completes the finite element formulation of the problem. Now the appropriate initial stress vector for the simulation of the winding must be defined. Figure 4.3 shows a typical instance during a winding simulation of a nonuniform thickness web.

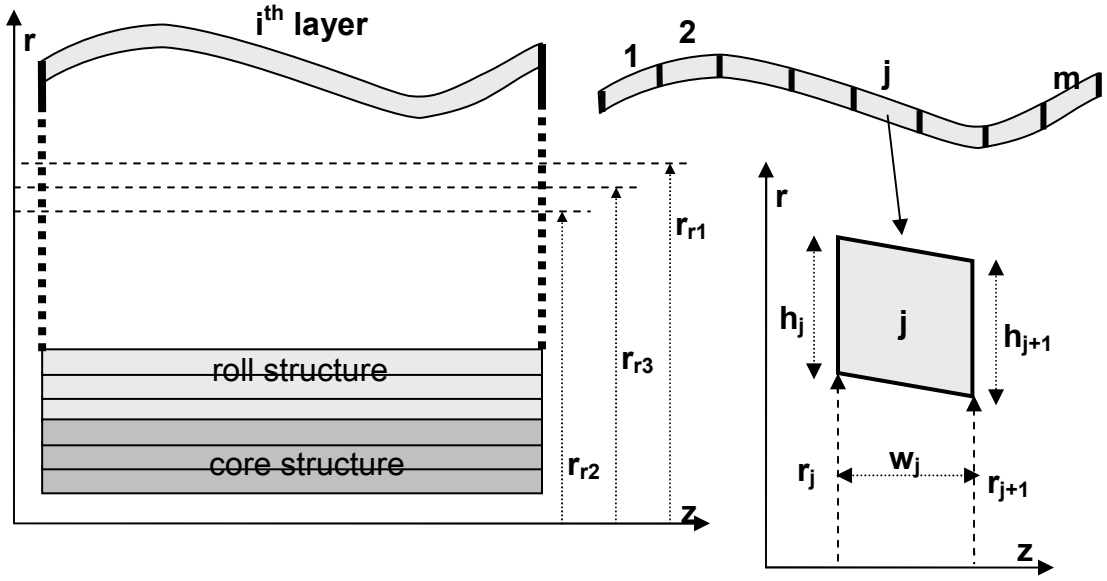

Figure 4.3 Treatment of the Outer Lap using a Pre-Stress Formulation

The nonuniform web thickness in the cross machine direction (CMD) results in nonuniform profile in radius across the roll width. This radius profile will vary as the wound roll is wound. Wound rolls may be comprised of hundreds to thousands of layers and if the widthwise web thickness variation persists in the machine direction (MD) large variations in the radius of the outer lap across the roll width can occur. Thus the tension will vary in the outermost layer depending on the CMD position. CMD positions with higher radial profiles should be subject to greater tangential stress and vice versa. In order to simulate this effect in a mechanically consistent manner the notion of a relaxation

radius, first coined by Hakiel, will be employed. If it was possible to extract the outer layer from a wound roll and allow it to relax to a stress free state, the radius of the undeformed cylinder of web would be the relaxation radius. Given the relaxation radius for a given roll profile the corresponding strains for all CMD positions can be computed. In a first attempt to calculate the relaxation radius for a given roll profile and web line stress T_w the mechanical equilibrium of the outer winding layer is established:

$$T_w \sum_{j=1}^{m} A_j = \sum_{j=1}^{m} E_{\theta j} \int_0^w \int_{f_1^j(z)}^{f_2^j(z)} \frac{r - r_r}{r_r} dr dz \tag{4.44}$$

Here A_j and $E_{\theta j}$ are the area and tangential modulus of elasticity for the j^{th} sector, respectively. The integrand is the strain of a radial position in the j^{th} sector so multiplying by $E_{\theta j}$ and integrating over the sector gives the total tangential force contribution of j^{th} sector. A_j and the integral can be expressed explicitly as below:

$$A_j = w \frac{h_j + h_{j+1}}{2} \tag{4.45}$$

$$\int_0^w \int_{f_1^j(z)}^{f_2^j(z)} \frac{r - r_r}{r_r} dr dz = \frac{w}{6r_r}\left(h_j h_{j+1} + h_j^2 + h_{j+1}^2 + 2r_j h_j + 2r_{j+1} h_{j+1} + r_j h_{j+1} + r_{j+1} h_j\right) - w\left(\frac{h_j + h_{j+1}}{2}\right) \tag{4.46}$$

Here the width of a typical sector is denoted as *w* and it is taken constant. r_r is the unknown relaxation radius which is assumed to satisfy tangential mechanical equilibrium of the winding layer. After algebraic manipulations the relaxation radius r_r is obtained as below:

$$r_r = \frac{\sum_{j=1}^{m} E_{\theta j} Y_j}{T_w \sum_{j=1}^{m} h_j^{ave} + \sum_{j=1}^{m} E_{\theta j} h_j^{ave}} \tag{4.47}$$

Where

$$Y_j = \frac{1}{6}\left(h_j h_{j+1} + h_j^2 + h_{j+1}^2 + 2r_j h_j + 2r_{j+1} h_{j+1} + r_j h_{j+1} + r_{j+1} h_j\right) \tag{4.48}$$

$$h_j^{ave} = \frac{h_j + h_{j+1}}{2} \tag{4.49}$$

This calculated relaxation radius then can be used to calculate the initial stresses of each sector. Here the initial stress vector is obtained and is shown to depend on the calculated relaxation radius as a function of radial position in terms of natural coordinates:

$$\left(\sigma_0\right)^j = \left[0 \quad 0 \quad 0 \quad E_{\theta j} \frac{r_j(\eta,\xi) - r_r}{r_r}\right]^t \tag{4.50}$$

Where

$$r_j(\eta,\xi) = \frac{(1+\eta)(1-\xi)h_j + (1+\eta)(1+\xi)h_{j+1} + 2(1-\xi)r_j + 2(1+\xi)r_{j+1}}{4} \tag{4.51}$$

This initial stress in a vector form is for the j^{th} sector. It can be used in the calculation of corresponding nodal load forces using the elemental force vector:

$$\left(F_e\right)_p = -2\pi \sum_{q=1}^{2} \sum_{j=1}^{2} \omega_q \omega_j B^t_{pk(g_q,g_j)} \left(\sigma_0\right)_{k(g_q,g_j)} r_{(g_q,g_j)} \det[J]_{(g_q,g_j)} \tag{4.52}$$

This procedure is applied to all elements (sectors) of the winding layer and the resulting elemental load vectors are assembled into a system force vector using the direct stiffness

assembly method. The resulting system of equations is solved and the corresponding unknown incremental displacements are obtained for all layers in the roll structure. Incremental strains and stresses are then computed for the addition of the most recent layer. Since there was no assumed radial compaction of the roll structure when the relaxation radius was computed, the resulting average tangential stress will be lower than the input T_w. This is the result of tension loss. The outer winding layer looses some of its tangential stress as the roll deforms inward beneath it. The degree to which this occurs depends on the radial modulus of the web being wound and the winding tension level. Webs with a high radial modulus will exhibit very little tension loss and the average tangential stress in the outer lap will approach the web line stress T_w.

If it is desired to force the average tangential stress in the outer lap to equal the web line stress T_w a procedure to iterate the relaxation radius of the outer lap is required. The first calculated relaxation radius will be denoted r_{r1}. The first average tangential stress of the outer winding layer calculated via finite element equations will be denoted $T_{\theta 1}$. A smaller relaxation radius than r_{r1} will result in greater average tangential stress so that a second iteration for the relaxation radius, r_{r2}, can be given as:

$$r_{r2} = r_{r1}\frac{T_w}{T_{\theta 1}} \tag{4.53}$$

After the second relaxation radius r_{r2} is used in the finite element calculations as r_{r1} and solving the resulting equations the average tangential stress $T_{\theta 2}$ for r_{r2} can be obtained. Finally using the first and second approximations for the relaxation radius linear interpolation can be used to solve for the third relaxation radius which would be expected

to produce an average tangential stress in the outer layer in the tangential direction equal to the web line stress:

$$r_{r3} = r_{r1} + \frac{T_w - T_{\theta 1}}{T_{\theta 2} - T_{\theta 1}}(r_{r2} - r_{r1}) \tag{4.54}$$

When the third relaxation radius is input to the finite element code it is found that the average tangential stress is approaching the web line stress (i.e. $\left|T_w - T_{\theta 3}\right| \le c$ and c is typically on the order of 10^{-4}x T_w).

4.3 Comparison of Results and Discussion

To benchmark the current axisymmetric codes a comparison with 2D model and test data reported by Cole and Hakiel[17]. The model results are taken from a code developed based on those described by Cole and Hakiel [17]. The test data consists of core pressure data and profilometer data taken to establish the variation in the outer lap radius. The core pressure data was taken on a core composed of ring segments. The segments were composed from aluminum and were 2.54 cm (1 in) wide and had an inside radius of 6.03 cm (2.375 in) and an outside radius of 6.35 cm (2.5)". Each ring segment was supported on pins such that the ring could deform inward axisymmetrically and also transmit the torque required to wind the roll. The ring segments were instrumented with strain gages and these strain measurements allowed the applied core pressure to be inferred. The web used in these tests was a 25.4 cm (10 in) wide polyester film which was nominally 101.6 μm (0.004 in) thick. There were two samples, Case A and B, each having a unique thickness variation across the web width. The traces for the thickness for each Case are shown in Figures 5 and 6. The modeling will employ 20 elements of uniform width and

thus the thickness is estimated at 21 positions equally spaced across the web width as shown in Figures 4.4 and 4.5.

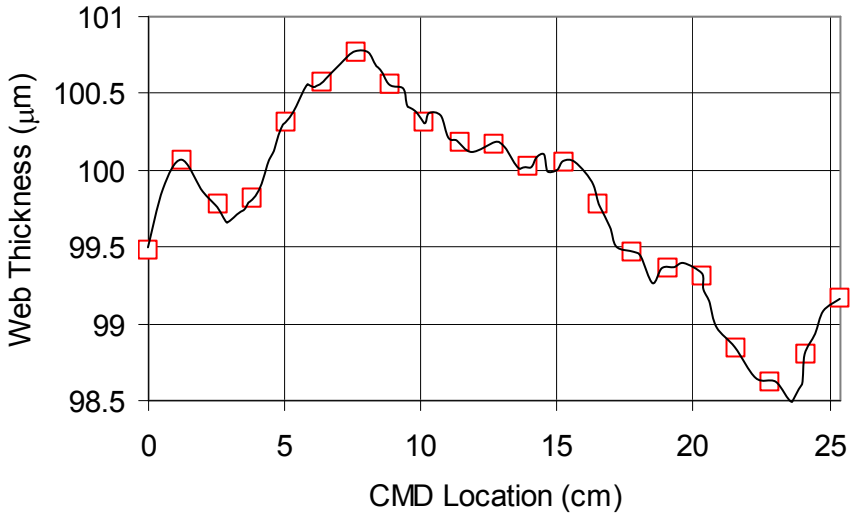

Figure 4.4 Hakiel and Cole – Thickness Case A

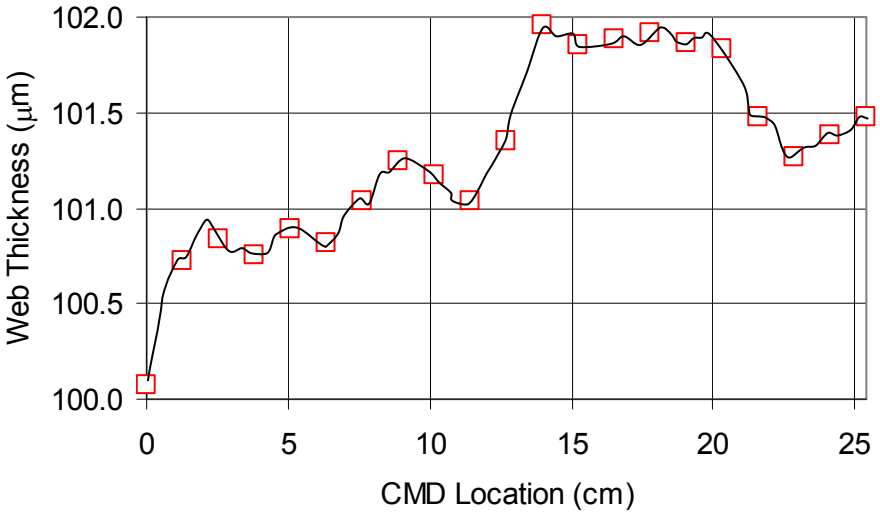

Figure 4.5 Hakiel and Cole – Thickness Case B

The remaining parameters required to run the models are given in Table 4.1. All of these parameters were extracted from Cole and Hakiel [17] except for the in-plane value of Poisson's ratio ($\nu_{\theta z}$) which was assumed and the shear modulus of rigidity G_{rz}. The shear modulus was assumed to be state dependent on radial stress through the radial modulus (E_r) as shown. This assumption was proven valid in other research [8].

Core Diameter	12.7 cm
Finish Roll Diameter	38.1 cm
E_θ, E_z	4.339 GPa
E_r	$E_r = K_1(1 - e^{\sigma_r / K_2})$
K_1	2.4949 GPa
K_2	8.6496 GPa
$\nu_{r\theta}$, ν_{rz}	0.01
$\nu_{\theta z}$	0.3
G_{rz}	$2E_r$
T_w, nominal winding stress	6.863 MPa

Table 4.1 Winding Model Input Parameters

4.3.1 Core Pressure Comparison

The model results that will be compared include results from Hakiel and Cole's formulation and the Pre-Stress formulations presented herein. These results will be compared to the core pressure test results presented by Cole and Hakiel [17].

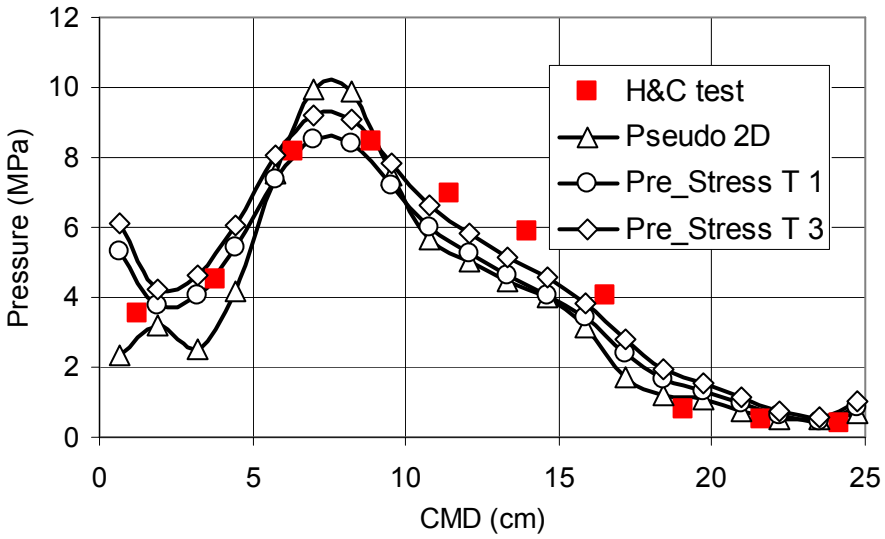

Figure 4.6 Core Pressure Comparison – Case A

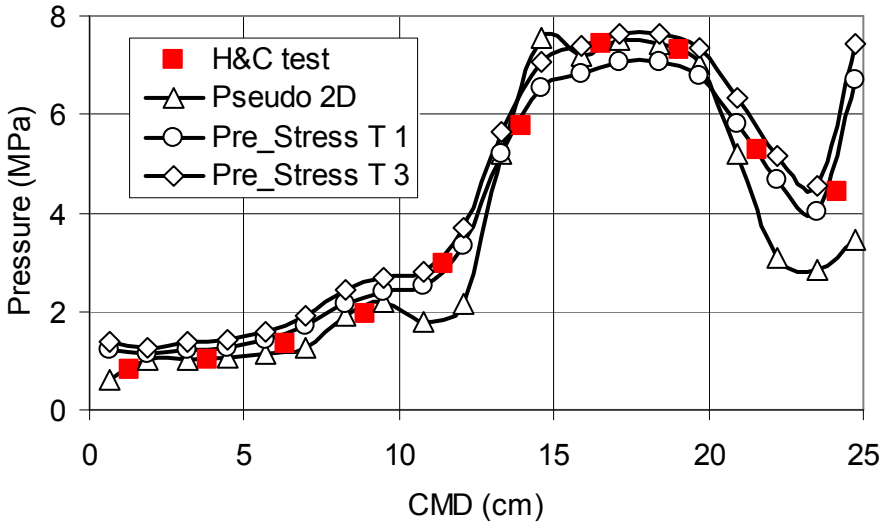

Figure 4.7 Core Pressure Comparison – Case B

The Pseudo 2D code developed were developed based upon papers written by Cole and Hakiel [17]. When comparing the core pressures predicted by the models it should be

noted that all models compare reasonably well with the core pressure test data. If the core rings that compose the core were deflecting appreciably this comparison would not be legitimate. This is because the axisymmetric wound roll models assume the core is a cylinder which is continuous over the web width. The Pseudo 2D models assume a segmented core and a segmented web. The reality of the test was a segmented core and a web that was continuous over its width. For Case A all the models yield less pressure than the test values in the 10 to 17 cm range of CMD location. As a measure of performance of the models compared to the test data the mean absolute error was evaluated and the results are shown in Table 4.2. Overall the axisymmetric Pre-Stress solutions compared the best with the test data. This polyester film has a very high radial modulus and only a small amount of tension loss would be expected. Thus the results from the Pre-Stress $T_{\theta 1}$ and $T_{\theta 3}$ solutions should not have been appreciably different. It is interesting that the Pseudo 2D model and the axisymmetric Pre-Stress yield results that are so similar given that the model developments are so different.

Model	Pseudo 2D	Pre-Stress $T_{\theta 1}$	Pre_Stress $T_{\theta 3}$
Case A	0.83	0.73	0.72
Case B	0.45	0.31	0.51

Table 4.2 Mean Absolute Errors

4.3.2 Outer lap Comparison

A comparison of the radius variation with respect to the cross machine direction is presented in Figures 4.8 and 4.9 for Cases A and B, respectively. The model results all agree quite well with one another. The model results show the same trends as the test data

but the range of radius from the model results is nearly twice that of the test data for Case A although there is better agreement for Case B.

It is also interesting to compare the model results in Figures 4.8 and 4.9 with the thickness traces presented for Cases A and B in Figures 4.4 and 4.5, respectively. Note the trends in measured thickness follow the trends in the outer lap radius predicted by the models. Based upon use of the models alone this might lead to the conclusion that the outer lap radius is entirely dependent on the web thickness variation across the web width. If the trends in measured thickness in Figures 5 and 6 are compared to the measured outer lap radius in Figures 4.8 and 4.9 less correlation is apparent. There are some features in the outer lap radius data that appear to repeat with a period close to 2.54 cm, the width of the core rings. It is possible that the independent deformations of the core rings had some impact on the outer lap radius variation across the web width.

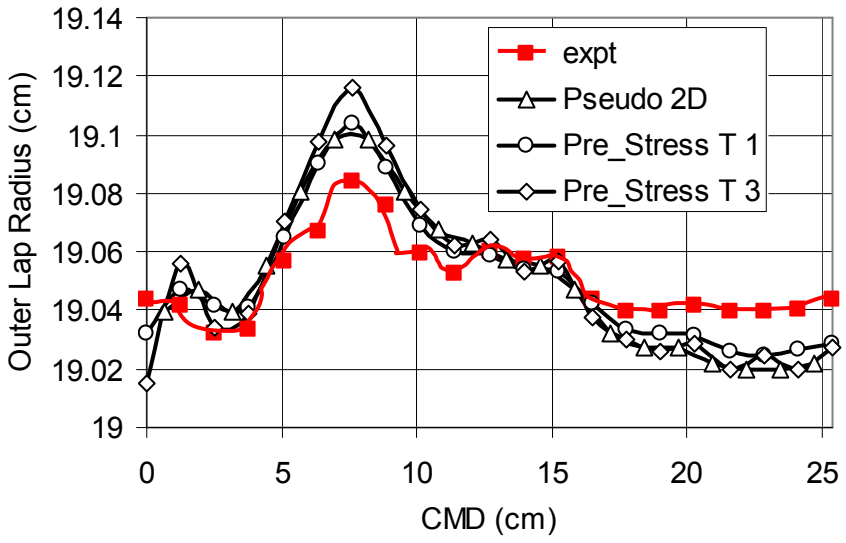

Figure 4.8 Outer Lap Radius Comparison – Case A

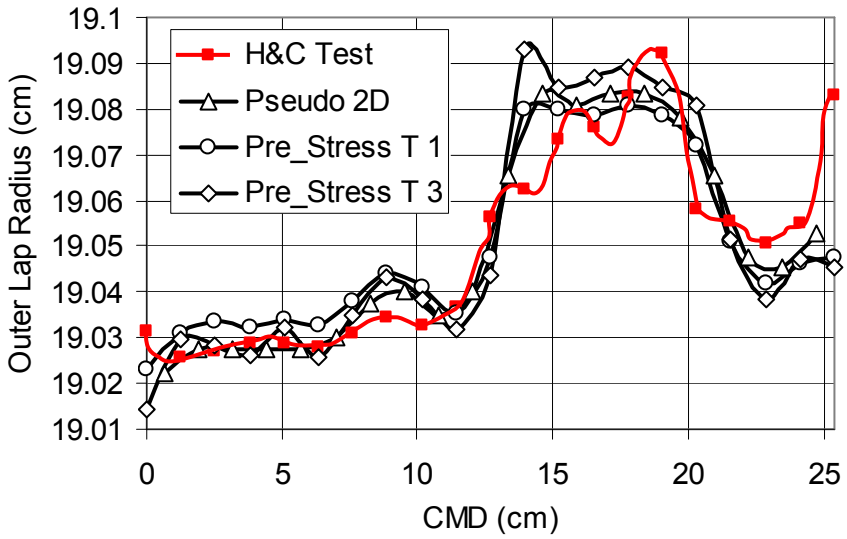

Figure 4.9 Outer Lap Radius Comparison – Case B

4.3.3 Axisymmetric Stresses

The stresses computed by the axisymmetric model include radial, tangential, axial and shear stress components. For Hakiel and Cole's Case B these stresses are shown in Figures 4.10,4.11,4.12, and 4.13.

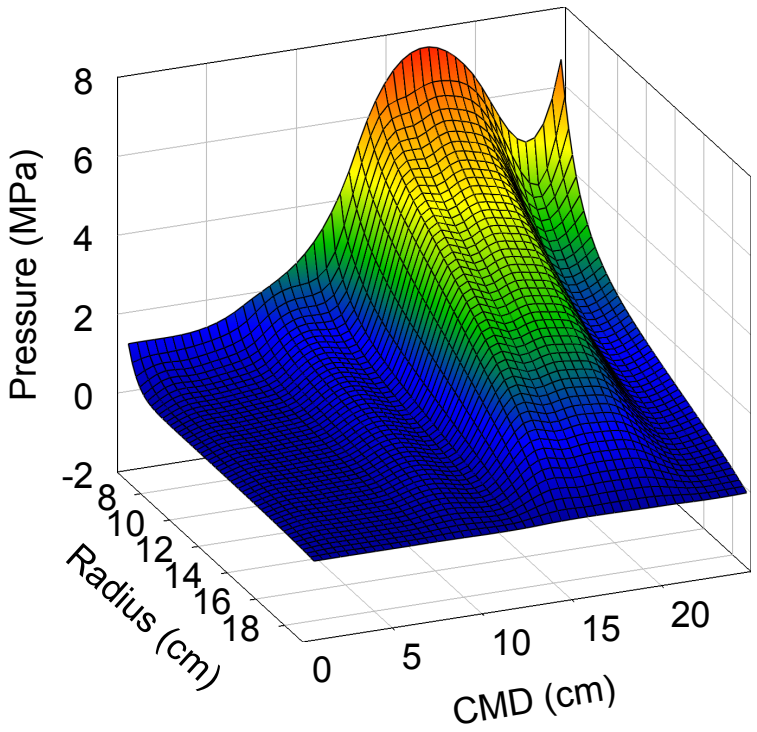

Figure 4.10 Pressure ($-\sigma_r$) – Case B

The pressures witnessed by this roll peak at 7.64 MPa (1110 psi). Whether these pressures result in roll and web defects are determined largely by the web surface characteristics and the coatings. Pressures of this magnitude could certainly cause core failures in fiber cores. One of the benefits of an axisymmetric winding model is that a model of an axisymmetric orthotropic core is readily incorporated.

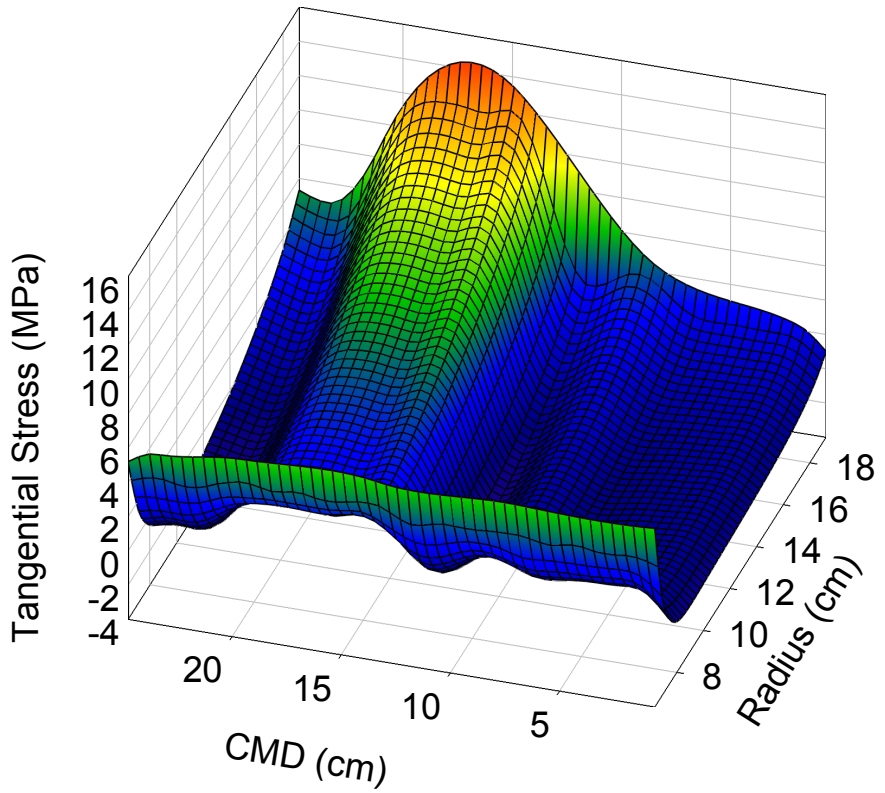

Figure 4.11 Tangential Stresses – Case B

The peak tangential stress is 15.4 MPa (2240 psi) in the outer lap. The yield stress of polyester is approximately 55 MPa (8000 psi). Thus this stress level may be acceptable as long as the roll is not stored at elevated temperature. The peak tangential stress would have become higher had the roll been wound to a larger radius. The 15.4 MPa peak stress was due to the variation in the outer lap radius that was shown in Figure 4.9. Had the roll been wound to a larger final radius the variation in the outer lap radius across the roll width would have increased and resulted in an even higher peak tangential stress. Thus these models are useful for determining how large a roll can be wound for given thickness variation prior to subjecting the web to tangential stresses that will induce inelastic deformation or web breaks. Inelastic deformation is undesirable because that

deformation will be nonuniform and will peak wherever the tangential stresses peak. When this web is unwound a baggy center will appear.

The axial stresses are shown in Figure 4.12. Axial stresses cannot be computed using Pseudo 2D models because each of the 1D sector models employ plane stress assumptions (i.e. $\sigma_z=0$). Note for the example given that the peak stresses are negative and are seen in the vicinity of the core. This is a case where the lateral growth of the web is being confined by the core. If the web and the core had properties that were more similar the peak negative axial stresses near the core would decrease and become less negative. Again these models are valuable in deciding what core properties are optimal. Another minimum is seen closer to the surface of the roll. The web width in the free span upstream of the winder is contracted due to the Poisson effect and web tension. After that web enters the wound roll and becomes the outer layer the circumferential stress decreases as more layers are wound onto the roll, refer to Figure 4.11. As the tangential stresses decrease the web width attempts to expand in the cross machine direction but is constrained by the frictional contact between layers and hence compressive axial stresses develop. If these stresses become to negative axial buckles or corrugations can appear which may be detrimental to roll quality.

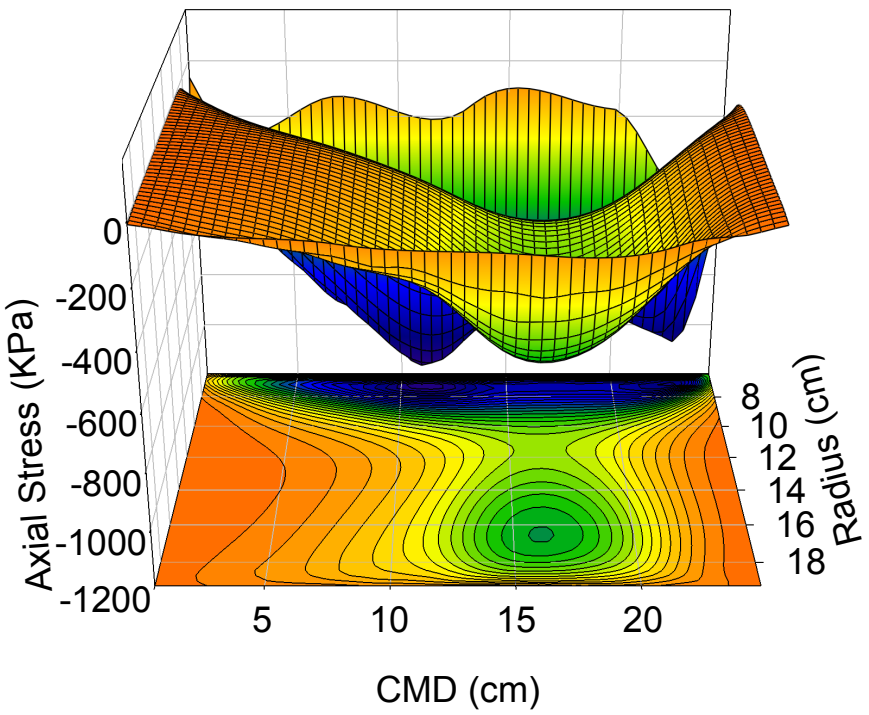

Figure 4.12 Axial Stresses – Case B

It is possible to develop 1D winding models using plane strain assumptions that could develop axial stresses and could be incorporated into a Pseudo 2D model. The difficulty is establishing a criterion that would determine when plane stress conditions exist and when plane strain conditions exit. One of the benefits of the axisymmetric finite element wound roll models is that no such assumptions need to be made. Note that in Figure 4.12 that the axial stresses dissipate to zero at the roll edges (i.e. CMD=0 and 25.4 cm) as dictated by surface equilibrium. Elements which border the edges are subject to near plane stress conditions. Elements in the interior region do attain various levels of axial stress (σ_z) but are not necessarily under plane strain conditions unless the axial strain (ε_z) is zero. Most of the elements in the interior are not in either plane stress or plane strain conditions.

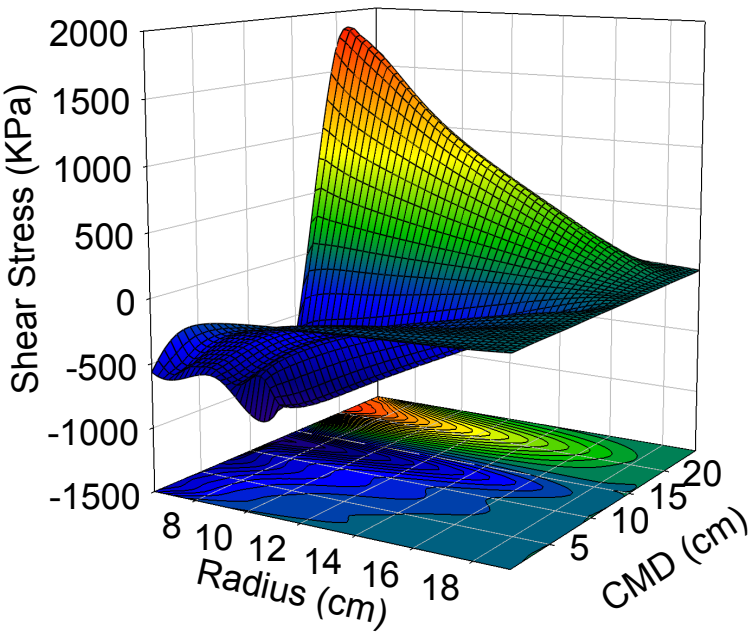

Figure 4.13 Shear Stresses – Case B

The shear stresses associated with this example are shown in Figure 14. They too cannot be calculated using the Pseudo 2D models, again due to the plane stress assumption which forces all stress components with an axial or z direction to be zero (i.e. $\sigma_z=0$, $\sigma_{rz}=0$). The shear stresses are largest in the vicinity of the core, again due to the vast difference in material properties between the core and the web. They dissipate to near zero levels at the roll edges and at the final lap as is dictated by surface equilibrium.

4.3.4 Conclusions

The results of Pseudo 2D model and the axisymmetric Pre-Stress model agree very well in terms of core pressure and the variation in radius of the outer lap. Both models compare nicely to the core pressure measurements taken by Cole and Hakiel [17]. Both models capture the trends but not the detail of the measured variation in radius of the outer lap. Additional tests should be performed on web with thickness variation wound

on non-segmented cores to determine if the core ring deformations were responsible for the discrepancy.

The Pre-Stress axisymmetric model formulation is optimal because only one solution step is required to achieve results where tension loss is allowed to occur. If one wishes to impose the constraint that the web line stress be equivalent to the average tangential stress in the outer lap then a three step solution process is required.

The stress results from axisymmetric models are important not because they are necessarily more accurate than that of previous models but because the additional stresses computed can allow other types or roll defects to be studied and prevented.

Finally this new pre-stress type formulation is proven to be computationally efficient and accurate so that it can be used as the axisymmetric wound roll model (AWM) for the combined model.

5. NIP and WOUND ROLL CONTACT MODEL

In this chapter we model a 2D-plane formulation of the contact of a nip and a wound roll. The nip and roll are treated as perfect cylinders. The Roll cylinder is modeled with a nonlinear material model including a pressure dependent modulus. Nip cylinder is modeled as a rigid cylinder for the sake of simplicity. In fact this approach is an idealization of steel which can be modeled as a rigid body when compared to the wound roll. Before analyzing this case we will analyze the diametral compaction of a cylinder between rigid surfaces for comparison with literature [39].

5.1 Contact Model

The contact model is depicted in figure 5.1.We begin with some simplifications for the contact problem. As seen from figure 5.1, because of symmetry of the problem, only half of the system needs to be modeled. A further simplification is possible if we consider that the contact effects are localized near the contact region so only one quarter is sufficient to model the system.

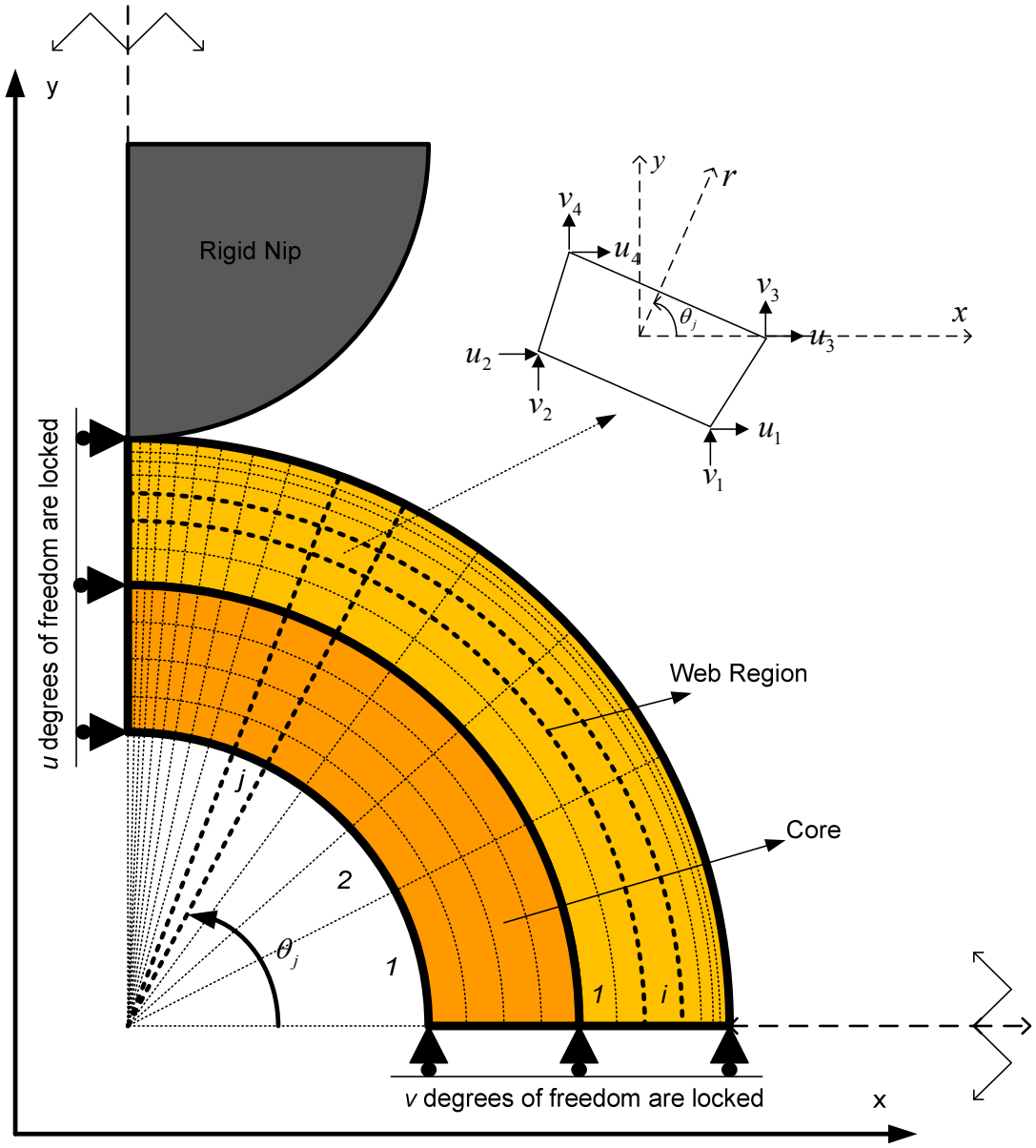

Figure 5.1 Contact Model

In figure 5.1 the finite element composition is also shown. We used quadrilateral 2D plane stress finite elements in the formulation. Since most of the deformation occurs around contact the region and the sharp gradients of the physical quantities are expected

to occur in this region we employ double refinement in the mesh along radius and tangential directions toward to the contact region. The quadrilateral master elements are formulated in the Cartesian coordinate system. This requires transforming the material matrix of a typical element during calculations in order to enforce cylindrical material symmetry. Transforming the material matrix of the elements, at first glance, is computationally undesirable. Despite this disadvantage Cartesian formulation has a distinct advantage over cylindrical formulation in resembling the rigid body modes of the elements. Cartesian shape functions are complete in terms of resemblance of the rigid body modes of the elements where as cylindrical shape functions are not. Because of this one should use a much higher mesh density in a cylindrical formulation in order to obtain same degree of accuracy as a Cartesian formulation.

5.2 Finite Element Formulation of Contact

The 2D finite element formulation of the cylindrical body begins with mesh generation. The mesh generation consists two parts. The first part is the uniform mesh generation of the core structure and the second part is the refined mesh generated for the roll region. We employ mesh refinement in the radial and tangential directions in the roll region. The mesh refinement implementation is done by using a geometric series written in terms of the maximum number of elements in the radial and tangential directions. The geometrical quantity (length, angle) under consideration is divided in to segments with a successive geometrical rate relation. As seen in figure 5.2 if we denote H as the geometrical quantity (in the figure it is depicted as length) to be divided into segments and n as the number of segments then with a given factor k the relation is expressed as:

$$H = h + kh + k^2 h + ... + k^{n-1} h \quad \text{or simply} \quad H = h\sum_{i=0}^{n-1} k^i \tag{5.1}$$

Here h is the geometrical value of the first segment and geometrical value of the $i^{\text{th.}}$ segment is $k^{i-1}h$. Obviously k should be selected between *0* and *1* to ensure refinement. The sum of geometrical sequence can be easily calculated:

$$H = h\frac{k^n - 1}{k - 1} \tag{5.2}$$

So h will be given by:

$$h = H \Big/ \left(\frac{k^n - 1}{k - 1}\right) \tag{5.3}$$

The first coordinate of a segment due to an origin can now be expressed. If we denote the first coordinate of $i^{\text{th.}}$ segment with x_i then:

$$x_i = h\frac{k^{i-1} - 1}{k - 1} \text{ or } x_i = H\frac{k^{i-1} - 1}{k^n - 1} \tag{5.4}$$

Setting k smaller and smaller than 1 will produce a more and more refined mesh as i the index increases. Since the relation is geometric, using more elements (increasing n) will result in disproportionally tiny elements at the end. (i.e. $i > j \rightarrow k^j h >> k^i h$). In order to prevent this and produce a more flexible mesh refinement we can also introduce a power factor p such that

$$x_i = H\left(\frac{k^{i-1} - 1}{k^n - 1}\right)^p \tag{5.5}$$

Here p is a predefined number like k and it is between *0* and *1*.

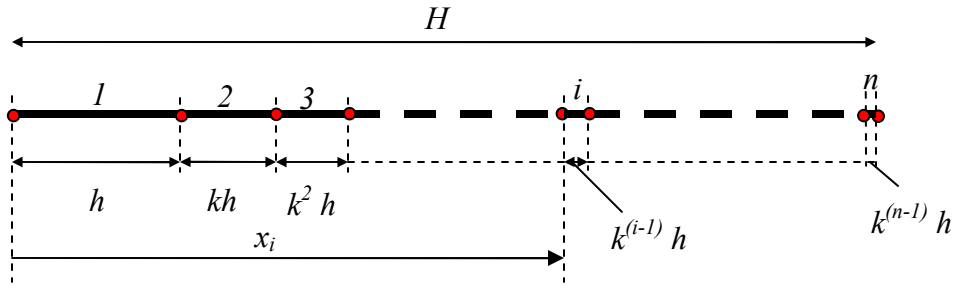

Figure 5.2 Refinement of a Line

Now the procedure is ready to apply to cylindrical mesh refinement. As mentioned before, there are mainly two quantities to be refined: First the radial thickness of roll the and second the $\pi/4$ radian angle of the quarter cylinder. If we denote the inner and outer radius with r_{in} and r_{out} respectively then the length to be refined will be $H=r_{out}-r_{in}$. If we use n_r sectors along radial direction then $i^{th.}$ radial position will be given as:

$$r_i = (r_{out} - r_{in})\left(\frac{k^{i-1}-1}{k^{n_r}-1}\right)^p + r_{in} \tag{5.6}$$

Angular refinement is done in similar way with $H=\pi/4$. If we use n_θ sectors along tangential direction then the $j^{th.}$ angular position will be given as:

$$\theta_j = \frac{\pi}{4}\left(\frac{k^{j-1}-1}{k^{n_\theta}-1}\right)^p \tag{5.7}$$

The coordinates of the refined mesh can be used to define elemental coordinates. We number the elements as shown in the figure. So the number of an element *(n.o.e)* is defined with its radial *(i)* and tangential *(j)* position:

$$n.o.e = (i-1)n_\theta + j \tag{5.8}$$

We used 4 node quadrilateral elements. The elemental coordinate vector which includes the Cartesian coordinates of the 4 nodes of the element for a typical element occupying the intersection of $i^{th.}$ radial and $j^{th.}$ tangential positions respectively can be given as

$$Q^{ij} = \begin{bmatrix} r_i \cos\theta_j & r_i \sin\theta_j & r_i \cos\theta_{j+1} & r_i \sin\theta_{j+1} & r_{i+1} \cos\theta_j & r_{i+1} \sin\theta_j & r_{i+1} \cos\theta_{j+1} & r_{i+1} \sin\theta_{j+1} \end{bmatrix}^t \tag{5.9}$$

The finite element formulation of plane problems is very similar to the formulation of axisymmetrical problems. The only difference is the definition of strain variables: plane problems lack hoop strain effects so the strain of an element e will be given by:

$$\varepsilon_e = \begin{bmatrix} \varepsilon_x & \varepsilon_y & \gamma_{xy} \end{bmatrix}^t \tag{5.9}$$

Here the component γ_{xy} is the engineering shear strain. We define displacement field's vector $\vec{u}_e = \begin{bmatrix} u_e(x,y) & v_e(x,y) \end{bmatrix}^t$. Here the first and second components are in the x and y direction respectively. The displacement field is represented in terms of interpolation of the nodal displacement values over an element:

$$\vec{u}_e = \Phi . \vec{u}_e^* \tag{5.10}$$

Here the nodal displacement vector and interpolation (similar to 4.31) matrix is given as:

$$\vec{u}_e^* = \begin{bmatrix} u_1 & v_1 & ..... & u_N & v_N \end{bmatrix}^t \tag{5.11}$$

$$\Phi = \begin{bmatrix} \phi_1 & 0 & ..... & \phi_N & 0 \\ 0 & \phi_1 & ..... & 0 & \phi_N \end{bmatrix} \tag{5.12}$$

The strain displacement relations are linked by the derivative matrix D:

$$D = \begin{bmatrix} \partial/\partial x & 0 & \partial/\partial y \\ 0 & \partial/\partial y & \partial/\partial x \end{bmatrix}^t \tag{5.13}$$

Using the derivative matrix D on the interpolated displacement field we get the strain vector in terms of nodal displacements:

$$\varepsilon_e = D\vec{u}_e \tag{5.14}$$

$$\varepsilon_e = (D\Phi)\vec{u}_e^* \tag{5.15}$$

$$B = D\Phi \tag{5.16}$$

Here B is denoted as the element strain-displacement matrix. In the same manner with the axisymmetrical formulation using B of the plane problems we can obtain the stiffness matrix of an element:

$$K_e = \int_e B^t M_e^{Cart.} B dV_e \tag{5.17}$$

Here $M_e^{Cart.}$ is the material matrix written with respect to Cartesian coordinates. We know that wound web materials exhibit axisymmetrical character. In order to model this we should employ a transformation for the material matrix written for cylindrical coordinates. Since we already know the orientation of a typical element it is easy to verify that

$$M_e^{Cart.} = R^t M_e^{Cyl.} R \tag{5.18}$$

Here R is the orthogonal matrix which represents the transformation. For the element occupying a *(i,j)* position it can be given as:

$$R = \begin{bmatrix} \cos^2\theta_j & \sin^2\theta_j & \sin 2\theta_j \\ \sin^2\theta_j & \cos^2\theta_j & -\sin 2\theta_j \\ -\sin 2\theta_j/2 & \sin 2\theta_j/2 & \cos 2\theta_j \end{bmatrix} \tag{5.19}$$

Beside this transformation since the original material matrix (written in cylindrical coordinates) includes a pressure dependent radial modulus the transformed matrix will also be pressure dependent. Thus it is crucial to employ a solution technique in order to correctly solve this materially nonlinear problem. This will be discussed in the "Contact Algorithm" section. The system stiffness matrix is formed from element stiffness matrices as is usual in the finite element assembly procedure. We have employed multi point constraints via a penalty formulation in order to enforce geometrical boundary conditions. Due to the penalty formulation a penalty number *(β)* is added to the appropriate components of the global stiffness matrix. Here we define the procedure briefly. As seen from figure boundary conditions arising from symmetry of problem requires preventing vertical movement of nodes at the bottom and horizontal movement of nodes at the left side of cylinder. Without losing generality if we denote one of these dof as q_i then the penalty formulation requires that a $\beta q_i^2/2$ term should be added to total potential energy of the system. Minimizing this augmented potential energy will introduce an additional term βq_i and this additional term requires us to add β to the *(i,i)* position of the global stiffness matrix. This generic procedure will apply to all boundary conditions of this type and we simply add the number β to the diagonal positions of the related dof.

5.3 Contact Algorithm

The most prominent work done in the development of plane formulation of the contact of two cylinders is to develop an efficient contact algorithm. In the literature contact problem of solid bodies are worked extensively. Due to nature of the contact problem even for the small strain case and linear elastic materials it is nonlinear because of the potential for change in boundary conditions. Even for the simplest case boundaries of contacting bodies should be precisely monitored for a realistic contact simulation. In the literature there are studies arising from analytical considerations which will only apply for simple geometries and materials with simple constitutive equations in linear elastic regime. As a special case, in the analytical approach, one can find many studies for the contact of two elastic cylinders. Despite limiting factors, Hoffecker [30] applied a slightly modified one of these closed form solutions for his surface winding wound roll simulation.

Analytical models are useful for the verification of the developed algorithm for the special cases but they are limited and as the material models are becoming more complex and shapes of bodies are becoming irregular we should move to the realm of numerical techniques. In the realm of numerical techniques the finite element method is proven to be the most prominent numerical tool for contact studies [32]. In the finite element contact analysis there are mainly two approaches. The first is node to node contact and the second is boundary contact. In the first approach only node to node contact is possible and there may be overlap in the regions between nodes. The advantage of node to node contact is it is computationally effective and simple. The second approach searches any

potential overlap of the boundaries dictated by the actual elements. Hence it is more accurate but computationally much more burdening [32], [36]. For smooth boundaries the optimal choice will be first approach. The literature on this subject includes general formulations for a large class of materials and geometric conditions [40], [41]. Since the algorithm will form a basis for an industrial code we are searching a more efficient and simple yet sufficiently realistic way in an ad hoc manner. An example of this type is presented in the study completed by Ganapathi&Good [39]. They studied diametric compaction of a wound roll. They used the finite element method and adopted the general strategy of node to node contact. The main idea of their approach was to find the force which will bring down an associated node to the contacting rigid surface. In this state the node barely touches the surface and there is not any interaction. Only the gap length is made zero. Their contact implementation is accomplished via linear interpolation. It requires three solutions per contacting node. The first solution is done for applying a unit load at the interior mid point of core. The solution will give the associated pull down force of the node under consideration. A second solution is done for applying half unit load. This time a new pull down force is obtained. For the final solution the load is found by linear interpolation of the first two results such that it will produce zero pull down force (barely contact). After establishing contact conditions for a node the material properties are updated and same procedure is repeated for the next potential contact node. Finally operation is stopped when the total compression force is obtained. Here we will give an algorithm which requires only one solution per contacting node. For the sake of simplicity and also in order to compare with the experimental results of Ganapathi we first studied contact of a cylinder with a flat rigid wall. Figure 5.3 is showing a general

picture and also a detail of the contact region. In the finite element analysis we employed the general strategy of node to node contact. As mentioned earlier this type of approach especially works better and is more efficient for the cases in which order of contacting nodes are known a priori. Since this is the case for the rigid wall to cylinder contact problem element nodes at the outer surface of the cylinder are potential contact points. Also because of geometric symmetry and loading symmetry as the rigid block approaches the first contact node will be the tip (outermost) radial point. Furthermore as the block is pushed more, subsequent contact nodes will be in order which is directly dictated by the cylindrical shape. Due this nature of the problem we number the nodes at the surface of the cylinder in the order of their potential contact order. Hence the tip receives number 1 and the next to tip receives number 2 and so on. By this way corresponding positions on the rigid wall are also dictated. We denote the gap between a contact node on cylinder and its counterpart on rigid wall with δ. A subscript refers to the number of node. There will be no interaction between cylinder and rigid wall till the contact of the first node. Hence we can choose $\delta_1=0$ as the reference configuration and define other gaps with respect to this configuration. As the rigid wall compresses the size of the gaps will change so we use a superscript in order to define the state of a gap. So in the reference configuration the super script for all deltas is 1. As the second gap closes the super script will be 2 and so on.

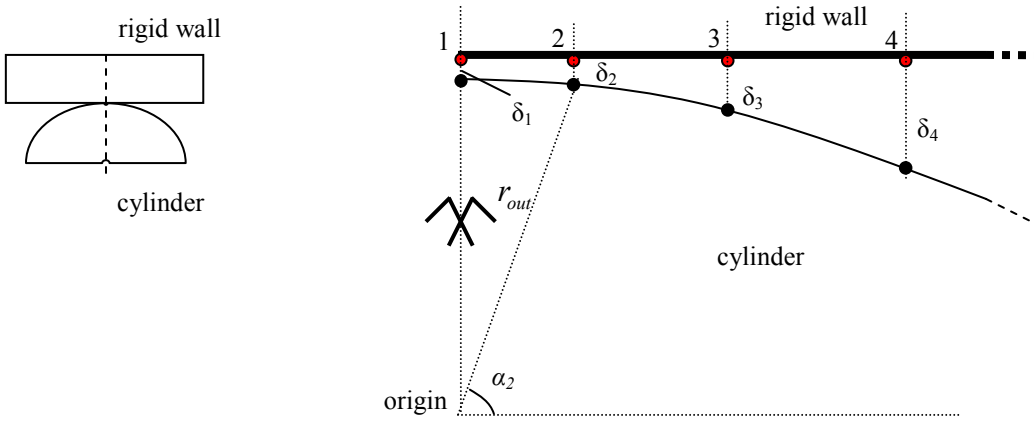

Figure 5.3 Geometry of the Node to Node Contact of a Rigid Wall and a Cylinder

From the geometry it is easy to show that for the reference configuration:

$$\delta_i^1 = r_{out}(1-\sin\alpha_i) \tag{5.20}$$

Here α_i is the angle between the ray of the $i^{th.}$ contact node and horizontal. α_i is directly related with the mesh refinement. It is easy to see that:

$$\alpha_i = \theta_{n_\theta+1-i} \tag{5.21}$$

Our solution procedure begins with running a wound roll model (Hakiel's 1D model) in order to obtain initial pressure hence initial radial modulus data for wound roll. This initial data is used in the calculation of stiffness matrix of the 2D plane model of wound roll prior to compaction. After this initial step we begin with the application of a vertical unit load at the tip i.e. node *1*.as seen in figure 5.4. We adopt the solution strategy of a quasilinearization concept. Thus we accept that material properties do not change unless a new node comes in contact with rigid surface. So during the deformation as the rigid surface moves from node *1* to node *2* the system is considered as linearly elastic. We

solve for this unit loading and obtain corresponding displacements of all nodes. Hence we know vertical displacements of node *1* and node *2* which we denote v_1 and v_2 respectively. Now we consider the required load for the rigid surface to come in contact with node *2* of cylinder. We denote this unknown load as F_1^*. This load when applied to the system will produce vertical displacements for node *1* and *2* such that they are geometrically compatible with the rigid surface. We denote these unknown displacements v_1^* and v_2^* for node *1* and *2* respectively.

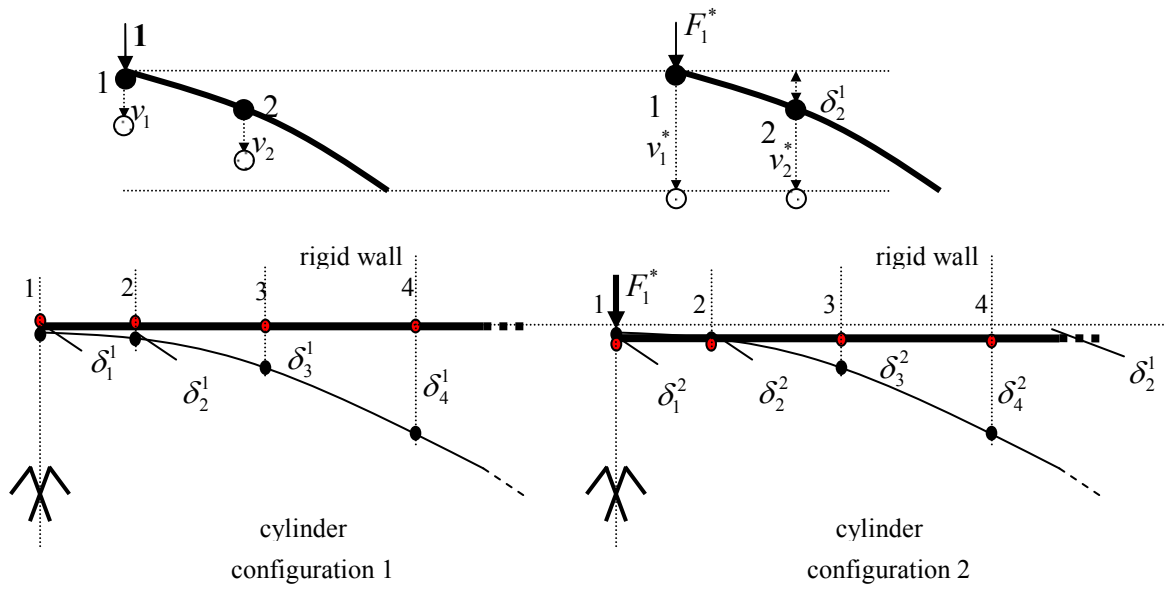

Figure 5.4 Geometry of Contact during Configuration 1 and Configuration 2

As seen easily from figure 5.4 the geometrical compatibility condition for the second unsolved case requires that:

$$v_1^* = v_2^* + \delta_2^1 \tag{5.22}$$

Also since we adopted quasilinearization, linear elasticity requires that there is

proportionality between forces and displacements i.e.

$$\frac{F_1^*}{1} = \frac{v_1^*}{v_1} = \frac{v_2^*}{v_2} \tag{5.23}$$

Substituting for v_1^* from compatibility relation we obtain

$$F_1^* = \frac{\delta_2^1}{v_1 - v_2} \tag{5.24}$$

$$v_1^* = \frac{v_1 \delta_2^1}{v_1 - v_2} \tag{5.25}$$

$$v_2^* = \frac{v_2 \delta_2^1}{v_1 - v_2} \tag{5.26}$$

Since we already know v_1, v_2 and δ_2^1 from the first solution we can now easily calculate v_1^*, v_2^* and F_1^*. The proportionality condition is valid for the whole structure so the doformation of a dof, q_i^* , which resulted from an F_1^* loading, can be easily calculated from the known counterpart q_i resulted from a unit loading:

$$q_i^* = \kappa \delta_2^1 \text{ Where } \kappa = \frac{\delta_2^1}{v_1 - v_2} \tag{5.27}$$

Here we denote κ as the proportionality constant. This procedure allows us to calculate the displacement field for the actual contact loading without actually solving for it. The actual contact state strain field can be calculated from these displacements per the usual finite element method. The stress field is calculated with the current state of the material properties. The total radial stresses are found by simply adding incremental stresses to the

current total stresses for every element. The total radial stress is used to update radial the modulus of elasticity of the associated element.

Now we should update the gap size for potential contact nodes. Actually this procedure is updating the geometrical boundary conditions of the contact zone. This first step, contacting to node *2*, is obtained by the movement of the rigid plate with an amount of v_1^*. This will be used to update gap sizes for potential contacting nodes:

$$\delta_i^2 = \delta_i^1 + v_i^* - v_1^* \text{ for } i = 1,2,...,n_c \tag{5.28}$$

Here superscript 2 indicates that associated value is calculated for contact state of node 2 and n_c is the maximum number of potential contact nodes which is set a predefined value. Total compression force and diametral compaction at the state 2 will be $2F_1^*$ and $2v_1^*$ respectively. The factor 2 arises because of the loading and geometrical symmetry. Now we can move on to the contact of node 3. This time since node 1 and node 2 are in contact with the rigid surface we should employ a multi point constraint (MPC) between their vertical displacements. We show the nodes subject to a vertical MPC by the red color in figure 5.5. The gap size δ_3^2 will be updatedusing the same basis this time as it was for δ_2^1 the first time.

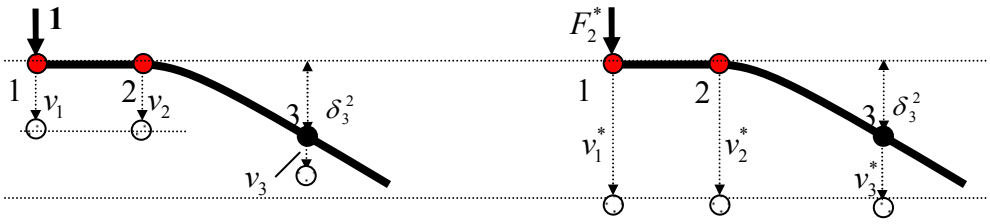

Figure 5.5 Geometry of Contact during Configuration 2 and Configuration 3

As in the previous calculation we apply a unit load to the updated system. The unit loading will cause displacements v_1, v_2, v_3 for the nodes 1,2,3 respectively. Again we denote the required unknown load for the contact of node 3 as F_1^*. We also denote corresponding displacements in this case as v_1^*, v_2^*, v_3^* for node 1,2,3 respectively. Since the vertical MPC constraints in both case vertical displacements for node 1 and 2 will be equal i.e. $v_1 = v_2$ and $v_1^* = v_2^*$. The geometrical compatibility requires that

$$v_1^* = v_3^* + \delta_3^2 \tag{5.29}$$

Again using the proportionality principle of linear elasticity we arrive at the following equalities:

$$\frac{F_1^*}{1} = \frac{v_1^*}{v_1} = \frac{v_3^*}{v_3} \tag{5.30}$$

The same procedure for calculating the displacement field for the actual situation will be applied again and the updating of material properties will be carried out as before. The geometrical update of the contact boundary will be done in the same way also:

$$F_1^* = \frac{\delta_3^2}{v_1 - v_3} \tag{5.31}$$

$$v_1^* = \frac{v_1 \delta_3^2}{v_1 - v_3} \tag{5.32}$$

$$v_3^* = \frac{v_3 \delta_3^2}{v_1 - v_3} \tag{5.33}$$

The same procedure for calculating displacement field for the actual situation will be applied again and the updating of material properties will be carried out as before. The geometrical update of the contact boundary will be done in the same way also:

$$\delta_i^3 = \delta_i^2 + v_i^* - v_1^* \tag{5.34}$$

Here the superscript 3 indicates the state is updated as the node 3 comes in contact. After contact of node 3 the total compression force and diametral compaction will increase with an amount of $2F_2^*$ and $2v_1^*$, respectively. The same solution procedure will apply to the other contact nodes until the total computed compression force exceeds the total predefined compression force. We can then give the generalized total compression force F_c^i and corresponding total diametral compaction v_c^i as the $i^{th.}$ node comes in contact with the rigid surface as:

$$F_c^i = F_c^{i-1} + 2F_1^* \tag{5.35}$$

$$v_c^i = v_c^{i-1} + 2v_1^* \tag{5.36}$$

Here $F_c^1 = 0$ and $v_c^1 = 0$ since there is no interaction at this state. The procedure will be

stopped when F_c^i is greater than predefined total compression force F_c^{TOT} for some *i*. This will complete the explanation of the approach. A flow chart is shown in figure 5.6 for the general contact algorithm:

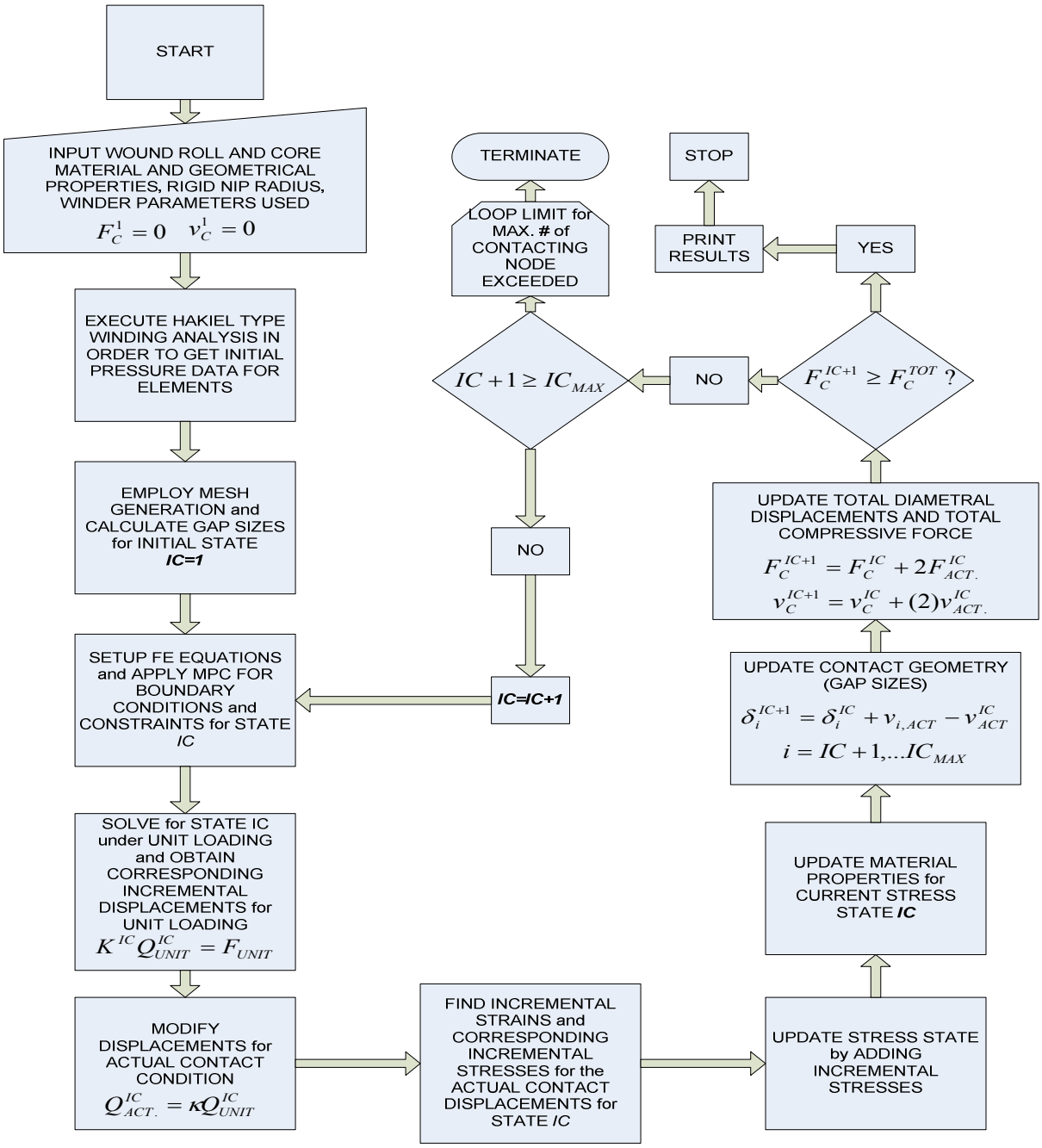

Figure 5.6 General Contact Algorithm

5.4 Contact of a Rigid Cylinder with Wound Roll

Now we are ready to derive an algorithm for the contact of two cylinders. One of the cylinders will represent the nip and the other the wound roll. We have already proposed a finite element formulation for wound roll with a nonlinear material feature. In application some nip cylinders are entirely formed by steel and some other include steel cores which are covered by rubberlike materials. In this study for the sake of simplicity nip cylinder will be taken as rigid. This assumption is quite valid in case of steel nip because most web materials are quite soft when compared to steel. Other cases can be studied with the same arguments explained here. In this case nip cylinder structure should be included in the analysis as another solid body. This means a system stiffness matrix for the nip must be produced and it must be coupled with wound roll stiffness matrix. The same quasilinearization technique can be used because the contact geometry is not radical and does not possess any sudden changes (i.e. the contact order will occur as dictated by the cylindrical shapes). We have also employed St. Venant principle here. Since the contact in this case occurs only at one side of wound roll and wound roll is directly supported from inside of the core, the other side will not have any stress and displacement field induced by nip contact. So as in the previous case we can only model a quarter of the wound roll. Our analysis for the wound roll and a rigid nip case starts with the geometrical resolution of contact region. In figure 5.7 we show the detail of the contact geometry. The main issue is to calculate gap sizes. The initial state is taken as the reference state and again the superscript shown indicates state for which node comes in contact. Thus the reference state will have a superscript 1 and $\delta_1^1 = 0$. It is easy to calculate gap size for the $i^{th.}$ node:

$$\delta_i^1 = r_{out}(1-\sin\alpha_i) + r_{nip}(1-\sin\gamma_i) \tag{5.37}$$

Here α_i is directly dictated by tangential refinement as before:

$$\alpha_i = \theta_{n_\theta+1-i} \tag{5.38}$$

γ_i can be found from the geometrical relation written via equivalency of horizontal lines which are colored red in the figure:

$$r_{out}\cos\alpha_i = r_{nip}\cos\gamma_i \tag{5.39}$$

This relation is easily converted to:

$$\gamma_i = \arccos\left(\frac{r_{out}\cos\alpha_i}{r_{nip}}\right) \tag{5.40}$$

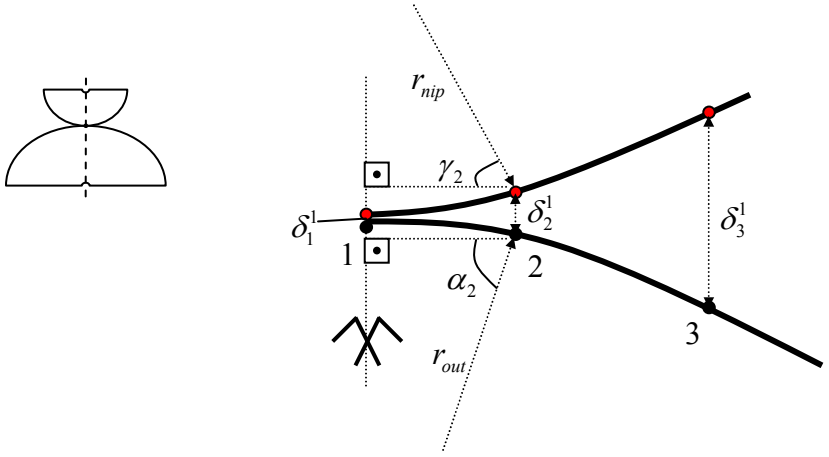

Figure 5.7 Geometry of Contact of Two Cylinders

Once the gap sizes, δ_i^1, are calculated the entire procedure will be quite similar to the rigid surface contact case. Only we substitute new gap sizes instead of their previous

counterparts. All update procedures will be same also. There is only a slight difference in the calculation of the compaction because now displacements are occurring only at one side:

$$F_c^i = F_c^{i-1} + 2F_1^* \tag{5.41}$$

$$v_c^i = v_c^{i-1} + v_1^* \tag{5.42}$$

5.5 Results and Conclusions

The algorithm in the figure 5.6 is coded in the background of VBA Excel. One of the important points in the calculations is the selection of a proper value for in-plane shear modulus ($G_{r\theta}$). In axisymmetrical formulations since in-plane shears are not considered and out of plane shears are generally small, selection of shear modulus (whether it is dependent on other material parameters as in isotropy or it is a completely independent parameter) do not affect overall results remarkably. In this situation in-plane shears are very important because of the plane formulation. The in-plane shear modulus ($G_{r\theta}$) is not given in the literature for web materials and moreover there is not any known test to measure this material property. However there are some closed forms in the literature which are proposed for the shear modulus ($G_{r\theta}$). These are similar to their isotropic counterpart (in fact isotropy is a special form of these equations) and they are represented as relations between other material parameters. As in Ganapathi [39] here we will give two common representations. Szilard derived (5.43) from St. Venant's work:

$$G_{r\theta}^{Szilard} = \frac{\sqrt{E_r E_\theta}}{2\left(1+\sqrt{\nu_{r\theta}\nu_{\theta r}}\right)} \tag{5.43}$$

Since product of Poisson ratios is small compared to unity (5.43) can be simplified as:

$$G_{r\theta}^{Szilard} \approx \frac{\sqrt{E_r E_\theta}}{2} \tag{5.44}$$

Cheng offered the following form:

$$G_{r\theta}^{Cheng} = \frac{E_r E_\theta}{E_r\left(1+\nu_{\theta r}\right)+E_\theta\left(1+\nu_{r\theta}\right)} \tag{5.45}$$

This can be also simplified if we take into account Poisson ratios are small compared to unity and also for most web materials $E_\theta >> E_r$:

$$G_{r\theta}^{Cheng} \approx E_r \tag{5.46}$$

In his work Ganapathi [39] conducted diametral compaction tests for wound rolls made from Newsprint and PET which were wound under different tensions. Comparison of results of Good&Ganapathi's algorithm with the experimental data indicated that two times of Cheng's expression results in superb agreement. Hence we used $G_{r\theta} = 2G_{r\theta}^{Cheng}$ in our calculations and obtained the same level of agreement. But the algorithm proposed here is much faster than Good&Ganapathi's because we are only solving for one time per contact node whereas Good&Ganapathi is solving three times per node. The web material data is provided in Table 5.1:

	PET	NEWSPRINT
K_1 (Psi)	1.05	0.0214
K_2	40.86	38.42
E_r (Psi)	711000	575000
E_θ (Psi)	711000	575000
Width (in)	6	6
Thickness (in)	0.002	0.00355

Table 5.1 Material and Geometrical Properties of Wound Rolls for Compaction Test

In the following figures verification of algorithm is clearly shown. However there are also some limitations. The current model treats roll as a monolithic solid body where as in reality it is consisted of web layers. Excessive compression with low hardness can result in separation of the layers. In this situation a more sophisticated model which takes into account this separation is needed. Finally we can conclude that for a generic web under normal winding operations the model would perform well.

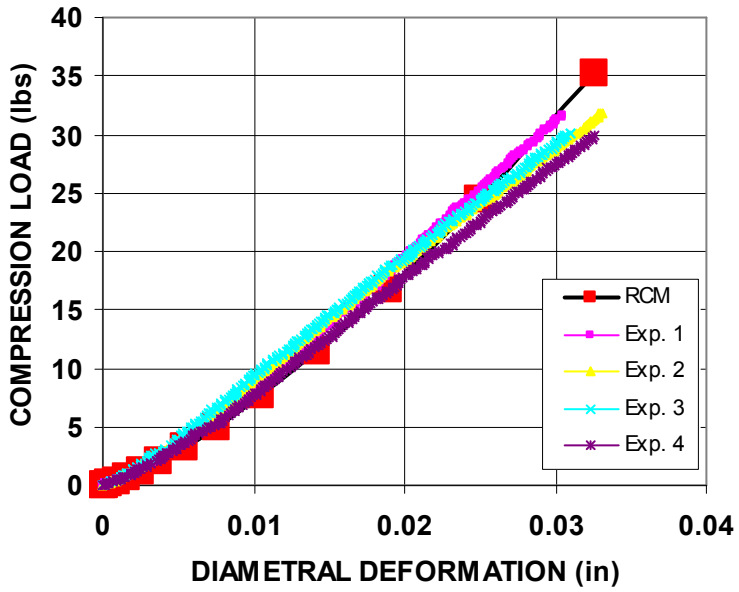

Figure 5.8 Load – Deformation Relation for PET – T_w=*333.3* Psi

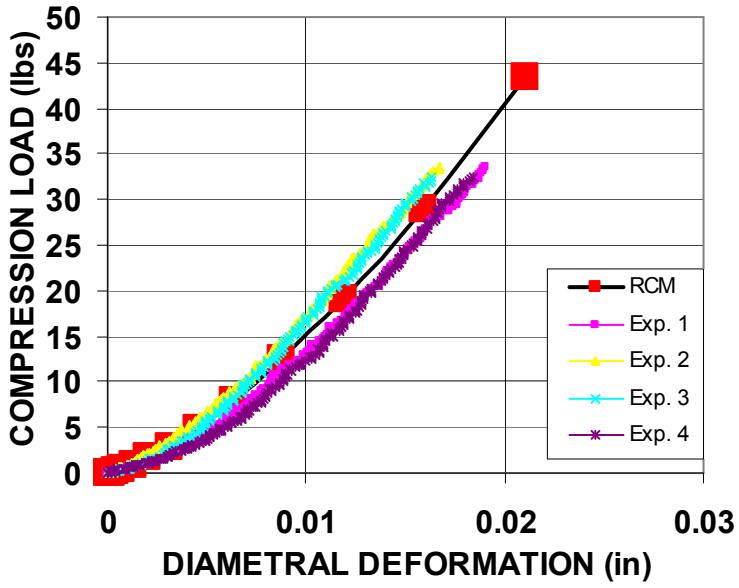

Figure 5.9 Load – Deformation Relation for PET – T_w=*666.7* Psi

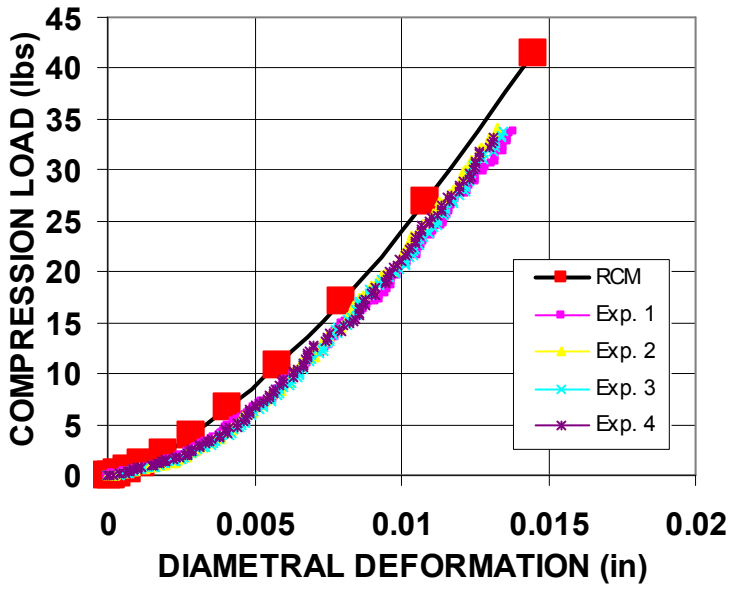

Figure 5.10 Load – Deformation Relation for PET – T_w=*1000* Psi

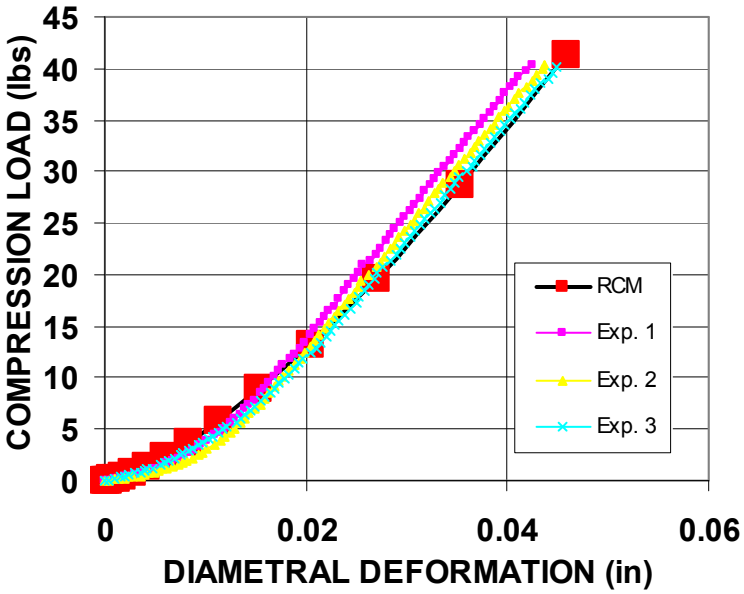

Figure 5.11 Load – Deformation Relation for Newsprint – T_w=*375* Psi

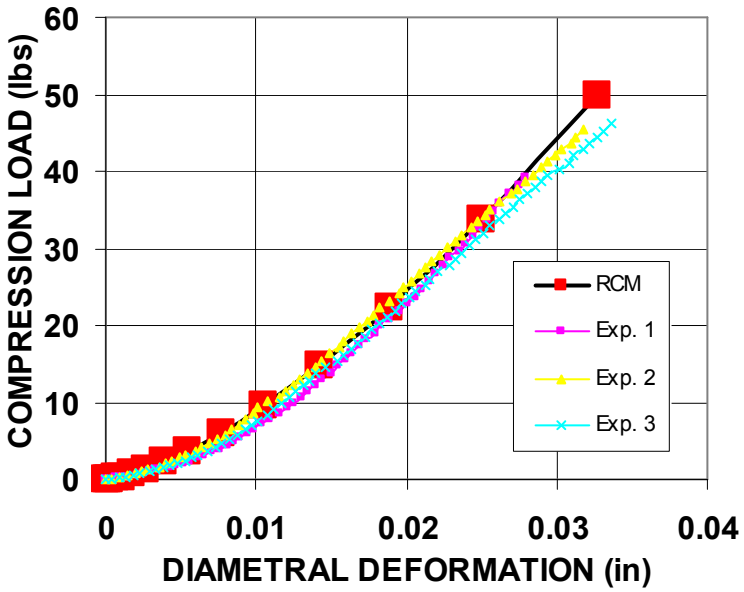

Figure 5.12 Load – Deformation Relation for Newsprint – T_w=*565* Psi

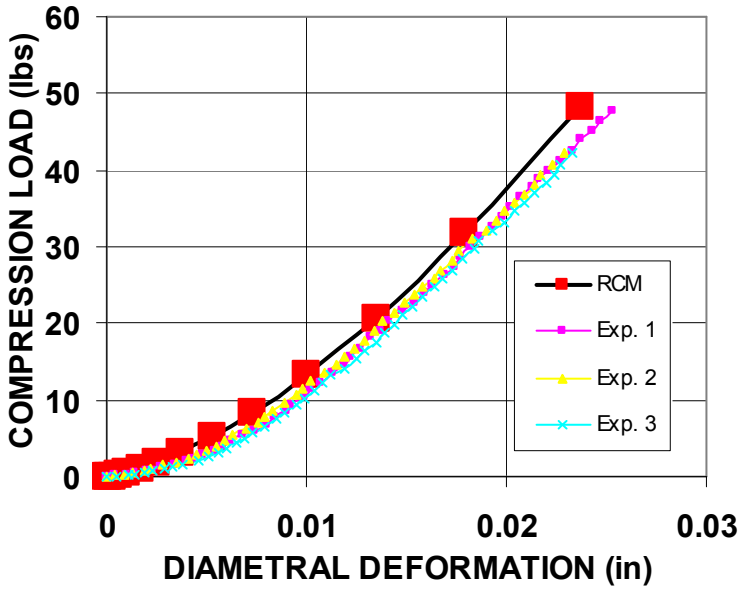

Figure 5.13 Load – Deformation Relation for Newsprint – T_w=*750* Psi

In case of a rigid nip we can demonstrate how nip radius affects the load – deformation

relation. The well known Hertzian theory of compression of cylinders gives the following relation (5.47) between load and deformation of compression between cylinders.

$$F = \frac{\pi}{4} E^* L \delta \tag{5.47}$$

Where L is the length of cylinders and E^* is the combined modulus for the cylinders which have E_1 and E_2 as modulus of elasticity:

$$E^* = \left(\frac{1-\nu^2}{E_1} + \frac{1-\nu^2}{E_2} \right)^{-1} \tag{5.48}$$

This is the form used in Hoffecker [30]. This relation does not include the effect of curvature of contacting bodies. We have run the code for several values of nip radius for newsprint data.

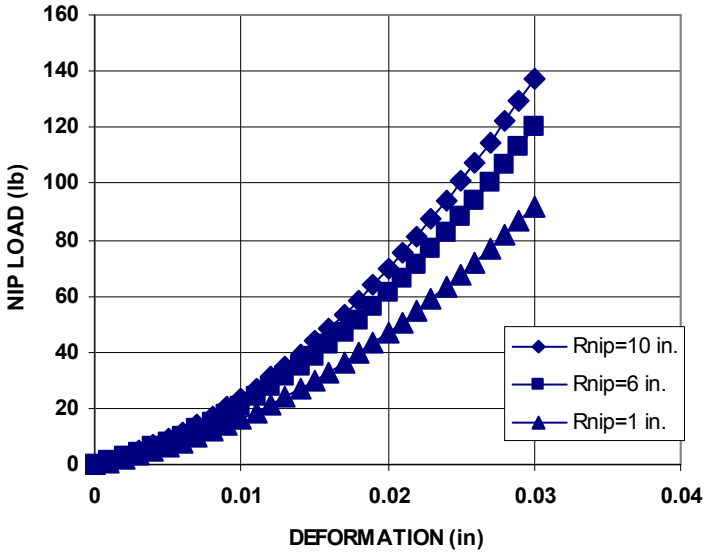

Figure 5.14 Effect of Nip Radius on the Load – Deformation Relation

As seen from figure 5.14 as the nip radius decreases, the slope of load deformation relation changes considerably. Since the indentation is easier, a remarkably softer representation in the radial stiffness is obtained on the same material with decreased nip radius. Hoffecker's [30] model does not include this kind of analysis.

6. BEAM SPRING MODEL

The connective model between axisymmetrical wound roll model and nip and roll compressor model is the beam spring model. In this model we represented the general contact problem of a nip and wound roll with beams and springs. In the figure we see beam model of a wound roll which corresponds the bending character of wound roll and springs which correspond to the radial stiffness of wound roll. In reality, since the nip is contacting to the wound roll only from one side winding under nip and wound roll contact is a 3D problem. Fortunately, taking into account some features, we can reduce the real 3D problem to a 2D counterpart without loosing nip effect. First of all the nip is contacting the wound roll continuously along its perimeter during winding. Also while winding a layer the axisymmetrical characteristic of the wound roll does not change significantly. This is because primary effect of the nip, nip-induced-tension, is dictated by the roll structure which is beneath. Since roll structure does not change during winding of a layer significantly we can assume that during winding a layer nip effect is same regardless of the tangential position. By this way without treating the whole wound roll as a solid, which will require enormous computational effort, we are simplifying in an ad hoc manner again. As explained before this approach is selected because of computational performance requirements of industrial codes.

6.1 Finite Element Formulation

We adopted the finite element method for the solution of the problem. The proposed model is depicted in figure 6.1.

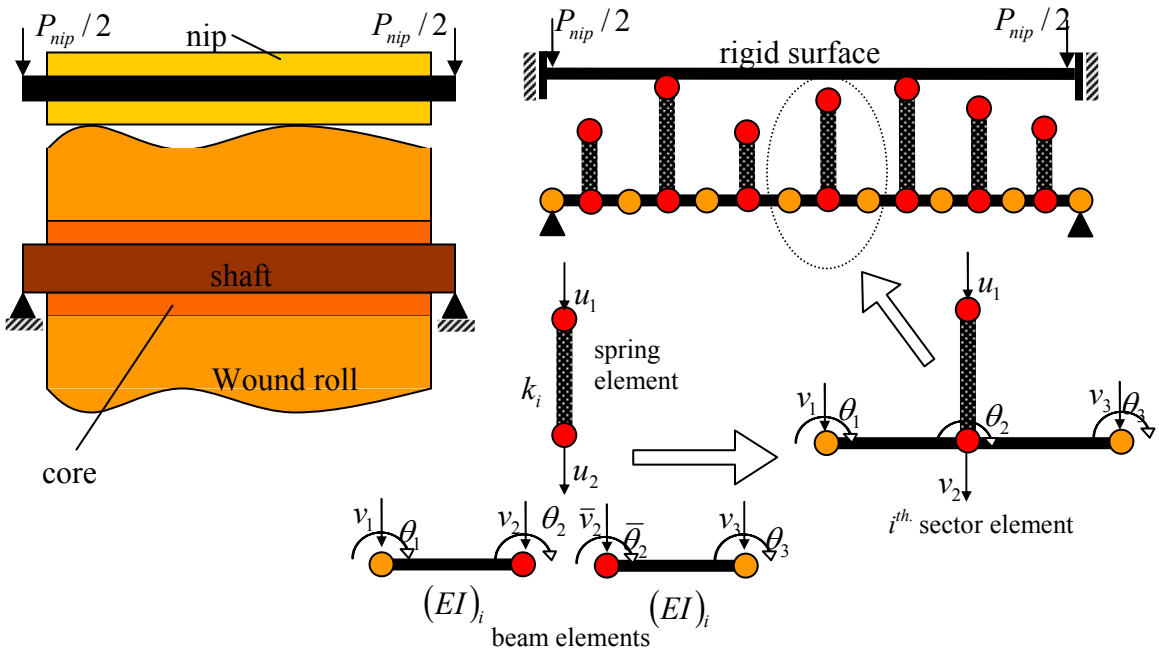

Figure 6.1 Beam – Spring Model Decomposition

The model has two key elements: beam elements and spring elements. We have selected 2 node regular Euler-Bernoulli beam elements to model the wound roll beam. The spring elements are also ordinary spring elements with 2 dof. The only difference is that the stiffness coefficient k is a state dependent variable (i.e. they are nonlinear springs). Two beam elements and one spring element are attached together as in figure 6.1 and form a "sector element". During assembly of the stiffness matrix these combination beam elements are connected as usual and the spring element is vertically coupled with the middle node of the associated formation of beam elements. The other ends of spring

elements are either under contact engagement with a rigid surface, representing nip, or free according to applied nip load P_{nip}. The combination is achieved with the following couplings:

$$v_2 = \bar{v}_2 = u_2 \tag{6.1}$$

$$\theta_2 = \bar{\theta}_2 \tag{6.2}$$

For cases where bending stiffness of the wound roll is comparable to that of the nip roller, the nip roller will be modelled as a beam in bending too. The finite element formulation of beams and springs are well known. We will start with the Euler Bernoulli beam formulation. Derivation of the Euler Bernoulli beam element can be found in elementary finite element books [34], [35]. Here we directly put the stiffness matrix of a beam element with length *L* and bending stiffness *EI*:

$$K^{beam} = \frac{EI}{L^3}\begin{bmatrix} 12 & 6L & -12 & 6L \\ & 4L^2 & -6L & 2L^2 \\ & sym. & 12 & -6L \\ & & & 4L^2 \end{bmatrix} \tag{6.3}$$

This stiffness matrix is used with the deformation vector of the element:

$$u^{beam} = \begin{bmatrix} v_1 & \theta_1 & v_2 & \theta_2 \end{bmatrix}^t \tag{6.4}$$

Force vector of the element is given as:

$$f^{beam} = \begin{bmatrix} f_1 & M_1 & f_2 & M_2 \end{bmatrix}^t \tag{6.5}$$

This stiffness matrix can be directly used for wound roll beam formulation once we put

correct values of *L* and *EI*. Length of beam element *L* should be selected as the half of the sector width:

$$L = w_s / 2 \tag{6.6}$$

The bending stiffness has two components. These are the modulus of elasticity along the neutral axis of the beam *(E)* and the moment of inertia of the cross section of the beam. The wound roll and core structure has different material properties and geometries. So we should calculate a combined bending stiffness. We assume that there is enough friction along CMD so at the wound roll and core interface there is no slip along CMD. Also we know that cross section of a sector is circular (i.e. both core and wound roll sections are annulus in shape and their origin is same). Thus we can assume that core and wound roll will bend together as a composite beam. This leads us to:

$$EI = E_z^{core} I^{core} + E_z^{w.roll} I^{w.roll} \tag{6.7}$$

Here E_z^{core}, $E_z^{w.roll}$ are the CMD modulus of elasticity of core and wound roll respectively and I^{core}, $I^{w.roll}$ are the moment of inertia of the core and wound roll respectively. The moment of inertia of the circular cross sections can be directly given as:

$$I = \frac{\pi(r_{out}^4 - r_{in}^4)}{4} \tag{6.8}$$

Here r_{out} and r_{in} are outer and inner radius of the annulus, respectively. Now with these inputs a beam element suitable for wound roll bending analysis can be formed. The spring element formulation is also straight forward. The spring stiffness matrix can be found in elementary finite element books [34], [35]:

$$K^{spring} = k\begin{bmatrix} 1 & -1 \\ -1 & 1 \end{bmatrix} \tag{6.9}$$

Again we should use a suitable spring stiffness factor in order to model radial stiffness of wound roll correctly. As we know in the axisymmetrical model we divided the wound roll along the CMD in to sectors. Each sector can have its own radial stiffness and geometrical characteristics. We have modeled each sector of wound roll as a spring element with a nonlinear force displacement relation. As we mentioned earlier, each sectors' nonlinear relationship comes from the nip and roll compressor model. The nip and roll compressor model produces points in the force-displacement plane. We can fit a second order polynomial approximation as for the $i^{th.}$ spring as:

$$P_i = c_i x^2 + d_i x \tag{6.10}$$

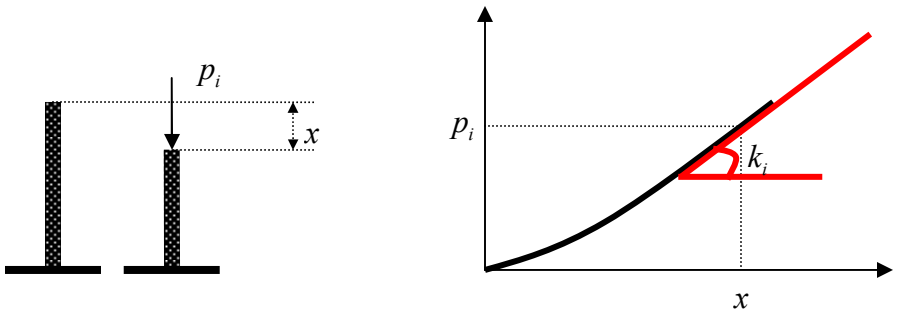

$i^{th.}$ spring under loading force deformation relation

Figure 6.2 Derivation of Spring Stiffness

Now spring stiffness can be easily computed directly by the definition: slope of the force displacement curve. Thus for the $i^{th.}$ spring this will be:

$$k_i = \frac{\partial P_i}{\partial x} = 2c_i x + d_i \tag{6.11}$$

This approach has been successfully implemented on several web materials, thus we believe expression (6.11) has sufficient complexity to model most web materials. As we mentioned earlier the combination of two identical beam elements and an associated spring element will form a sector element. The stiffness matrix for $i^{th.}$ sector element can be given as:

$$K^{sector} = \frac{(EI)_i}{w_s^3}\begin{bmatrix} k_i^* & 0 & 0 & -k_i^* & 0 & 0 & 0 \\ & 96 & 24w_s & -96 & 24w_s & 0 & 0 \\ & & 8w_s^2 & -24w_s & 4w_s^2 & 0 & 0 \\ & & & 192+k_i^* & 0 & -96 & 24w_s \\ & & & & 16w_s^2 & -24w_s & 4w_s^2 \\ & sym. & & & & 96 & -24w_s \\ & & & & & & 8w_s^2 \end{bmatrix} \tag{6.12}$$

Where

$$k_i^* = \frac{w_s^3 k_i}{(EI)_i} \tag{6.13}$$

The corresponding displacement vector can be given as:

$$u^{sector} = \begin{bmatrix} u_1 & v_1 & \theta_1 & v_2 & \theta_2 & v_3 & \theta_3 \end{bmatrix}^t \tag{6.14}$$

The sector elements are assembled as is usual in finite element analysis in order to obtain a global stiffness matrix of the system. The system is then solved under contact conditions. The solution is nonlinear both because of contact boundary conditions and nonlinear springs. Thus again we have to employ a specific contact algorithm solution.

6.2 Nip Contact Algorithm

The nonlinear nature of the problem requires a robust and efficient contact algorithm. Our goal here is to find spring forces for a given nip load. We will employ a similar ad hoc approach which we employed for the nip and roll compression problem. Thus we will adopt the quasilinearization principle again. This means that during deformations material properties (here spring stiffness) will remain unchanged unless the rigid beam comes in contact with a new spring tip(s). The height of the springs (i.e. springs' profile and the deformation of the wound roll beam) will determine the order of contact for the springs. This profile is directly taken from the roll profile (i.e. springs' profile is current roll profile). There will be no interaction between springs and rigid beam until the rigid beam contacts the longest spring or springs. This potential first contact position(s) can be easily determined by ordering the springs' heights. The number of springs is equal to the number of sectors. In figure 6.3 we depict 11 springs each with its own height and stiffness coefficients. We see from the figure number 5 and number 9 are equal in height and there is no longer spring than them. So we define the rigid beams reference configuration (i.e. state 1) as barely touching number 5 and number 9. Now we can define the gap sizes of springs for state 1:

$$\delta_i^1 = h_{\max} - h_i^1 \tag{6.15}$$

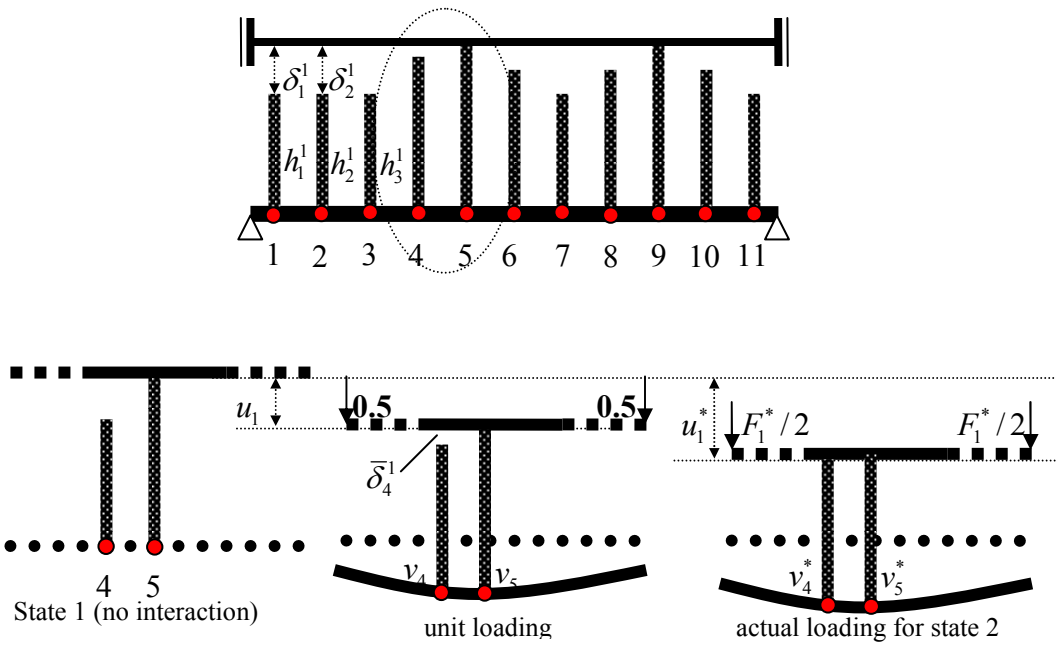

Figure 6.3 Contact Sequences of Nip Beam and Springs

Here again the superscript denotes the state of the variable. δ_i^1 is the gap size for the $i^{th.}$ spring in state 1. We assume that the nip (rigid) beam's ends are constrained such that vertical displacement of the nip beam is same at every CMD location. We start analysis by loading half of the unit load to the ends of nip beam. During this loading we will keep spring coefficients constant. This will produce a displacement field. In figure 6.3 we showed the vertical displacements for ends of springs where they are connected to the beam. There is a vertical displacement of the rigid beam and this is shown as u_1. Now using this displacement field we can calculate gap sizes for this unit loading:

$$\bar{\delta}_i^1 = \delta_i^1 + v_i - u_1 \tag{6.16}$$

We can find next possible contact node by finding minimum of $\bar{\delta}_i^1$. This is because we are assuming the system is linear elastic during this deformation. Now if we denote

$\min \bar{\delta}_i^1$ as $\bar{\delta}_j^1$ then we can use proportionality principle again. Let's denote the required force to make contact with the $j^{th.}$ spring as F_1^*. Let's also denote corresponding displacements as u_1^* and v_j^* for the rigid beam and the end of the $j^{th.}$ spring respectively. So the contact condition will be:

$$\delta_j^1 = v_j^* - u_1^* \tag{6.17}$$

Also proportionality principle can be used to state:

$$\frac{F_1^*}{1} = \frac{u_1^*}{u_1} = \frac{v_j^*}{v_j} \tag{6.18}$$

Using these expressions we get the required force and the unknown displacements (superscript with asterisk) as before:

$$F_1^* = \frac{\delta_j^1}{v_j - u_1} \tag{6.19}$$

$$u_1^* = \frac{u_1 \delta_j^1}{v_j - u_1} \tag{6.20}$$

And for any vertical displacement v_i^* using unit load counterparts v_i we can easily write:

$$v_i^* = \frac{v_i \delta_j^1}{v_j - u_1} \tag{6.21}$$

We have found the unknown load and corresponding displacements for the contact case. Now we have to update the contact geometry (gap sizes) and material properties (spring coefficients). The gap sizes are easily updated using:

$$\delta_i^2 = \delta_i^1 + v_i^* - u_1^* \tag{6.22}$$

The spring coefficients are updated only for the springs under contact during the deformations from state 1 to state 2. This is because only they are experiencing compaction. The amount of compaction can be obtained as:

$$x_l^1 = v_l^* - u_1^* \tag{6.23}$$

Here the superscript denotes the state in which compaction occurs. The subscript is the index for the nodes under contact during that associated state. Now we can easily update the spring coefficients for these springs:

$$k_l^2 = 2c_l x_l^1 + k_l^1 \tag{6.24}$$

Here the superscript denotes state and k_l^1 is for state 1. Since there is zero compaction for this state:

$$k_l^1 = d_l \tag{6.25}$$

Our final calculation is for spring forces. Since we know the compactions for these springs it is easy to write:

$${}^sF_l^2 = {}^sF_l^1 + k_l^1 x_l^1 \tag{6.25}$$

Here the left superscript (*s*) denotes that the force is for springs. The right superscript denotes the state. ${}^sF_l^1$ is zero because there is zero compaction for this state. We can generalize this procedure and continue till all springs are under contact. This is only possible if there is enough predefined nip load. If the nip load is big enough after

contacting all springs remaining load can be applied stepwise. At every step an update procedure for the spring coefficients has to be carried out. The total procedure for the general case is shown in the form of a flow chart in figure 6.4:

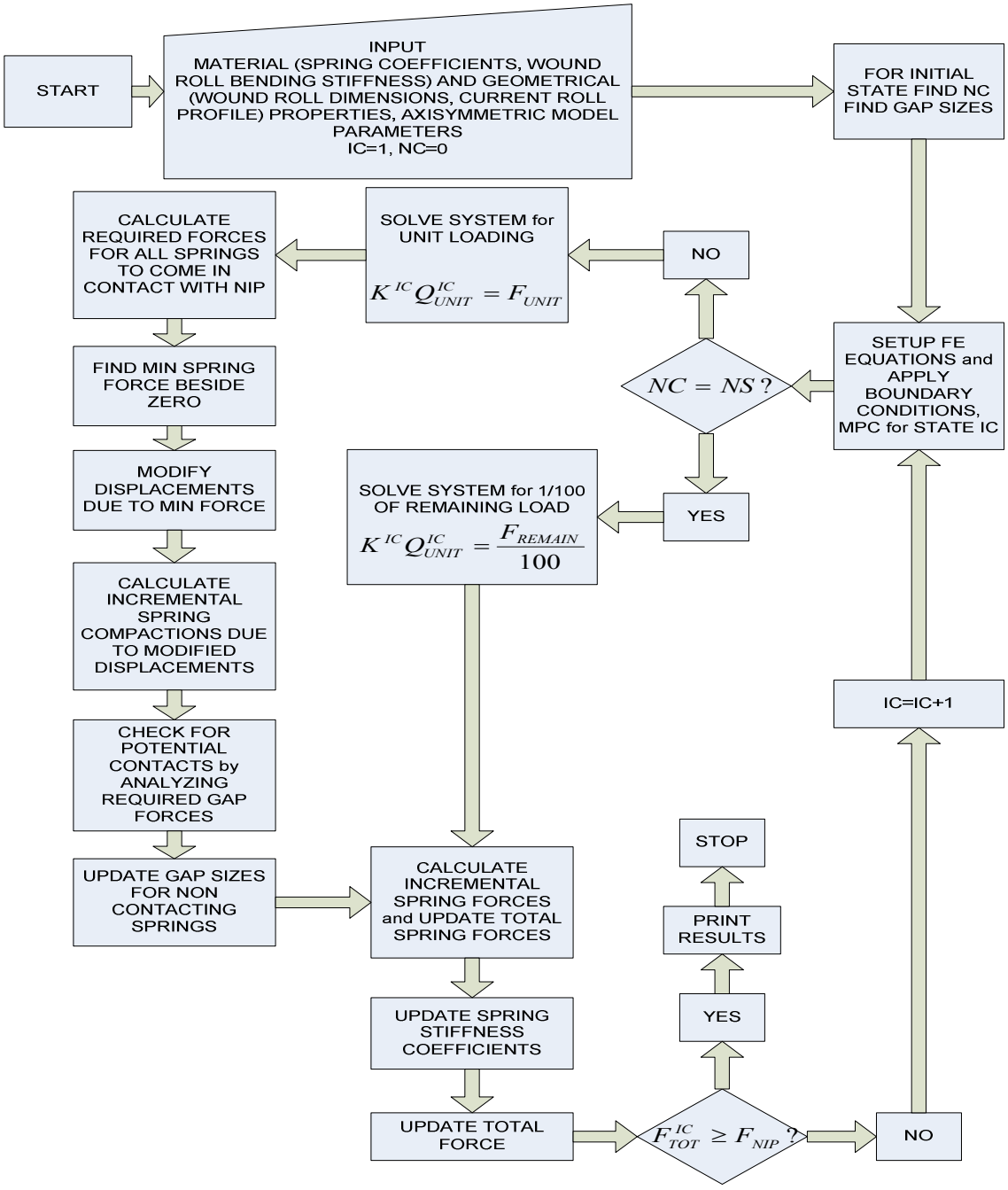

Figure 6.4 Beam Spring Model Algorithm

The given algorithm can be easily modified for the case of elastic nip. This time it is required to include the nip stiffness matrix as well. The wound roll beam matrix and nip stiffness matrix are in fact uncoupled. The link is the connecting springs. The procedure will be same only this time instead of computing only vertical displacement of the rigid nip beam we have to compute elastic nip beam's vertical displacements at different CMD positions which are corresponding to the tips of springs. Since the nip is considered an elastic beam in this case it should be constrained so that no additional modification is needed for orientation of nip beam. We have simply assumed that nip beam's ends are constrained so that there is not any rotation and also left and right ends are forced to move equal vertically by multi point constraints. These precautions will be enough to prevent any rigid body rotations of beam so that we will not worry about our contact algorithm which does not include such engagements. Actually for most of the nip engagements this consideration is valid because nip cylinders are forced with steel rods which are connected their shafts. These rods are rigid enough to prevent such rotations.

6.3 Results and Conclusions

In this section we will show some results regarding to the consistency of the developed algorithm. We choose a spring profile with as shown in figure 6.5. We used 10 sectors hence there are 10 springs. We run the code for a series of spring constants. At every turn we changed spring constants which characterize nonlinearity i.e. we set c_i to different values for every turn as in (6.25) and we set $d_i = 300$ for all runs.

$$c_i^j = 250(j-1) \text{ for } j=1,\ldots,5 \tag{6.25}$$

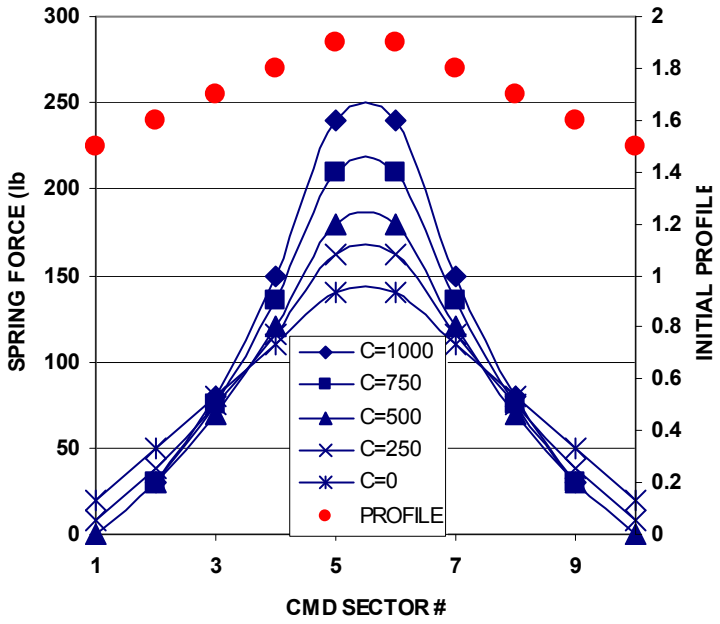

Figure 6.5 Effect of Nonlinearity on Spring Forces

In this analysis other related data is given in table 6.1:

Roll Width (in)	10
Roll Inner Radius (in)	2.5
Core Inner Radius (in)	0.5
E_{zweb} (Psi)	500000
E_{zcore} (Psi)	30000000
Nip Load (lb)	800

Table 6.1 Roll Beam Data

As seen from figure 6.5 it is obvious that spring force profile is dictated by the spring height profile which was expected. Also as the nonlinearity increases higher springs

receive greater loads because the same amount of compaction results in greater load as *c* of that spring increases.

7. COMBINED NIP and AXISYMMETRICAL WOUND ROLL MODEL

In this chapter we will combine the nip compression model, the axisymmetrical wound roll model, and the beam spring model.

7.1 Modeling the Nip Effect

As we mentioned earlier primary effect of nip is the nip induced tension NIT. Extensive studies were done in order to understand and model this effect. The most comprehensive recent study was completed by Kandadai [28] in WHRC of OSU. In his study he concluded that coulomb friction law is a very good approximation in the modeling of NIT. Based on this assumption, for a sector j if we know the average nip induced normal compression force N_j than resulting tangential stress (NIT_j) can be given as:

$$NIT_j = \mu_k \frac{N_j}{w_j h_{ave,j}} \tag{7.1}$$

Here w_j , $h_{ave,j}$ are width and average thickness of the $j^{th.}$ sector, respectively, and μ_k is the kinetic coefficient of friction between web and nip. As we introduced in previous chapters, the axisymmetrical wound roll model is capable of doing simulations when it is fed by the incoming web line tension. In fact the axisymmetrical wound roll model is

already allocating the incoming tension so that CMD positions can take different tangential stresses due to a CMD profile in outer lap radius. The key in the unification is to alter any CMD position's input tension by not only taking into account roll profile but also the calculated NIT for that CMD position. The NIT calculation will be conducted within the beam spring model. So in presence of a nip, the wound-on tension allocation is complicated by the NIT calculation and reallocation of wound on tension (WOT). General nip applications include surface winding, center winding with nip and gap winding. In his study [30] Hoffecker mentioned that in surface winding tension distribution is governed by local relative velocity fields occurring at the entrance of web into the roll. He neglected the complexities arising from the selection of winding technique and considered the center winding with nip case for two extreme conditions. Before addressing these conditions we should explain one of the most important parameter for calculations: wrap angle. The web generally enters the wound roll by first wrapping the nip roller. The angle between radii which correspond to this wrapping arc of web is called the wrap angle. Hoffecker assumed that roll profile can be dominant in the determination of final tangential stress or WOT for each sector due to the magnitude of the wrap angle. The two extreme wrap conditions are: Full wrapping and no wrapping. In figure 7.1 these extremes are depicted:

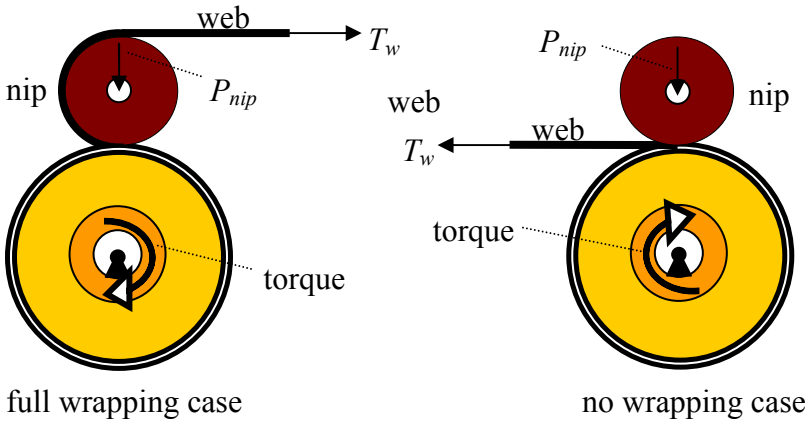

Figure 7.1 Wrapping Extremes for Center Winding w/ Nip

He argued that in case of full wrapping because of friction and unity of a web as a whole, the incoming web line tension tends to be uniform. For this case the consideration of tension allocation due to roll profile is no longer effective and we should set all sectors' tensions equal to incoming web line tension (T_w). So the final wound on tension for a sector j (WOT_j) will be the sum of incoming web tension and nip induced tension (NIT_j) if any for that sector:

$$WOT_j = T_w + NIT_j \tag{7.2}$$

For the no wrapping case, the final wound-on tension for a sector j will be sum of the allocated tension due to roll profile ($T_{w,j}$) and the nip induced tension (NIT_j) if any for that sector:

$$WOT_j = T_{w,j} + NIT_j \tag{7.3}$$

We have adopted this strategy and implemented these two extreme cases into the model. We have completed simulations for both cases and compared with the experimental

results. It is concluded that even for extreme wrapping angles roll profile is till dominant for tension allocation. So for all nip engagement cases we employed the tension allocation case.

7.2 The Combined Model

A general picture of how the combined model execuses is seen in figure 7.2:

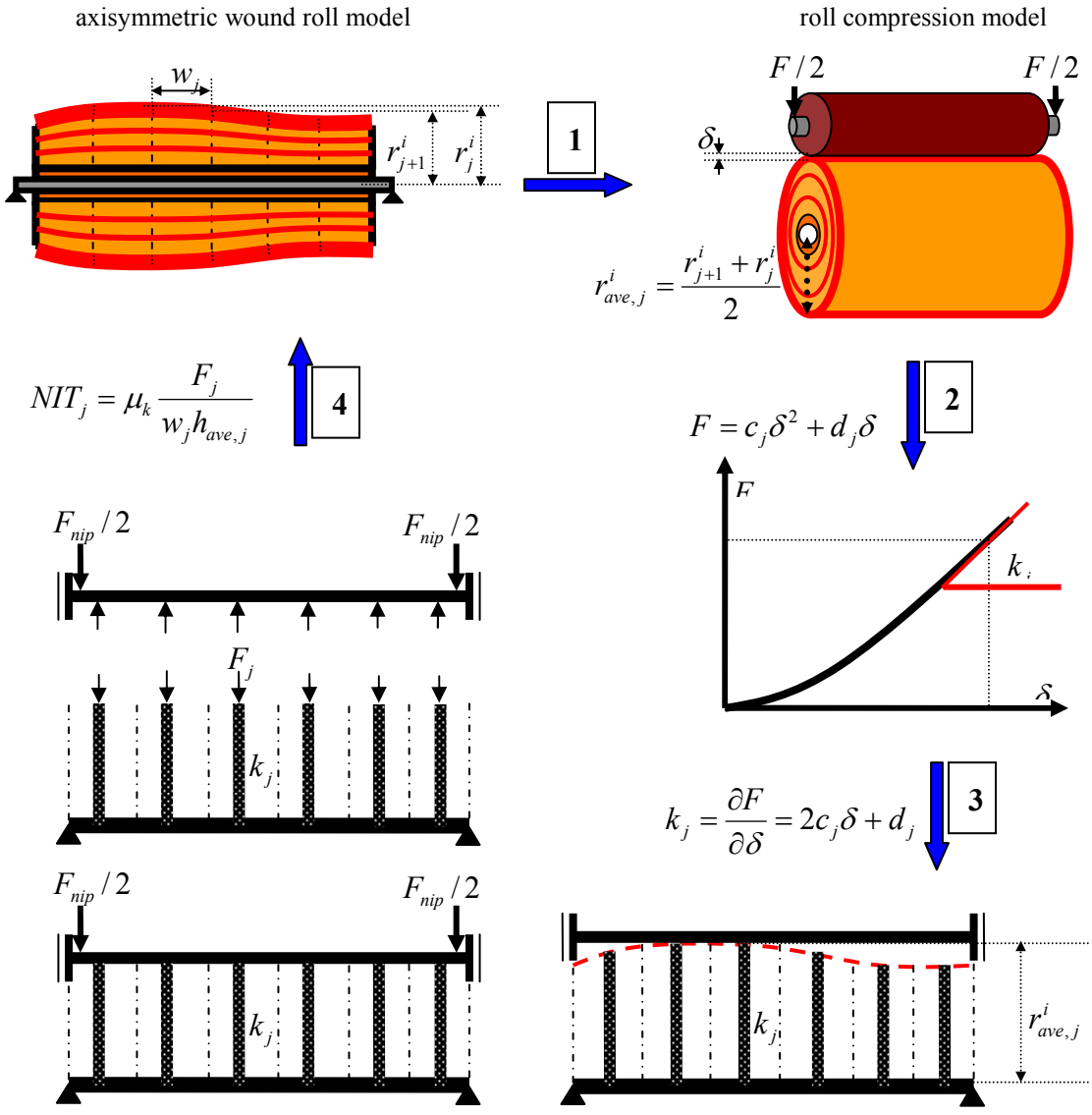

Figure 7.2 Combined Model Composition

After giving all inputs the combined model will begin to run just like the regular axisymmetric wound roll model (AWM) (allocating the incoming web line tension due to roll profile only) till the wound roll grows in radius to a trigger position (indicated by red layer). When a parameter (average roll radius, number of layers) hits the trigger value axisymmetric wound roll model stops and the roll compression model (RCM) begins execution. The axisymmetric wound roll model (AWM) provides the current roll radius profile, radial pressure profile and material properties to the roll compression model (RCM). The RCM breaks down the wound roll into sectors and begins to apply roll compression algorithm for each sector taking into account their different outer radius, pressure profile and material properties. The RCM produces data points in nip pressure versus displacement plane by repeating the analysis for each of the sectors. Then a curve fit module in the RCM produces second order curves for each data set of the sectors. These second order coefficients (c_j, d_j) for $j^{th.}$ sector are obtained by this way. These coefficients are, then, directly used to produce the spring stiffness of corresponding springs for sectors. The RCM pass these coefficients to the beam spring model (BSM). The beam spring model (BSM) also gets the roll radius profile from the AWM in order to use it as a spring height profile and in the calculation of the wound roll beam stiffness terms. Using the spring stiffness for all the springs and beam stiffness matrix for the wound roll and nip the BSM sets up the equations of the contact model of the nip and wound roll. The BSM obtains the final spring compression forces under given nip load. These spring forces are then sent to AWM in order to be converted to nip induced tensions and used in the calculation of the wound on tensions of the sectors. At this point the AWM resumes normal operation mode. The AWM uses these NITs in the calculation

of WOTs till the second trigger level. When this level is reached the whole sequence is repeated and a new set of NITs (derived from the current roll status) are obtained. The combined model continues working until the final roll radius is reached. The trigger value can be set as predicted radii or predicted intervals of layers. For example if the final roll radius is r_f and inner roll radius is r_{in} then we can call NIT calculation sequence s times simply by setting trigger radii as:

$$r_{trig,i} = r_{in} + i\frac{r_f - r_{in}}{s} \tag{7.4}$$

So whenever average roll radius is equal to a trigger value the NIT calculation sequence is initiated. Another way to initiate the trigger is using a predicted amount of layers for triggering NIT calculations. If there are n_w layers then trigger layers can be given as:

$$n_{trig,i} = i\frac{n_w}{s} \tag{7.5}$$

The flow chart of the combined model is shown in figure 7.3:

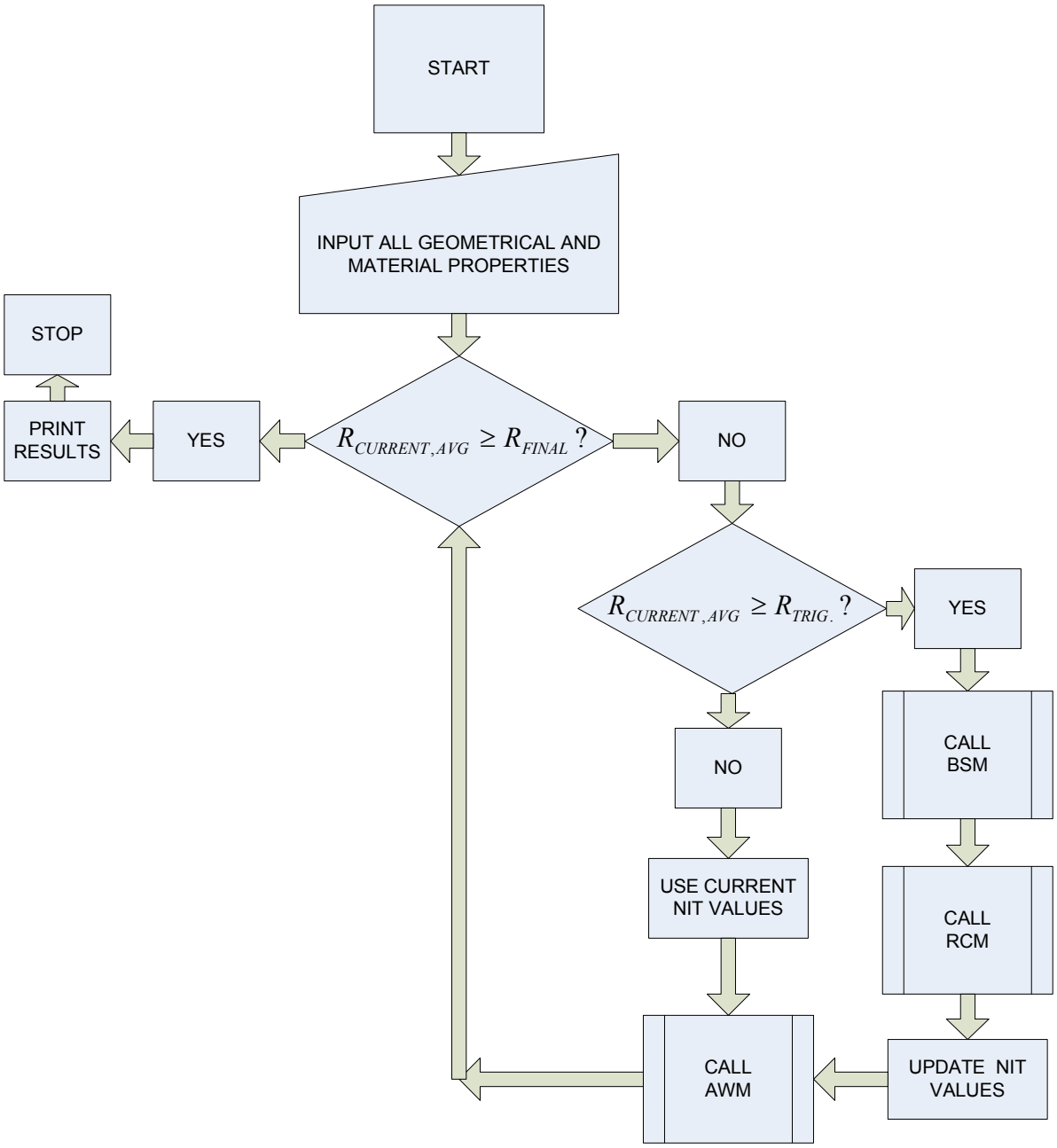

Figure 7.3 Combined Model Algorithm

8. EXPERIMENTAL VERIFICATION

In this chapter we will verify the proposed model via lab experiments. First we describe and give details of experimental work.

8.1 The Methodology

In order to verify our model we choose to construct a segmented instrumented core similar to that of Hakiel [17]. Our segmented core is formed by 24 individual identical rings each has a width of 1 inch. The rings are made from 7075 aluminum and have a diameter of 8 inches. Each ring is attached with 4 strain gages (2 dummy, 2 active). The active strain gages which are responsible for sensing the deformation are located at the most sensitive location of the rings. FE analysis revealed that this location is just near the joint place of inner bars and outer shell of ring. Active strain gages are attached to these points in order to measure circumferential strain. A picture of a segment and segmented core is seen in figure 8.1 and figure 8.2 respectively.

Figure 8.1 7075 Aluminum Segment with Strain Gage Attached

Figure 8.2 Segmented/Instrumented Core

Calibration is done with air pressure applied to the outer surface of the segmented core. For this purpose an external cover was molded from plastic and fit on the segmented core so that there is not any air leakage. Applied pressure is increased up to 100 Psi with 10 Psi steps. At every step strain readings are recorded and following calibration curves obtained. It is apparent that from the curves strain readings vs. pressures are linear with a factor around 5. This factor is less or more for individual rings and can be easily computed for each rings strain vs. pressure curve by linear fit. We have also measured the outer roll radius profile with a profilometer. We stop the winding and take readings across CMD at various pile heights.

8.2 The Material

The material that we used for the verification is 300 gage polyester provided by Mitsubishi Polyester. Mitsubishi intentionally produced a highly radical thickness profile so that experiments easily can pick up the effects of thickness variation. We are given four rolls each has width of 24 inches. These rolls were cut from a master roll which was 173 inches wide. These four rolls were cut with slitter knifes which are stationed at the downstream roller. During cutting Mitsubishi employed oscillation on the slitter knifes with amplitude of 3 inches and period of 220 seconds. The web's thickness profile is varying in both CMD and MD directions. In order to characterize thickness variation Mitsubishi recorded BETA-gage readings while the web is flowing on the rollers. The BETA-gage method infers thickness variation by measuring radiation that is transmitted through web. Given a constant source of radiation the amount which is transmitted through the web is directly related to the mass and hence the thickness of the web.

BETA-gage readings were produced with a sensing head going back and forth along CMD as the web passes through in a perpendicular MD direction. As seen from the figure 8.3 this produces thickness data along a zigzag pattern.

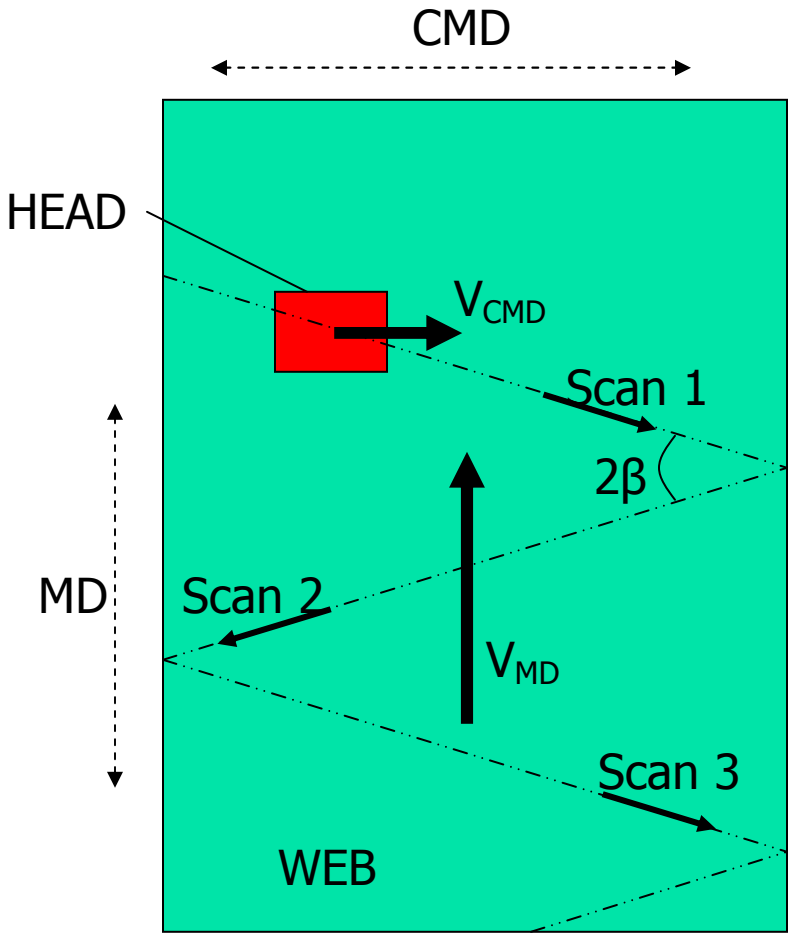

Figure 8.3 BETA-gage Zigzag Pattern

The zigzag pattern is characterized by the zigzag angle β. This angle is dictated by the speed of web (V_{MD}) on the line and the speed of the head (V_{CMD}) across the web. β can be easily calculated as:

$$\beta = \arctan\left(\frac{V_{MD}}{V_{CMD}}\right) \tag{8.1}$$

In our case the line speed is V_{MD} =64.4 in/s. and the head speed is =4.16 in/s. so numerical value for β is β = 86.3 degrees. This is a very important parameter as it dictates the average distance d_{ave} between two data points which are on the same CMD position and which belong to successive scans. From the figure 8.4 it is easy to see that

$$d_{ave} = w \tan \beta \tag{8.2}$$

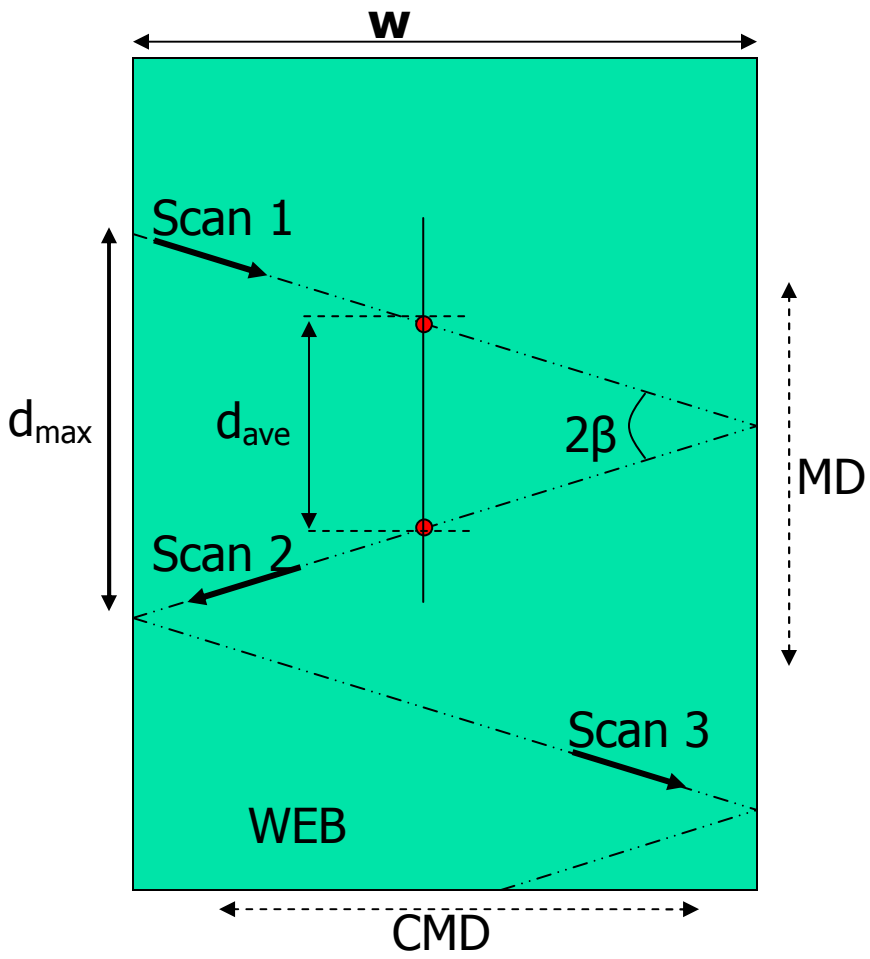

Figure 8.4 BETA-gage Distances

In our case d_{ave} is found to be d_{ave} = 2122 inches. It is easy to see that the maximum

distance between two consecutive data d_{max} points can be given as $d_{max} = 2d_{ave}$ from geometrical considerations. This makes $d_{max} = 4244$ inches.

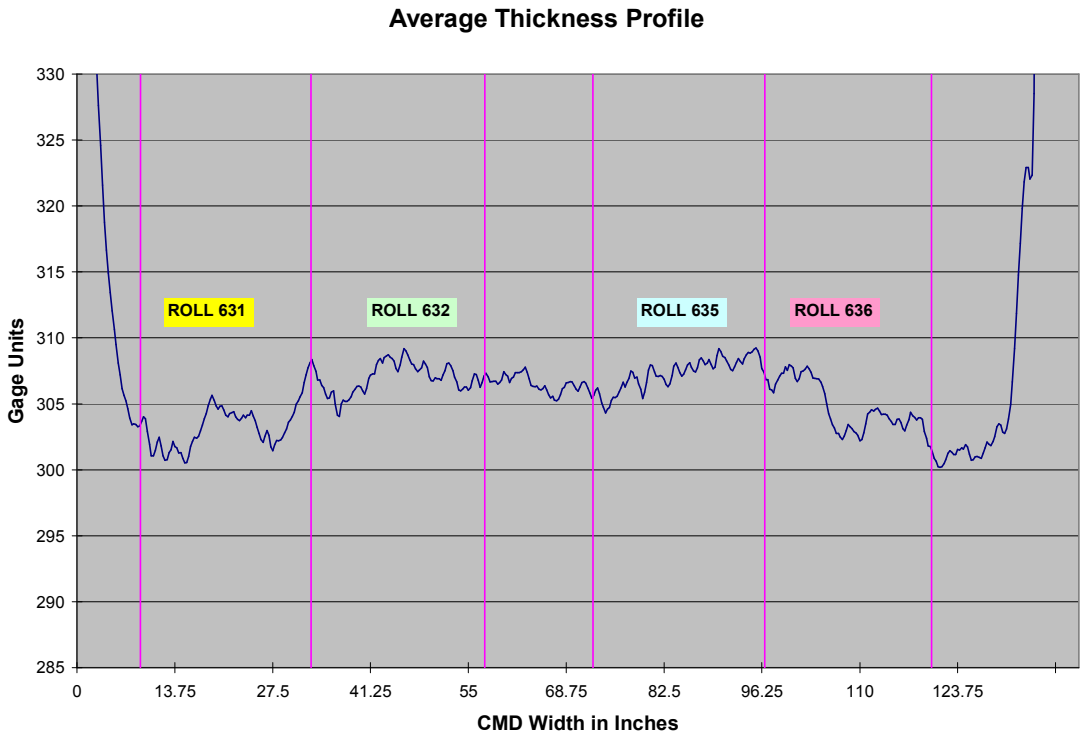

Figure 8.5 Master Roll Average Thickness Profile

In figure 8.5 we see the average thickness profile for the master roll. In this figure also the boundaries are marked for the small rolls. They are given code names 631,632,635 and 636. As you see during slitting some portions of the master roll were discarded.

The combined model requires the thickness profile for all the model layers. One model layer is formed by combining a certain number of actual layers for a given radial position. So in order to form model layers we have to find the corresponding thickness profile for a given radius. In fact we have to produce this profile from the given data on a zigzag pattern and also we have to take into account effect of oscillation. We begin by

defining the length of ith. lap:

$$L_i = 2\pi(r_c + (i-1/2)h_{ave}) \tag{8.3}$$

Where r_c is the core outer radius and h_{ave} is the average web thickness. Now we can define the distance between the head of the roll and the center of the ith layer D_i as

$$L_i = 2\pi(r_c + (i-1/2)h_{ave}) \tag{8.4}$$

$$D_i = \sum_{j=1}^{i} L_j - L_i/2 \tag{8.5}$$

If we explicitly calculate the summation we get:

$$D_i = 2\pi((i-1)r_c + (i-1)^2 h/2) \tag{8.6}$$

Now we can employ linear interpolation with the given data. In order to demonstrate the linear interpolation process virtually we draw the figure 8.6. As seen from the figure we are trying to calculate the thickness for the ith layer's jth CMD position. Without losing generality let the scans encompassing the ith layer be scan k and scan k+1 and their jth CMD positions' distances from the head be $d_{k,j}$ and $d_{k+1,j}$ respectively. If the BETA-gage thickness reading for scans k and k+1 are given as $h_{k,j}$ and $h_{k+1,j}$ at jth CMD position then the thickness for the jth CMD position of the Ith layer can be given by the linear interpolation:

$$h_{i,j} = h_{k,j} + \frac{h_{k+1,j} - h_{k,j}}{d_{k+1,j} - d_{k,j}}(D_i - d_{k,j}) \tag{8.7}$$

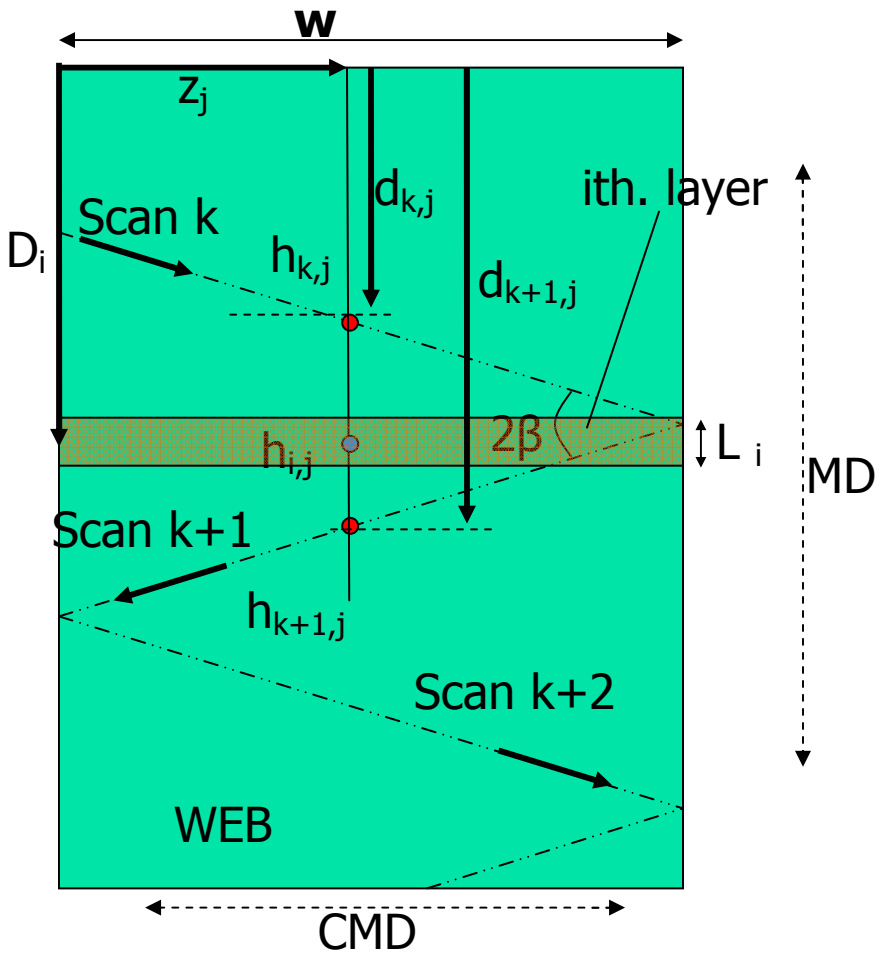

Figure 8.6 BETA-gage Data Harvesting

Once we produce the thickness profile for all layers i.e. producing the $h_{i,j}$ for all i,j then we can employ a procedure for taking into account the oscillation. Let the amplitude and the period of the oscillation be A_O and P_O respectively. If we assume a sinusoidal form then for the ith layer lateral shift caused by the oscillation can be given as:

$$\Delta_i = A_O Sin\left(\frac{2\pi D_i}{\lambda}\right) \tag{8.8}$$

Here λ is the wave length and can be given as the product of period and the web line speed V_{MD}

$$\lambda = V_{MD} P_O \tag{8.9}$$

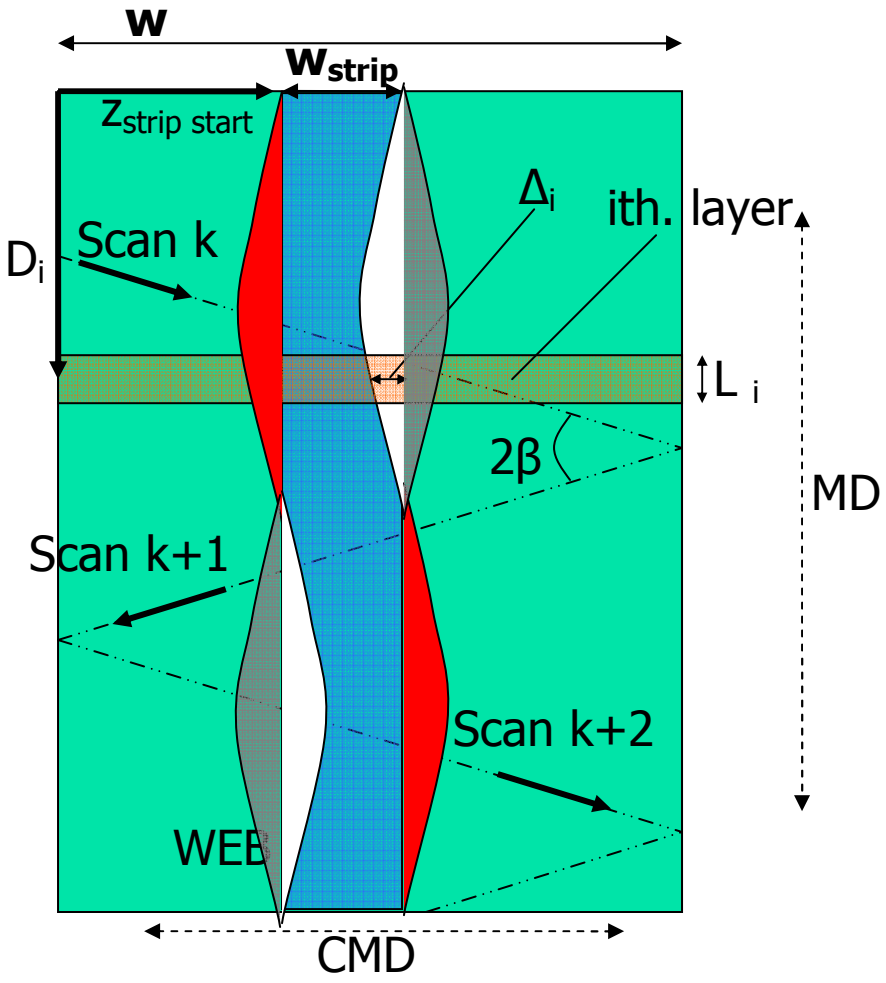

Figure 8.7 BETA-gage Oscillation

As seen from the figure 8.7 if one of the small rolls, represented with the blue strip, is cut with the given oscillation then the white area of the strip will have the thickness values of the adjacent grey area. We have developed and implemented an algorithm which takes the associated thickness data for given strip (small roll) position (z_{strip}, w_{strip}) in CMD and oscillation parameters. Now we have the thickness profile for a given small roll which is cut from the master roll with the oscillation. Even for this small roll there are too many data points across CMD. For example for the master roll the HEAD recorded about 500 data points across CMD. So for 24 inch small roll which is cut from the master roll there are about 88 data points along CMD. In the combined model we are defining sectors along CMD and defining the thickness profile at the sector connections. Since the number of sectors is directly affecting the number of dof of the problem using all CMD data will greatly increase the number of dof hence the CPU time of solution. In order to get a reasonable CPU time we will simply extract the thickness data for suitable number of sectors which happens to be quite smaller than the actual number 88.

ith. layer BETA-gage thicknees profile

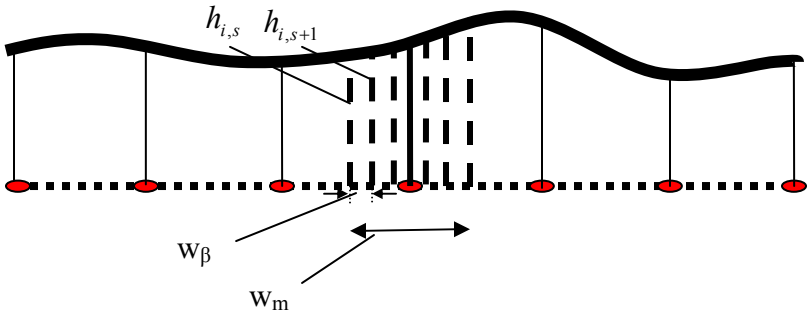

ith. layer model thicknees profile

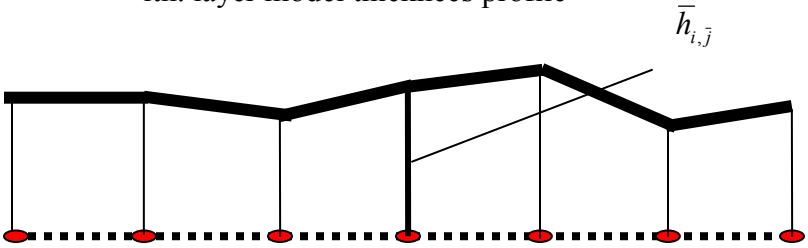

Figure 8.8 CMD Thickness Interpolation

As seen from figure 8.8 we are taking an average of the BETA-gage thickness for a model sector. If the BETA-gage based thickness data and the CMD data width for BETA-gage are given by $h_{i,s}$, $h_{i,s+1}$,… and w_β respectively then we can calculate the area A_β under the BETA-gage data. An average thickness $\bar{h}_{i,\bar{j}}$ based on equivalent area can be obtained by simply dividing this area to the model sector width w_m.

$$A_\beta = \sum_s \left(\frac{h_{i,s} + h_{i,s+1}}{2} \right) w_\beta \tag{8.10}$$

$$\bar{h}_{i,\bar{j}} = A_\beta / w_m \tag{8.11}$$

The reason we went on calculating the model thickness from area is mainly based on the desire to get a better representation of the thickness profile. If we have used basic linear interpolation depending on the position only we would only retain two adjacent BETA-gage data points for the computation of model thickness for a sector whereas there are more BETA-gage data in one sector. So we are taking other BETA-gage data into consideration by using the area method.

The combined model also needs the material constitutive parameters as inputs. These are Pfeiffer's K_1 and K_2 parameters which characterize the material nonlinearity in radial direction and tangential modulus of elasticity E_θ. In order to obtain Pfeiffer's constant we conducted compression tests on 1 inch thick stacks of the web material with an Instron machine. The Instron machine's own deformation measurement system resulted in an unusually soft behavior for the material (low $K_2 = 92$) when compared with its apparent hardness during handling. We thought that under high loads machine's frame distortions can contribute to the results so we went on to measure the displacement of specimen directly by an external method. We have used a strain extensometer for this purpose. This device is externally attached to the specimen so it is impossible to be affected by machine's own deformation under the load. This method turns out to be consistent and we have obtained a high K_2 value (= 450) for the stack which corresponds well with the material's apparent hardness. In figure 8.9 we can see the difference between Instron's own measurement system and the externally attached strain extensometer.

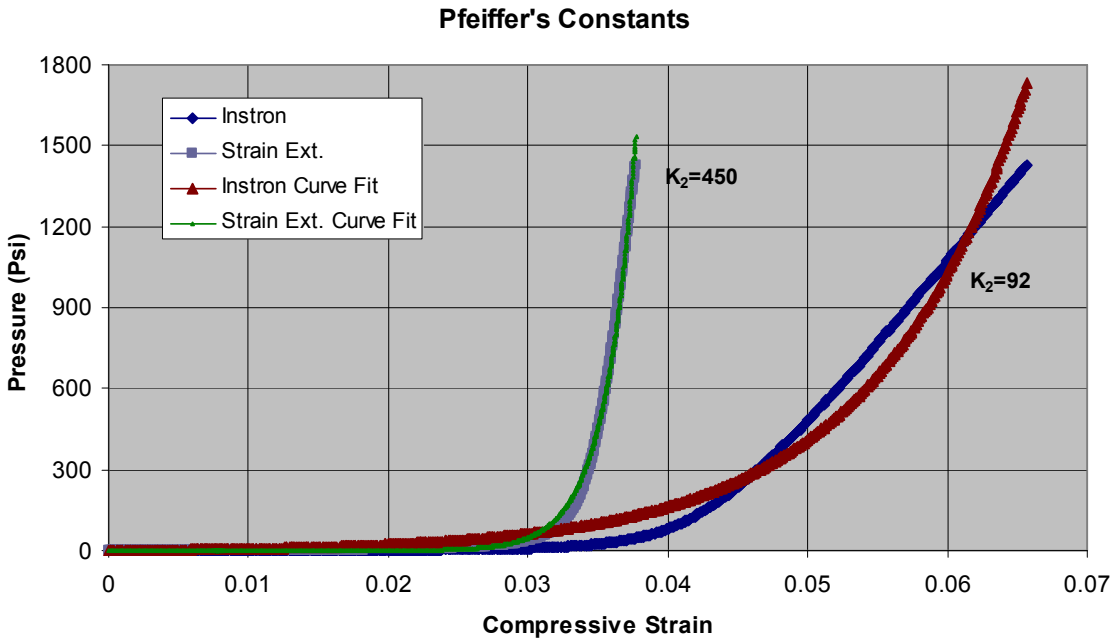

Figure 8.9 Pfeiffer's Constants

We have employed a standard tensile test for the characterization of the tangential modulus. We lay down a sample of web material which is 50 feet long and applied tension on it. The elongations were recorded for various load levels and a stress strain curve was obtained from this data. The test is repeated three times, figure 8.10, and a linear curve was fitted over the average values, figure 8.11. The slope of this curve is simply equal to the tangential modulus of elasticity. The tangential modulus of elasticity is found to be 731,000 Psi.

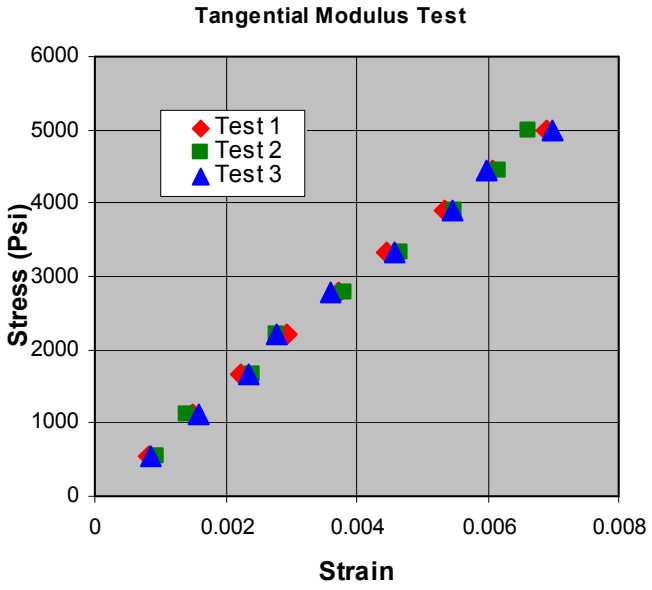

Figure 8.10 Stretch Tests

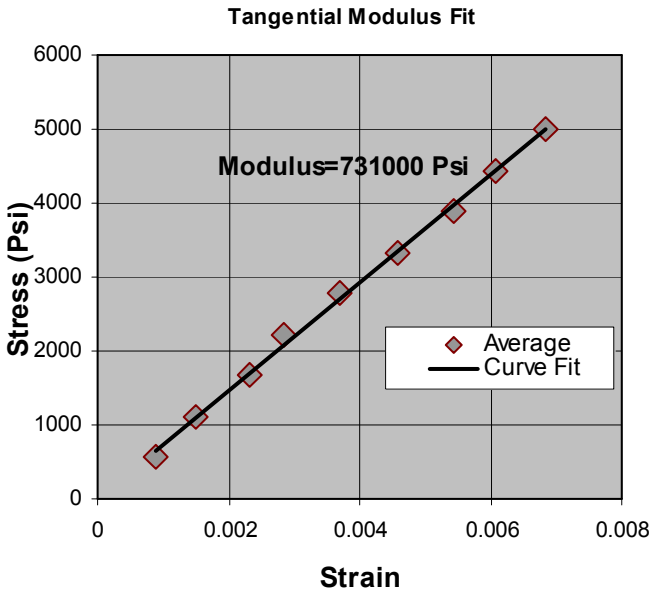

Figure 8.11 Tangential Modulus of Elasticity

8.3 Experimental Results

We have experiments in two categories. The first category includes the center winding only cases. The second category includes the center winding with a nip roller cases. The material and geometric properties and winder conditions are same for all rolls. Here we give Table 8.1 for these data:

Roll Inner Radius (in)	4	E_θ (Psi)	731000
Roll Outer Radius (in)	11.75	E_Z (Psi)	731000
Core Inner radius (in)	3.7	v_{rz} , v_{rt}	0.01
Core Material Mod. (Psi)	10400000	$v_{\theta t}$	0.1
Core Poisson Ratio	0.33	T_w w/ Nip	1.5 PLI
Roll Width (in)	24	T_w w/o Nip	1.2 PLI
K_1 (Psi)	0	Nip Load	1.33 PLI
K_2	450	Ave. Thickness (gage)	300

Table 8.1 Material and Geometrical Properties of Wound Rolls Used in Tests

We ran center winding only tests with all four rolls at 1.5 PLI of winding tension. Here we give the core pressures from the model and tests. The test values are average of the values of two consecutive experiments under same conditions. The core pressures are given for four different pile heights. The pile height is the thickness of the web material which has been wound onto the core.

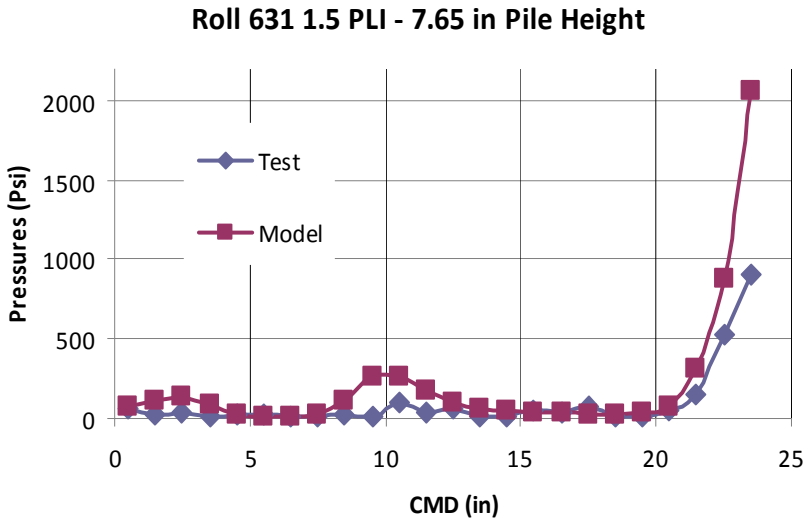

Figure 8.12 Roll 631 1.5 PLI 7.65 in. P.H. Pressures

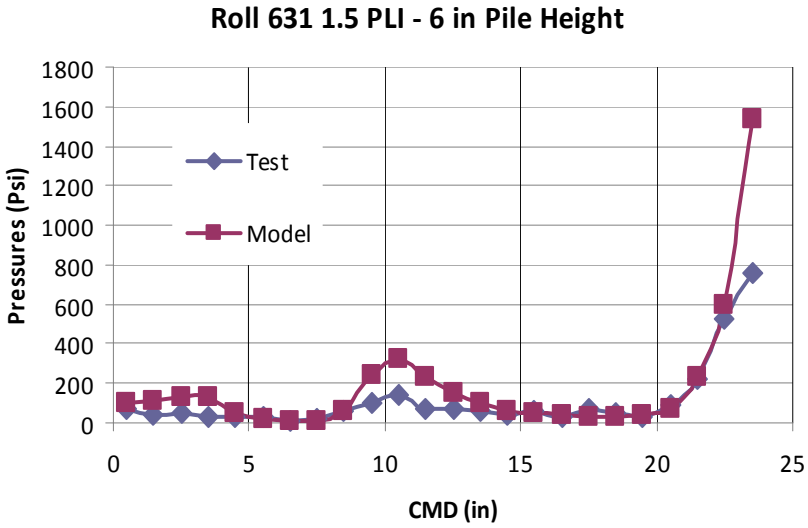

Figure 8.13 Roll 631 1.5 PLI 6 in. P.H. Pressures

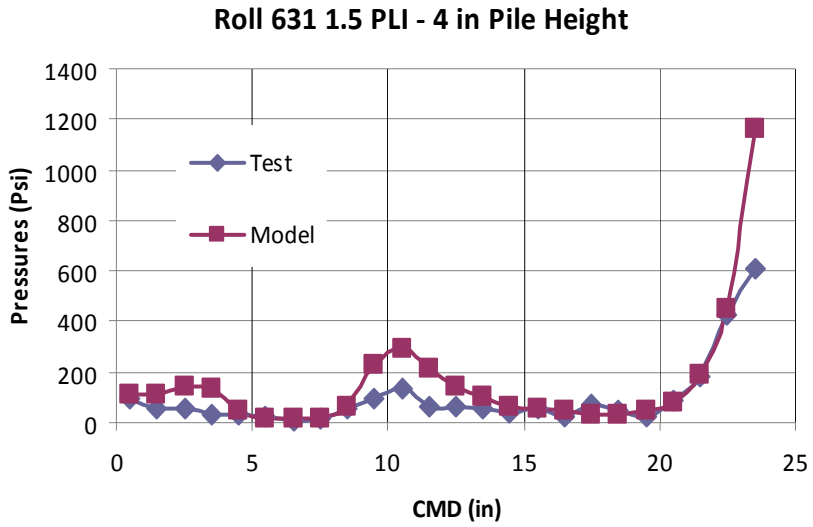

Figure 8.14 Roll 631 1.5 PLI 4 in. P.H. Pressures

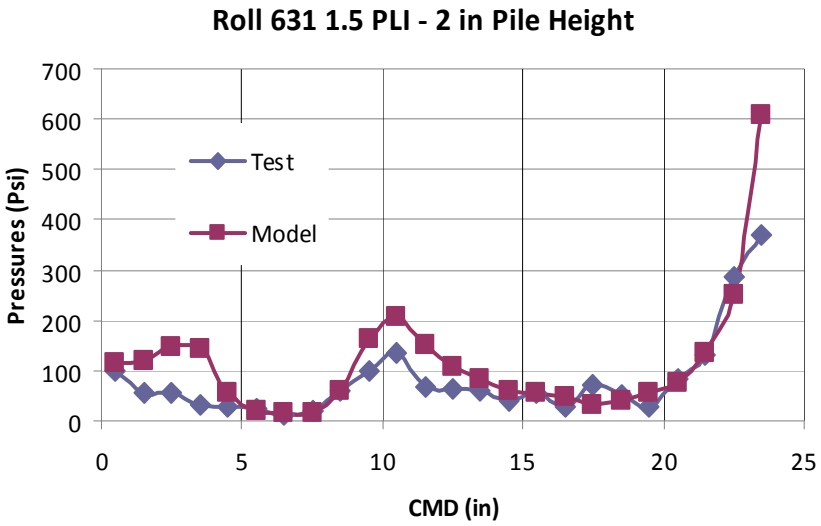

Figure 8.15 Roll 631 1.5 PLI 2 in. P.H. Pressures

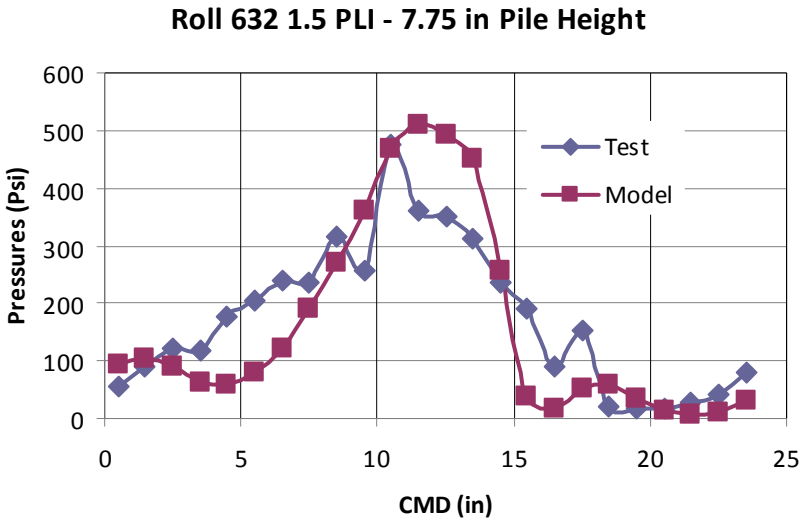

Figure 8.16 Roll 632 1.5 PLI 7.75 in. P.H. Pressures

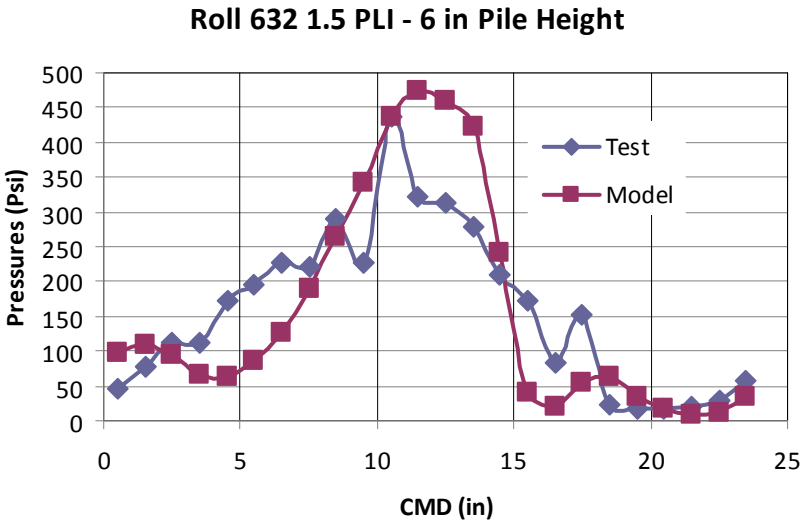

Figure 8.17 Roll 632 1.5 PLI 6 in. P.H. Pressures

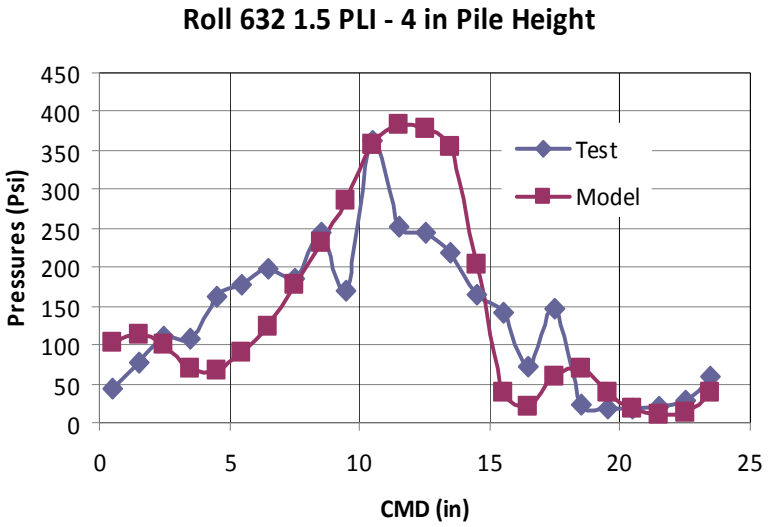

Figure 8.18 Roll 632 1.5 PLI 4 in. P.H. Pressures

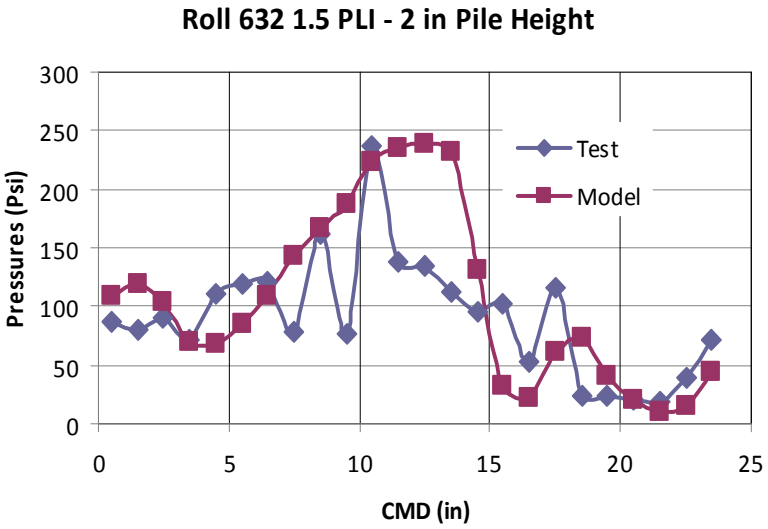

Figure 8.19 Roll 632 1.5 PLI 2 in. P.H. Pressures

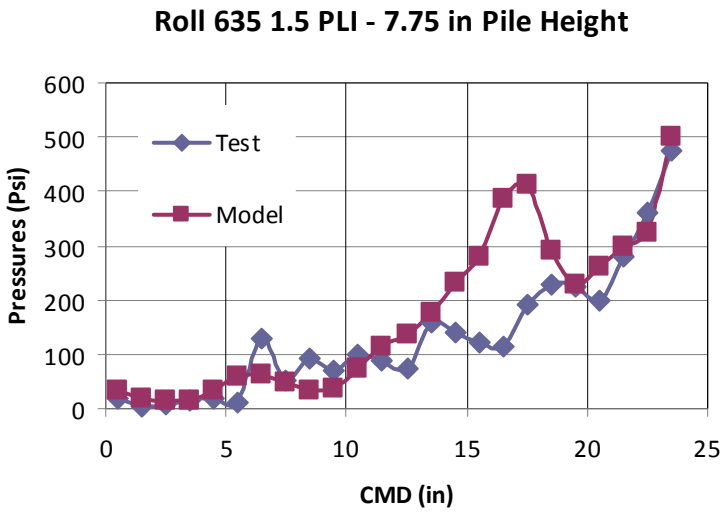

Figure 8.20 Roll 635 1.5 PLI 7.75 in. P.H. Pressures

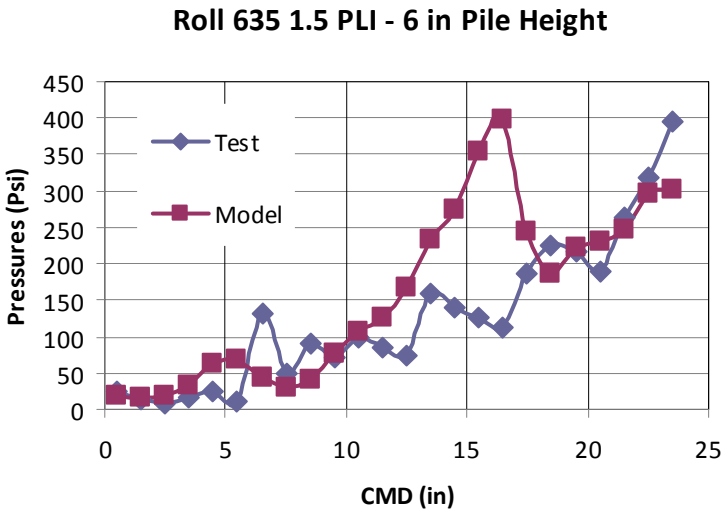

Figure 8.21 Roll 635 1.5 PLI 6 in. P.H. Pressures

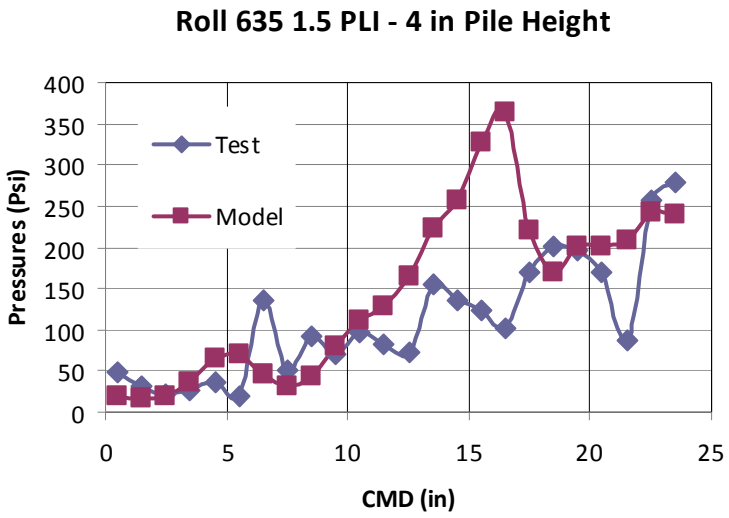

Figure 8.22 Roll 635 1.5 PLI 4 in. P.H. Pressures

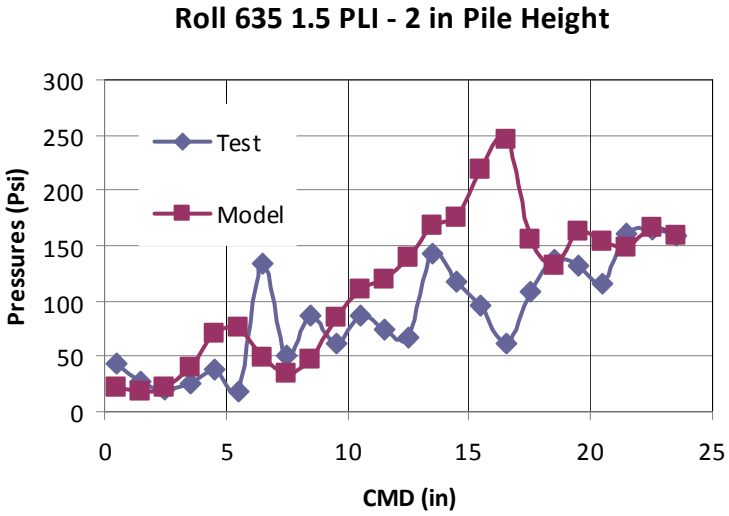

Figure 8.23 Roll 635 1.5 PLI 2 in. P.H. Pressures

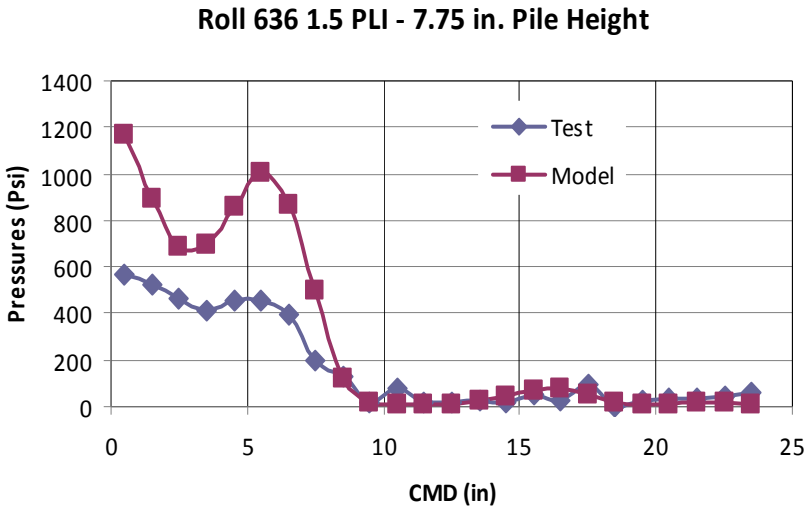

Figure 8.24 Roll 636 1.5 PLI 7.75 in. P.H. Pressures

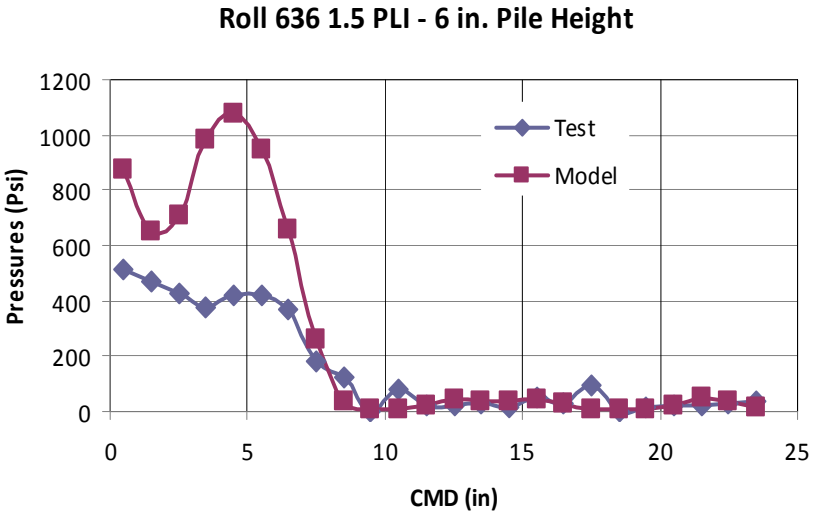

Figure 8.25 Roll 636 1.5 PLI 6 in. P.H. Pressures

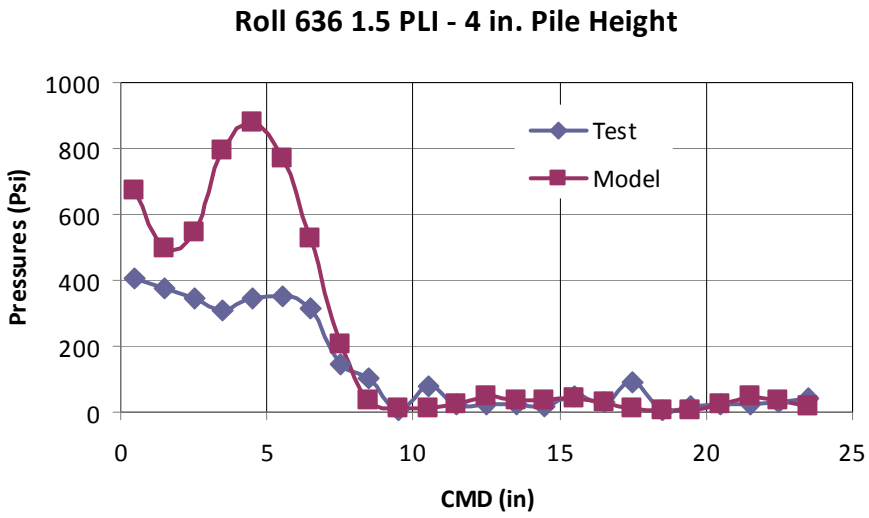

Figure 8.26 Roll 636 1.5 PLI 4 in. P.H. Pressures

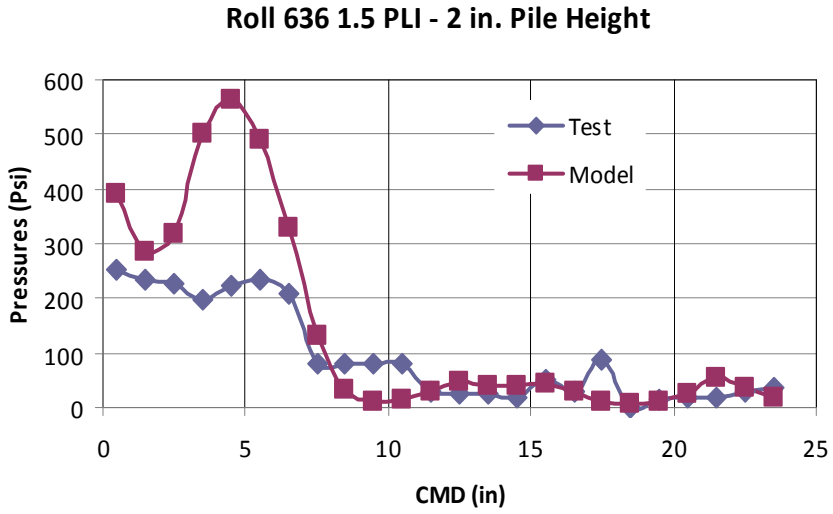

Figure 8.27 Roll 636 1.5 PLI 2 in. P.H. Pressures

We also obtained outer lap radial profile data with a profilometer. We compared these readings with the output of the model.

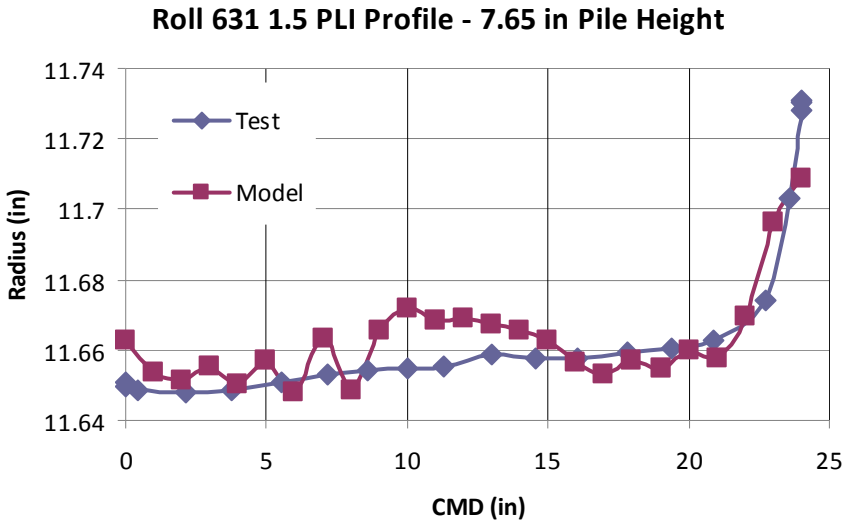

Figure 8.28 Roll 631 1.5 PLI 7.65 in P.H. Roll Profile

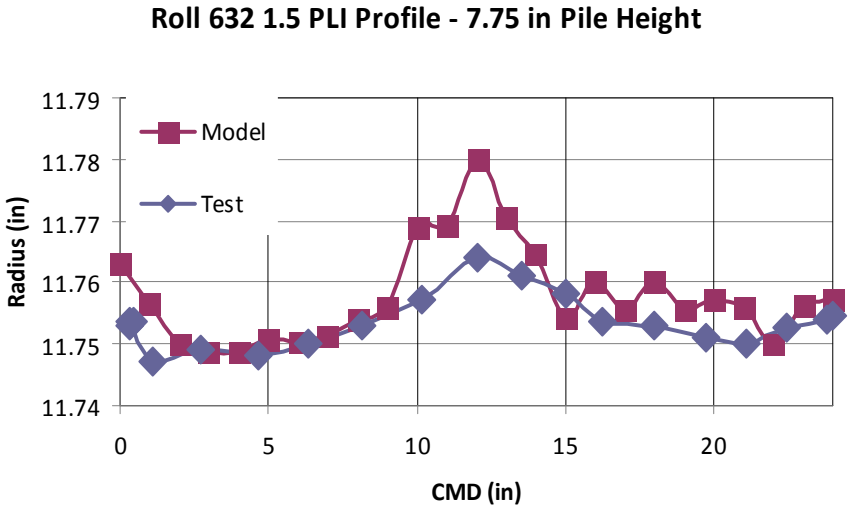

Figure 8.29 Roll 632 1.5 PLI 7.75 in. P.H. Roll Profile

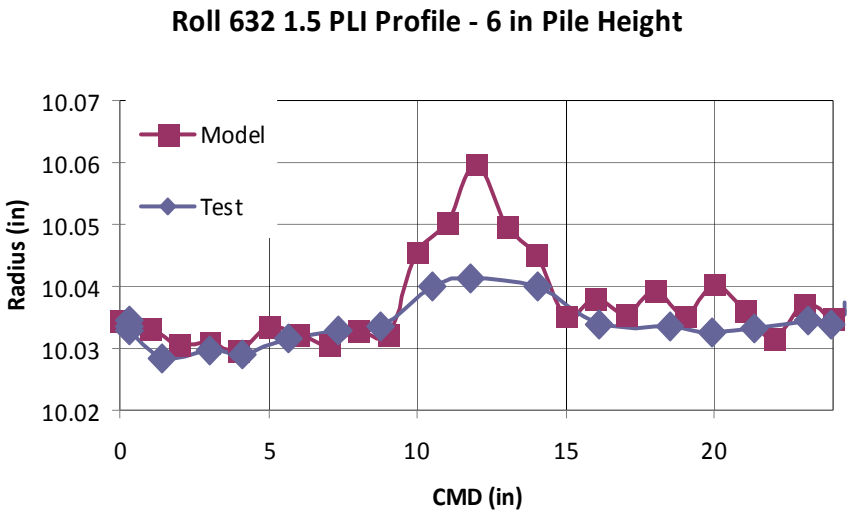

Figure 8.30 Roll 632 1.5 PLI 6 in. P.H. Roll Profile

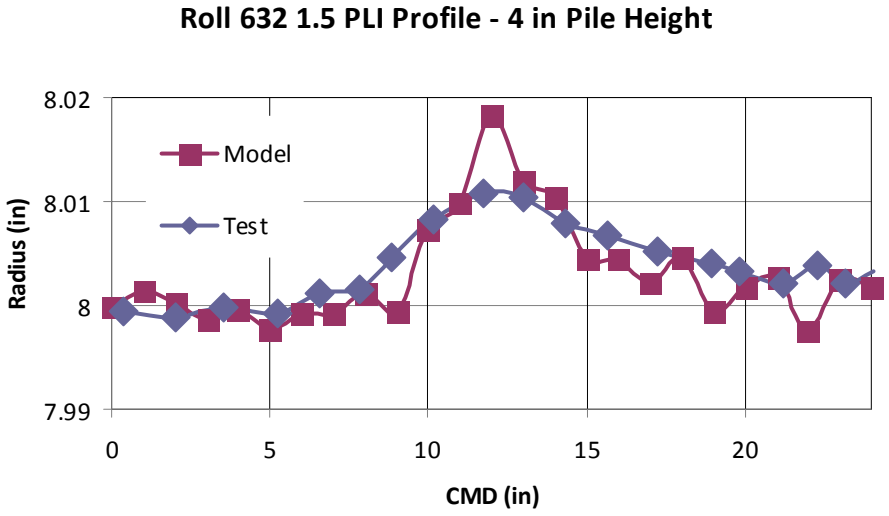

Figure 8.31 Roll 632 1.5 PLI 4 in. P.H. Roll Profile

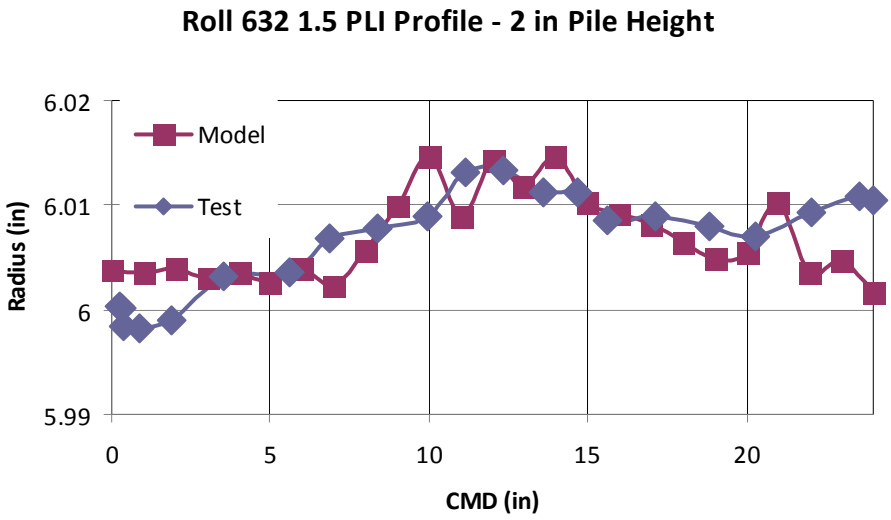

Figure 8.32 Roll 632 1.5 PLI 2 in. P.H. Roll Profile

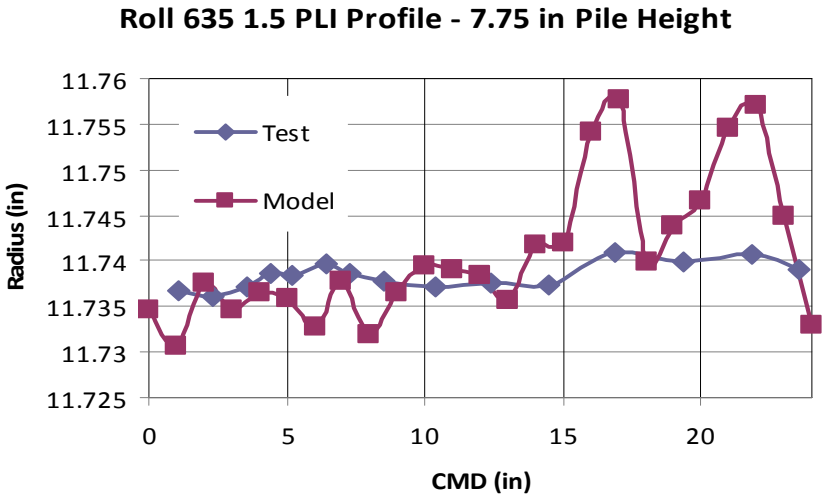

Figure 8.33 Roll 635 1.5 PLI 7.75 in. P.H. Roll Profile

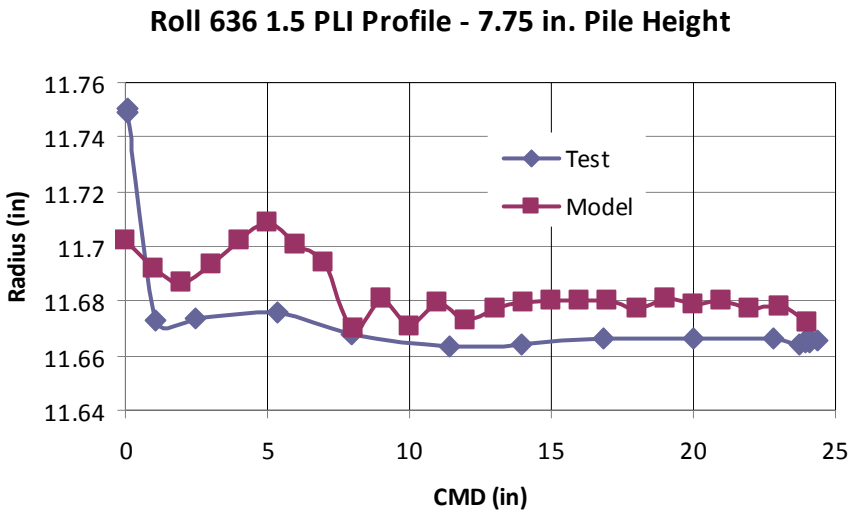

Figure 8.34 Roll 636 1.5 PLI 7.75 in. P.H. Roll Profile

In the second category of tests we center wound rolls with a nip. Now the web line tension was 1.2 PLI and the nip load was 1.33 PLI.

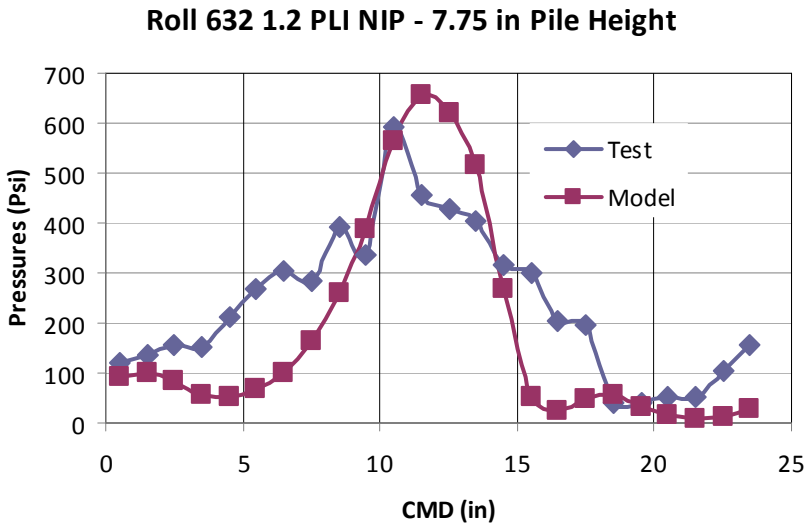

Figure 8.35 Roll 632 1.2 PLI NIP 7.75 P.H. Pressures

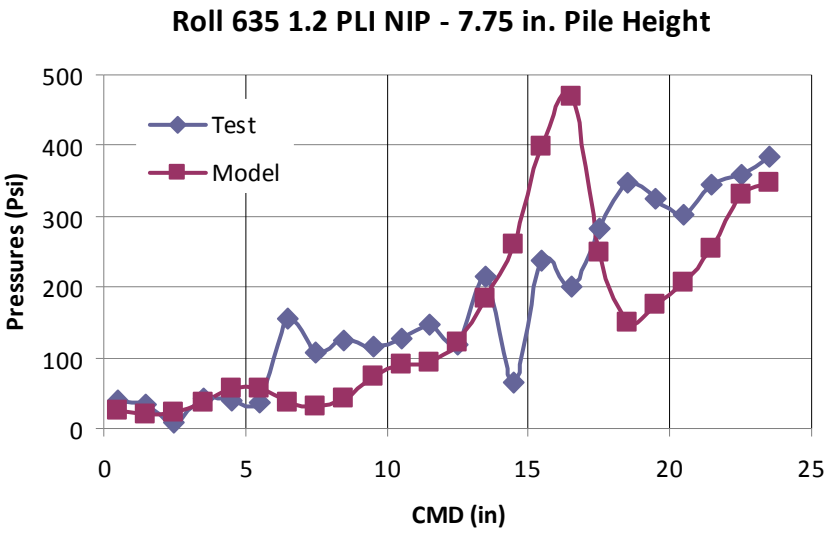

Figure 8.36 Roll 635 1.2 PLI NIP 7.75 P.H. Pressures

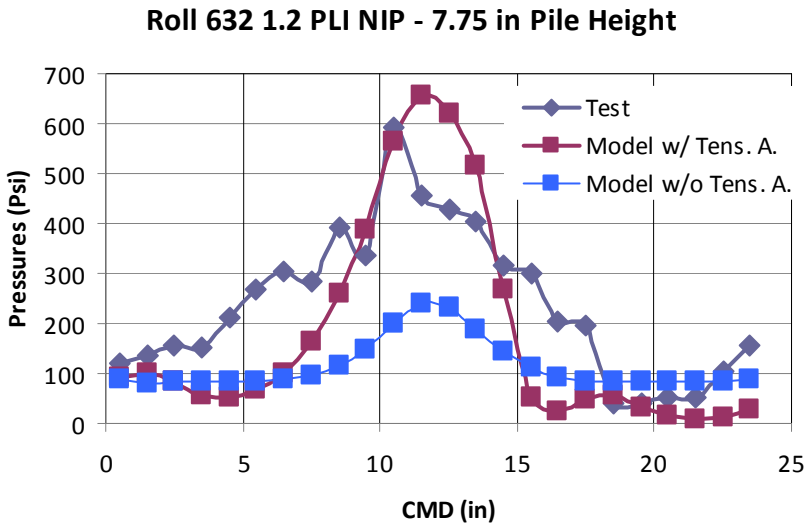

Figure 8.37 Pressure Comparison of Cases w/ and w/o Tension Allocation

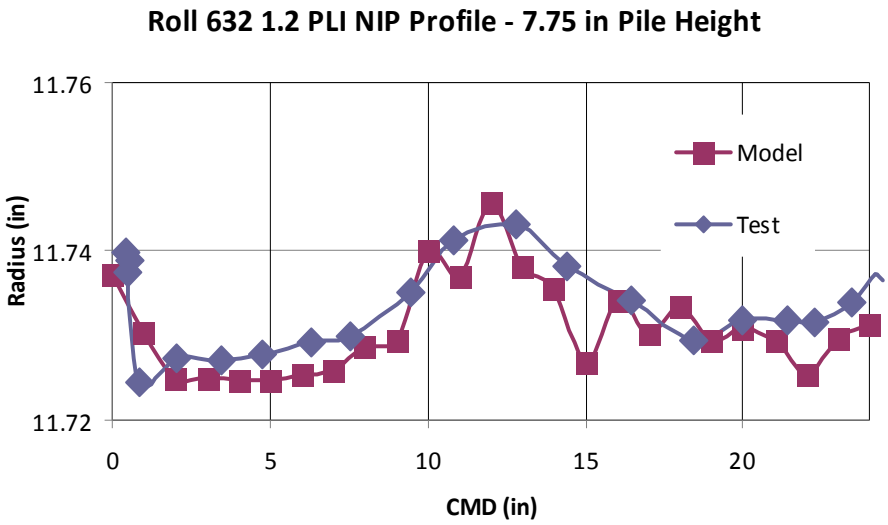

Figure 8.38 Roll 632 1.2 PLI NIP 7.75 in. P.H. Roll Profile

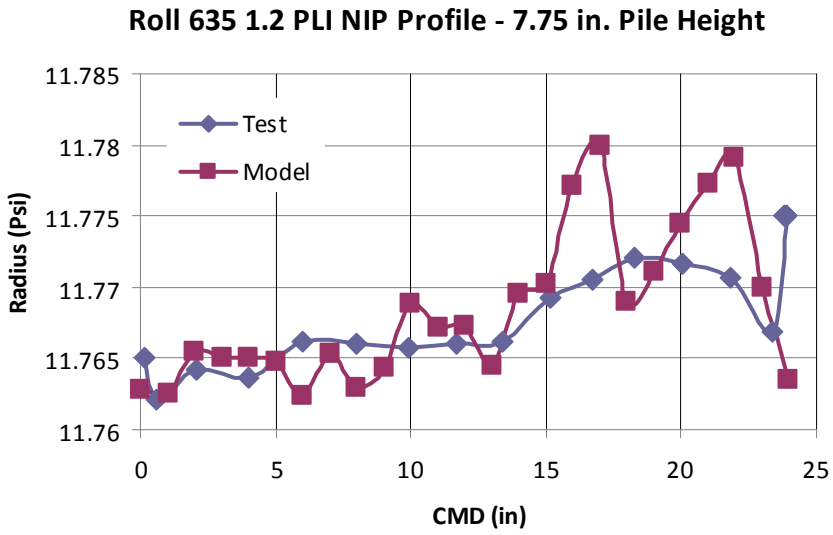

Figure 8.39 Roll 635 1.2 PLI NIP 7.75 in. P.H. Roll Profile

8.4 Discussion

The code is producing core pressure levels for rolls 632 and 635 that agree well with tests. The core pressure patterns are also matching. For the cases with nip engagement, again the pressure levels are close to the experiments and the core pressure patterns are also matching. The profilometer comparisons are also matching. For rolls 631 and 636 which were cut from the edges of the master roll, there are clear deviations from the experimental values at the edges. These deviations can be attributed to the following facts:

- **Sparse Data**: As we mentioned previously, we found that average distance between two consecutive data points is about 2122 inches for the BETA-gage readings. There are 56 scans for the entire length and only 32 of these scans include recorded data. The rest were lost during archiving in the Mitsubishi facility. This means that for every 3 consecutive scans the scan in the middle is lost. This situation increases the average distance between two consecutive data points to 4244 inches. Moreover, for some cases 2 consecutive scans were lost. In this case the average distance between data points increases to 6366 inches.

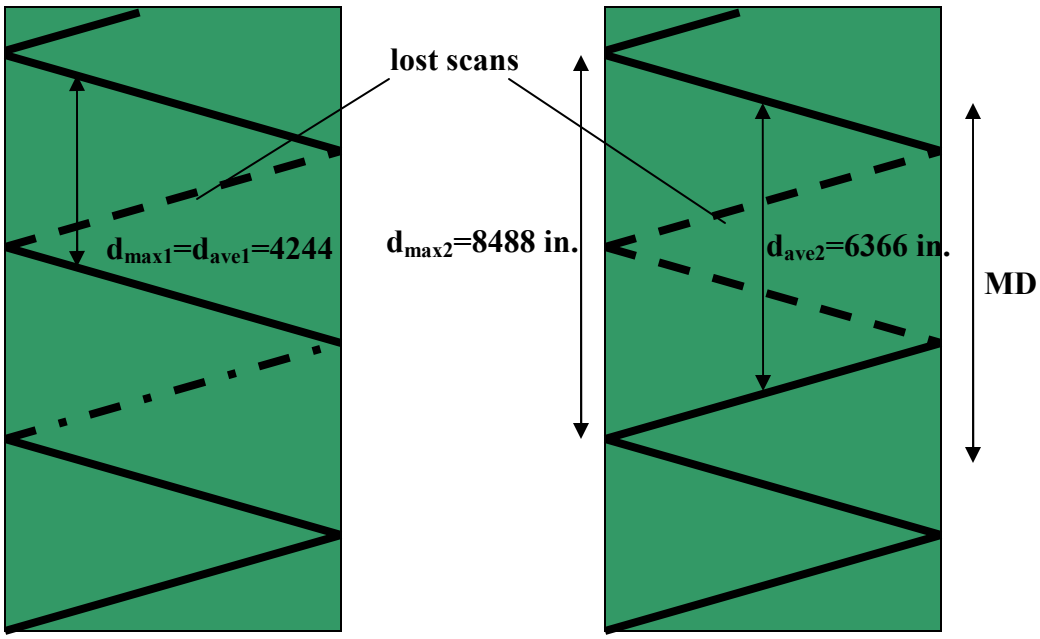

Figure 8.40 Zigzag Data Distances

In this case the maximum distance reaches to 8488 inches (refer figure 8.40). As we mentioned previously the model harvests the BETA-gage data and produces the input data for the code by linear interpolation. Such long distances will certainly induce considerable errors which can affect the results. We also sent strips which were cut from the head and tail sections of the rolls to 3M for an alternative method of thickness measurement. They used capacitance thickness (CT) gauges for measuring the thickness of the strips which were cut along CMD direction. To help explain where these thickness traces were measured refer to figure 8.41:

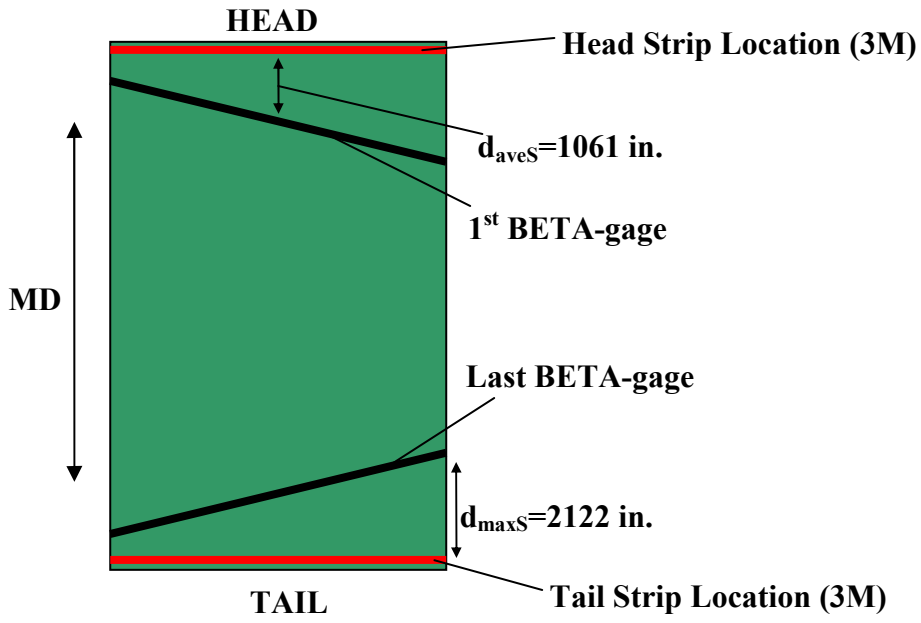

Figure 8.41 3M Specimen Locations

The average distance between the BETA-gage data and the CT-gage data is d_{aveS} = 1061. . In the figures 8.42 and 8.43 head and tail comparisons for roll 631 are shown respectively. When we compare the closest raw BETA-gage (zigzag) data and model's layer thickness (based on closest BETA-gage data for that position) with CT-gage we see from the figures thickness profile changes considerably even for 1061 inches. The situation is same for other cases. So this clearly indicates the effect of thickness data sparsity. As a final measure of sparsity we can also mention the ratio of scanned area to the total web surface. The distance between successive scanning points on a zigzag is 0.27 inches. If we assume continuous scan along zigzag pattern, scanned area can be given by the multiplication of the width of the zigzag (=0.27), number of valid scans (=32) and length of a zigzag

which is 0.27*32*137.23*tan 86.3 ≈ 18350 in^2. The total area is 120000*137.23 ≈ $16.5*10^6$ in^2. The ratio will be %0.1.

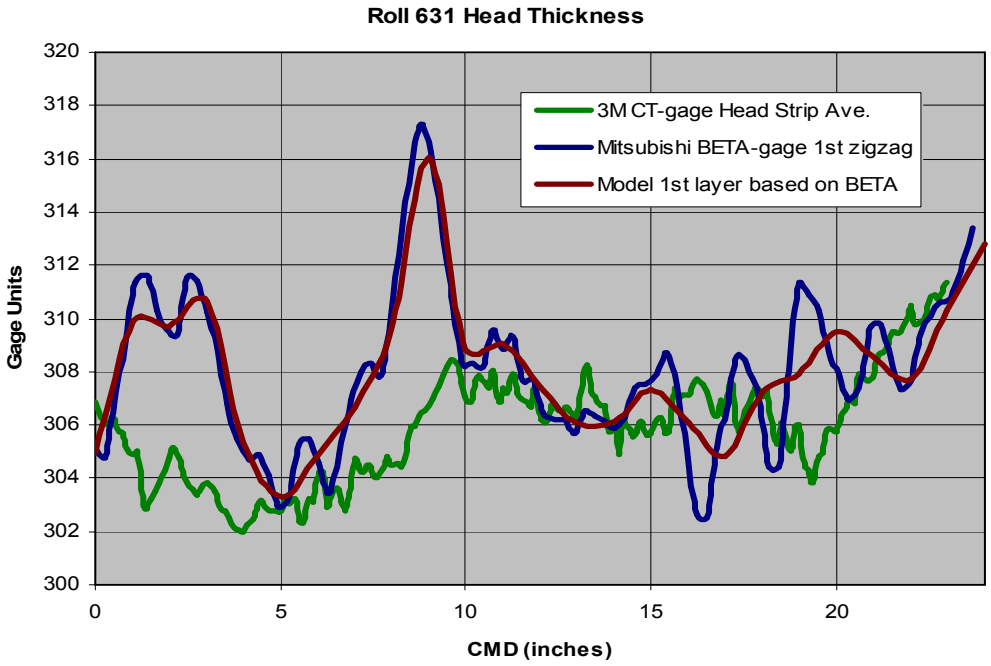

Figure 8.42 Roll 631 Head Thickness Comparison

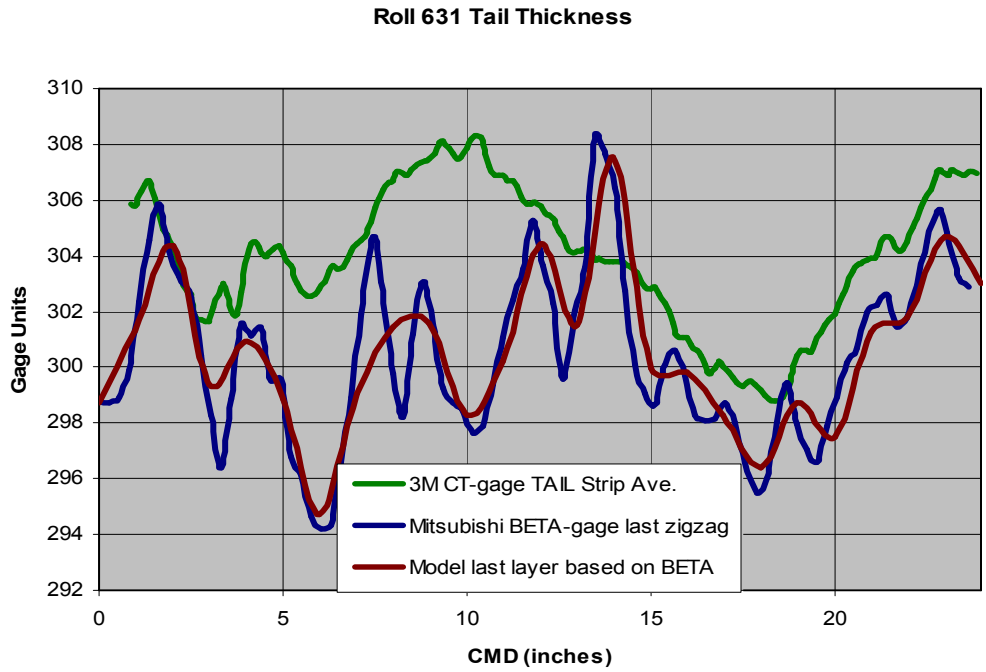

Figure 8.43 Roll 631 Tail Thickness Comparison

- **Radical Thickness Profile and BETA-gage Reliability**: Mitsubishi intentionally produced a very radical web thickness profile. The production machine (extruder) was turned on from cold start position. At the beginning of the production the thickness control systems were left off intentionally. These devices were activated at the one third of the production. At the end, the master roll was also slit with oscillated knifes. All these factors contributed to the very radical and irregular thickness profile. In fact this is such an extreme case it is never allowed in normal production. The average thickness at the head side is greater then the average thickness at the tail side. Also since thickness control system was activated at the one third of the production, tail section is considerably smoother when compared to head section. This property is directly affecting the results. The section which

goes into the roll greatly influences the core pressures. For all cases irregular thicker side (head) was wound first (i.e. winding begun from head).

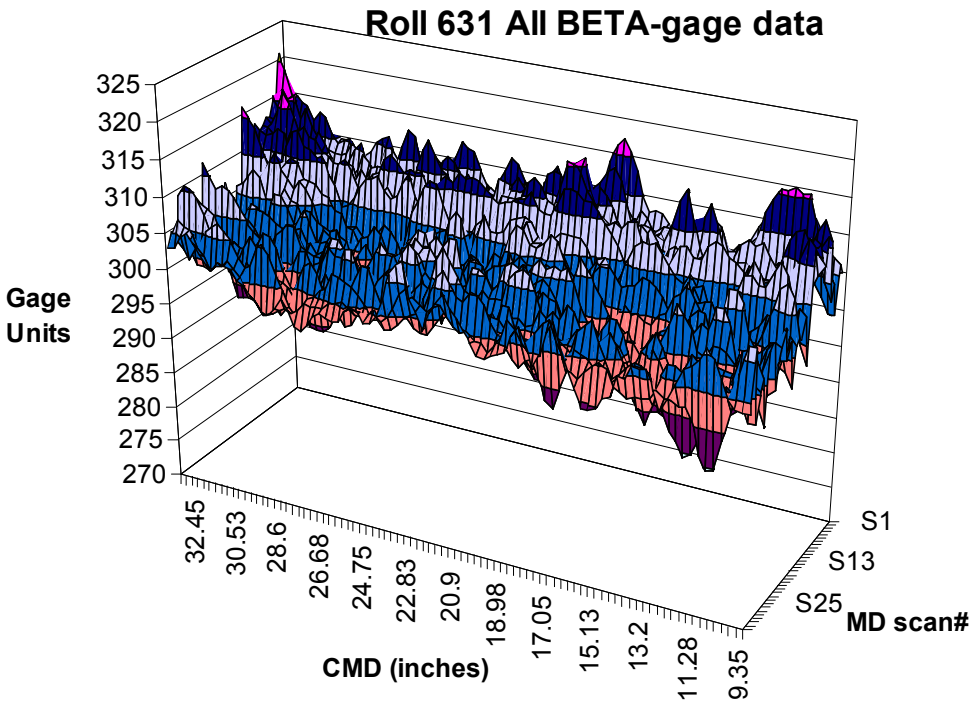

Figure 8.44 Roll 631 All BETA-gage Data

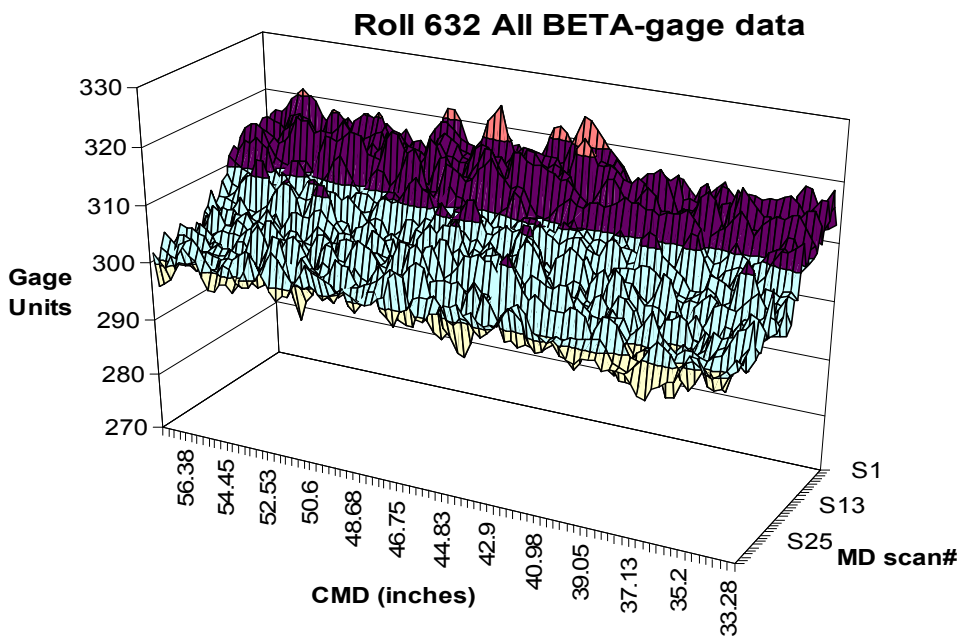

Figure 8.45 Roll 632 All BETA-gage Data

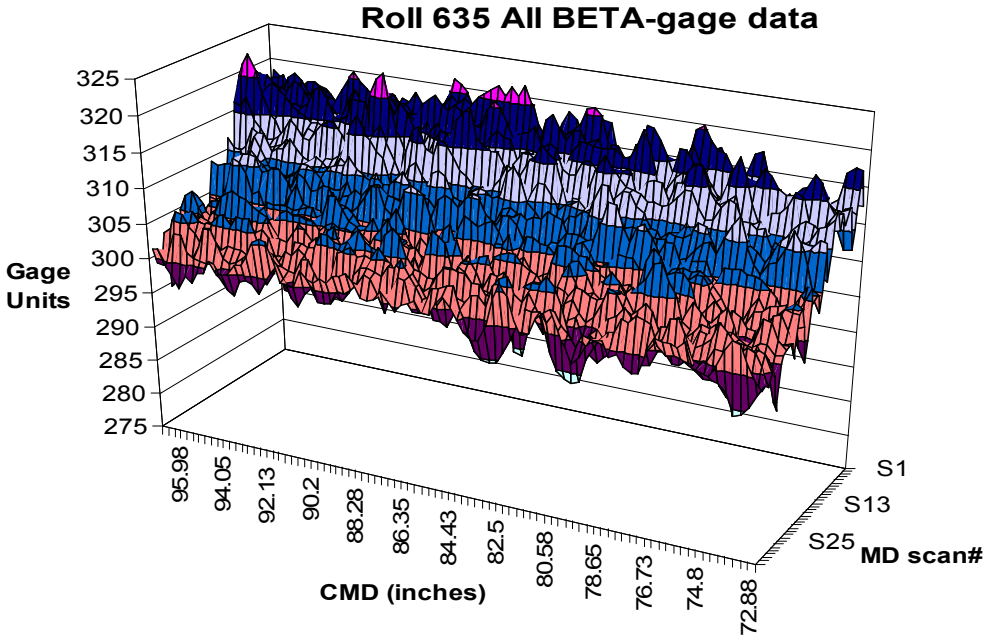

Figure 8.46 Roll 635 All BETA-gage Data

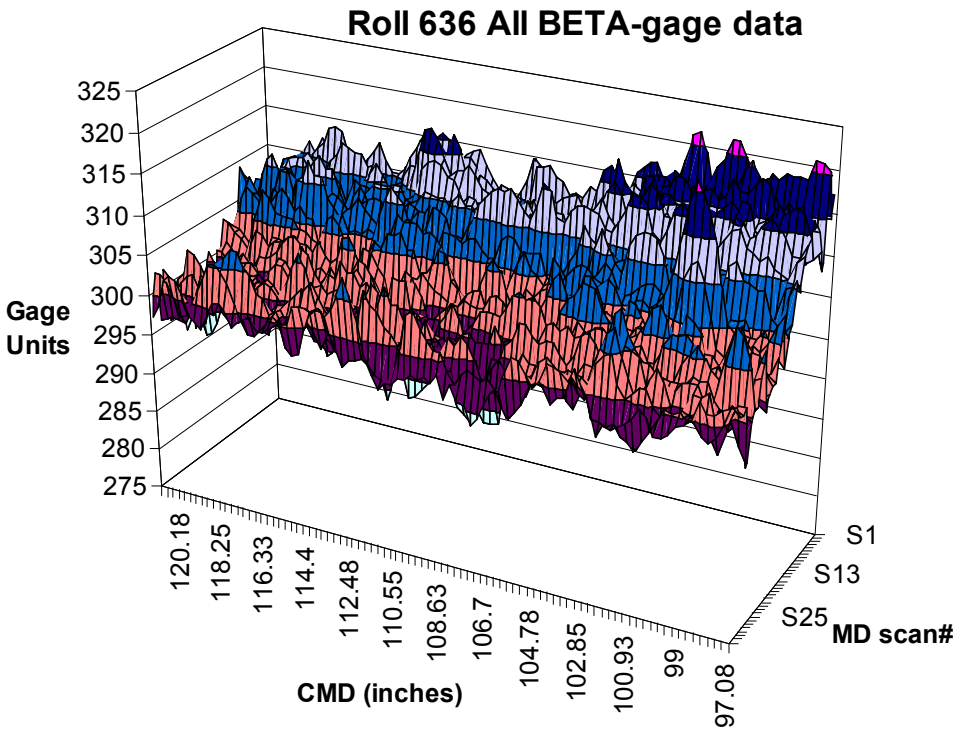

Figure 8.47 Roll 636 All BETA-gage Data

As seen from 3D thickness plots (figure 8.44,45,46,47) problematic rolls 631 and 636 display the most irregular surfaces while the best matching case 632 displays a much smoother thickness profile. Roll 635 is somewhere in between in terms of smoothness as its results are somewhere between the best matching case of roll 632 and problematic rolls 631, 636. Like other measurement methods BETA-gage includes its own errors in measurement. Also as mentioned before, the BETA-

gage is continuously moving across CMD as the web passes through. When the BETA-gage is a measuring very radically changing web thickness and moving surface profile, a lot of detail can be missed. This may explain why roll 632 matches better. As we mentioned previously thickness profile located in the vicinity of core has much greater influence on core pressures. Roll 632 is wound with smoother hence more reliable thickness profile at the beginning.

- **Inelastic Behavior:** During winding we encountered severe raises at the edges of problematic rolls 631 and 636 (figure 8.48). Raises are located at the edges where we are experiencing the biggest difference between model and experimental results. We also observed severe undulations in the web prior to the winder which is winding on these locations (figure 8.49). The radius of these thicker edges are almost 0.2 inches greater than the average roll profile. For a 10 inch diameter roll this indicates 0.02 tangential strain for the web which is winding on those regions. When multiplied with tangential modulus of elasticity of web (= 731000 Psi) the tangential stress allocated to the web at those regions becomes 14600 Psi theoretically. This is well beyond the yield stress of conventional polyester which is somewhere between 8000-10000 Psi. This also explains the undulations. As the material yields its length is increasing without additional tangential stress. Since it is not free (attached to the other elastic portion of web) length increment manifests itself as undulations.

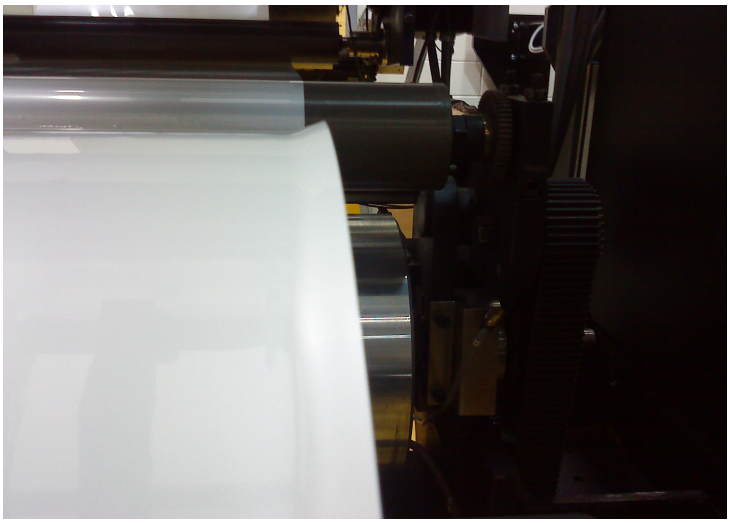

Figure 8.48 Raise at the Edge of Roll 636

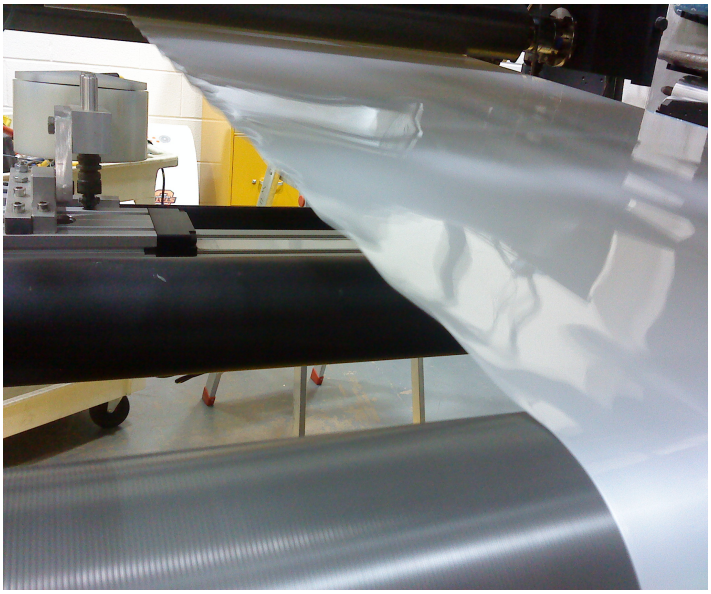

Figure 8.49 Inelastic Ondulations at the Edge of Roll 631

The combined model is not currently capable of performing inelastic analysis in the plane. As it is intended to be a practical (robust, reliable, fast) design tool for industry we are not complicating an already complicated code for this kind of extreme situations. So this is simply out of scope of this study. Nevertheless in an attempt to take into account this matter in a different manner we measured the MD thickness variation. The model is capable of doing simulation with MD thickness variation. Since inelastic behavior induces length variations (ondulations) we measured them and use this data as input in order to take into account the effect of inelasticity. We cut 50 foot long slices and measured their length for length variation characterization (figure 8.50).

Figure 8.50 Sliced Specimen for Length Measurement

Although there is still considerable difference between model and experimental results, situation improved when this data is input to the code. The difference is

because in inelastic behavior energy is not conserved where as in the model it is always conserved. We can demonstrate an ad-hoc solution to this matter by simply reducing the tangential stress to half for these edges (figure 8.51). This time we can see it is matching much better but of course this is not a robust solution based on real inelastic analysis.

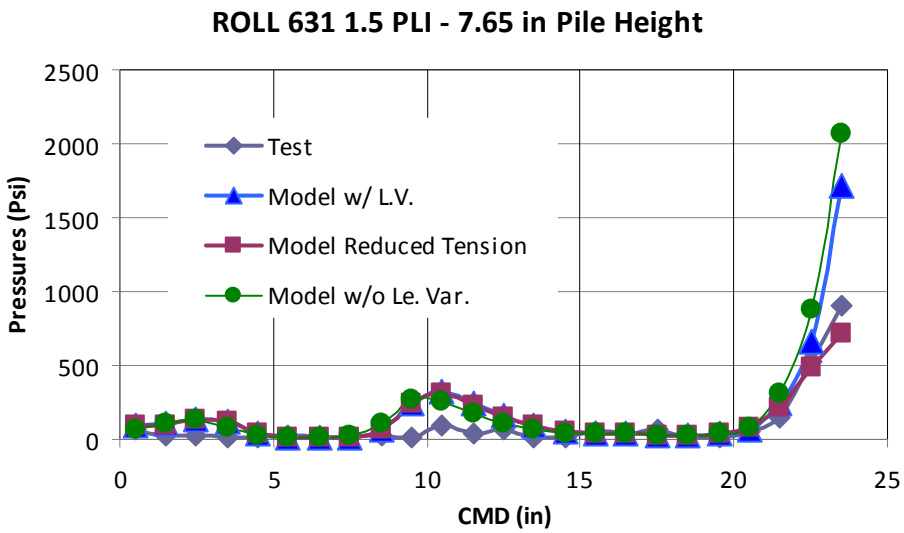

Figure 8.51 Effect of Length Variation and Energy Loss

- **Gapping:** In general, during winding, pressure profile monotonically increases for all locations as the material builds up. During experiments we observed relief in pressures for some locations. This can be attributed to the gapping. Gaps are occurring when layers disengage from each other due to winding and material conditions. Radical thickness profile with oscillation is one of the main causes of gapping. Since the web is oscillated, thicker locations are changing as we wind the material on to the core. Also since the thickness profile is radical irregular roll

profile during winding occurs. All these factors interactively contribute to the formation of gaps. The figure 8.52 explains this phenomenon.

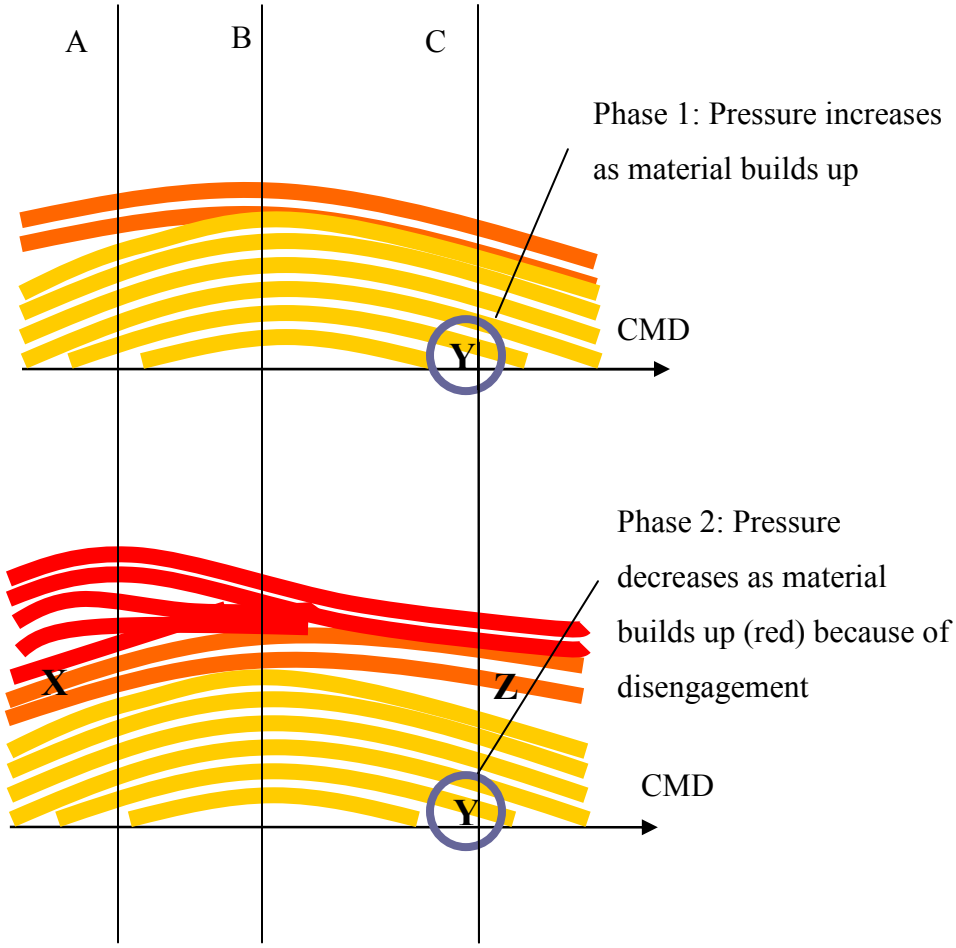

Figure 8.52 Gapping Phenomenon

At the beginning of winding thicker part was around section B. Because of oscillation it is switched to section A. Now as winding continues pressures are rapidly increasing for location X. After a limit, because of considerable bending rigidity for thick materials, pressure around location X may induce a relief in

loading around Z. Hence the pressure increment around location Y which was caused by winding orange layers will significantly reduce. For advanced cases excessive pressure around X may even cause disengagement (gap) around location Z just like a seesaw. If the decrease in pressure is greater than the contribution of the red layers then we will observe the pressure relief in the second phase around location Y as well as a gap will form around Z. In order to model this phenomenon properly we have to introduce gapping property. The current model does not count for gapping as it will greatly increase the complexity and decrease the stability and speed. Gapping is currently out of the scope of this study but we will discuss some aspects of this in chapter 9.

- **Nip Support Conditions:** For the center winding with nip case the model produces pressure profiles which are close to the experimental values. Patterns are also similar but model based pressure profiles have more pronounced and sharper peaks. One important reason for this may be the nip engagement model. The model assumes fully rigid supports for nip beam. But in reality supports will allow some degree of flexibility to the nip. This will affect the engagement order of the various locations on the roll's surface. In turn this will automatically alter the nip induced pressures along CMD because if nip is allowed to rotate to some degree then it will engage with the lower locations also (figure 8.53). This is why the peaks are sharper and higher in the pressure profiles. This feature (elastic supports for nip) is out of scope of this study but we will discuss some aspects in the chapter 9. Another issue is the frequency of the activation of nip engagement subroutine. In the simulations it is not called for all layers because the CPU time

will increase significantly. Instead nip engagement algorithm is called every time after a certain number of laps are wound. This number is user defined and it was set to 20 during calculations. During winding these 20 laps, same spring constants are used. In fact as the material builds up “springs” will became softer and the peaks will deform more. Finally under the same load progressively softened peaks may allow nip to come in contact with lower regions. Hence lower regions will begin to get NIT and pressure profile for those regions will begin to increase.

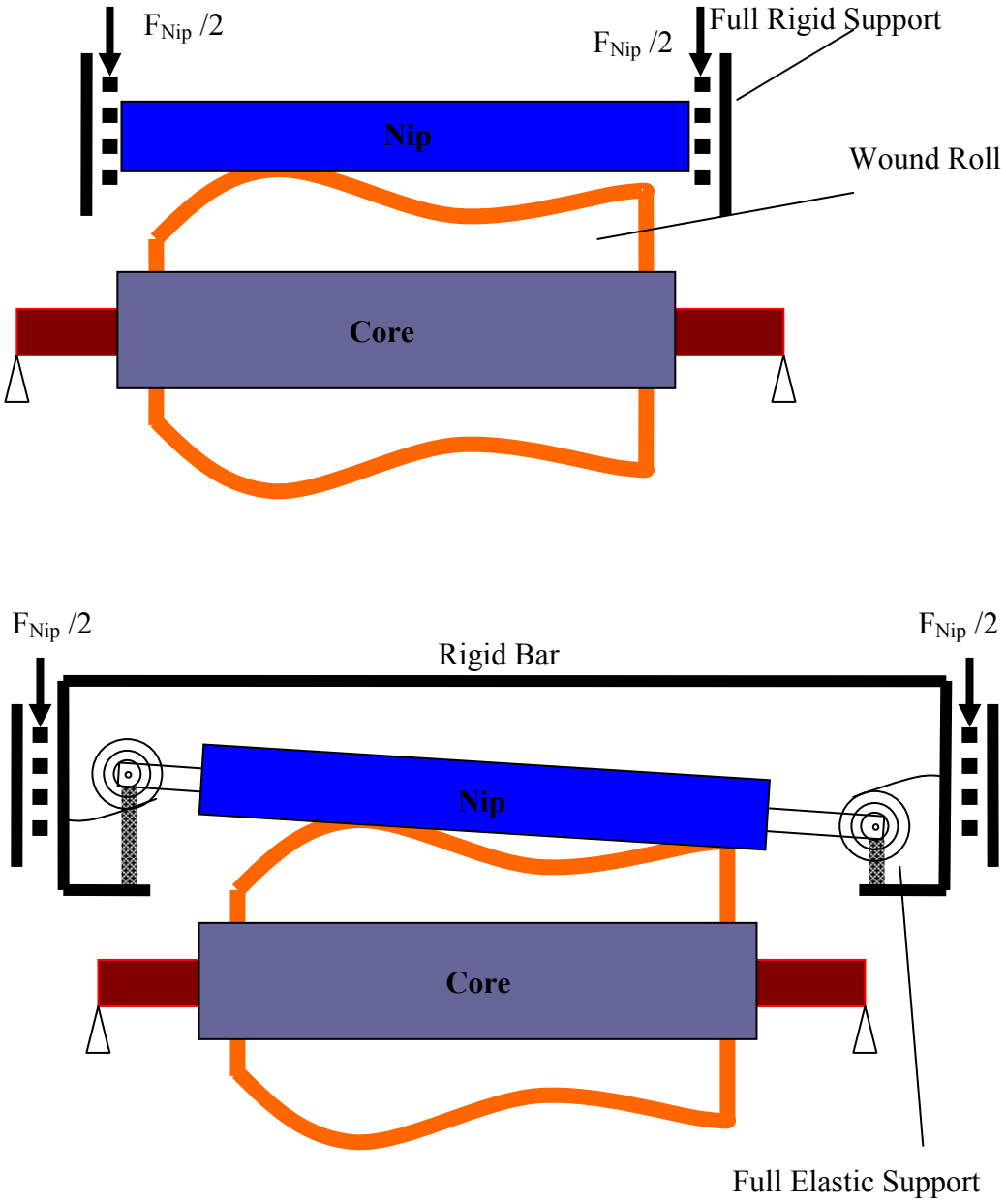

Figure 8.53 Elastic vs. Fixed Support for Nip

8.5 Summary

The current model is composed of three sub-components. The first sub-component is a standalone 2 winding simulation which is tested and verified with the experiments done in the literature [17] (Chapter 4). The second sub-component is the roll compressor model. This is also tested and verified with the experiments done in the literature [39] (Chapter 5). The third component and the less sophisticated one is the nonlinear beam spring model which is extensively tested and verified with the simple cases in the literature (Chapter 6). Briefly the combined model is formed from totally verified sub-components. Extensive testing of the combined model indicated that all sub-components are working in a perfect harmony and no abnormality is occurred.

The combined model produced comparable stress levels and similar stress patterns for the experiments completed here at OSU. The level of agreement for these experiments is inferior to the level of agreement for the experiments done in literature [17]. There are several facts behind this:

- Severely inadequate data for thickness characterization
- Extremely radical and irregular web which is never encountered in normal production.
    - Inelastic behavior which is never intended to be included in the model and beyond the scope of this study.
    - Gapping behavior which is not included in the model and beyond the scope of study.

Nevertheless the combined model produced acceptable results even for these poor conditions as it can be used to predict maximum pressure levels, pressure patterns correctly. We can conclude that given adequate data in normal production conditions combined model shall produce superior results.

9. CONCLUSIONS, FUTURE WORK AND RECOMMENDATIONS

9.1 Summary

The final objective was to develop an efficient, robust and reliable 2D axisymmetric wound roll model including nip effects. During this study the following works are completed towards final objective:

- Limitations of the small strain theory in the winding simulations are investigated. In this context an efficient compact nonlinear axisymmetric finite element model is developed for the geometrical nonlinear analysis of wound rolls. The results are compared with existing linear and nonlinear models and also with experiments. It is found that the small strain based pre-stress formulation is valid for the wound roll models

- An efficient and robust standalone 2D axisymmetric wound model is developed. This model is based on the notion of pre-stress formulation in the small strain conjecture. The results of the model are compared with existing literature and experiments and it is validity is proved.

- The radial stiffness of a wound roll under nip load is investigated. An efficient and robust numerical contact algorithm is developed for the contact of a wound roll and a nip. The formulation is based on the finite element method. The model directly takes into account geometrical and material properties of wound roll and nip. Load versus deformation relations are produced for given material and geometrical parameters. Results are compared with experiments and the model is verified. It is also showed that radii of the contacting cylinders are important in the calculation radial stiffness of wound rolls. Finally it is shown that the load versus deformation relation can be represented with a second order curve fit of the discrete data. The radial spring stiffness is then derived with differentiation of the 2^{nd} order polynomial.

- A contact algorithm which takes into account nonlinear radial character of wound roll and nonuniform roll profile is developed for the calculation of the NIT versus CMD. The contact algorithm is based on the analog beam spring model. In this model the radial stiffness of the wound roll is represented with nonlinear springs. The behavior of the springs is represented with two parameters which are provided by the load versus deformation analysis of thin slices across CMD as explained above. It is shown that the results produced by the model are consistent with the literature.

- The sub-components are brought together such that they are recursively working together as the proposed combined model.

    - In this context the 2D axisymmetrical model is modified so that the WOT

can be input.

  - All three models are modified to produce suitable outputs for each other as shown in figure 7.2.

  - A BETA-gage code which harvested thickness data was implemented within the main model. Once the oscillation amplitude, period and number of scans are known users can directly feed measured raw BETA-gage data into the code.

- The combined model is tested and the results are verified via experiments.

  - A segmented instrumented core similar to the one in the Hakiel's work [17] is constructed and successfully employed in determining the core pressure variation.

  - As in Hakiel [17] the roll profile is measured with a profilometer and the results are compared with the model's output roll profile.

Wound roll simulations play an important roll in industry. A computationally efficient, robust realistic and proven wound roll model including nip effects in 2D would be very useful in understanding stress related defects in production processes. In this study we have composed a wound roll model in to sub components and showed the validity of sub models. The combined model is formed by an integration of these proven sub models and it is also verified via experiments. Hence it is a proven, practical (robust, fast) and capable simulation tool for web handling industry.

9.2 Conclusions

We have come to the following conclusions:

- It is concluded that tension loss is mainly caused by the deformation of the outer surface of the roll. Hence the pre-stress formulation which is implicitly including tension loss phenomenon is valid even for geometrically nonlinear cases.

- The radii of contacting cylinders are important in the determination of the radial stiffness.

- It is found that in the fully wrapping case of the center winding with nip, tension is still mainly allocated due to the roll radius profile. Hence in case of nip engagement the code should always run with tension allocation due to profile (refer figure 8.37).

- The sparsity of the thickness data is important for the modeling of highly irregular and radical webs.

9.3 Future Work and Recommendations

The current model is using almost all available resources of axisymmetric finite element formulation. There are only a few potential research areas that exist in the realm of axisymmetric finite element modeling. Here we will briefly discuss these potential future works.

- **Gapping:** Gapping is the phenomenon of disengagement of layers from each other. As mentioned previously, especially with web materials which are

produced with radical thickness profiles and oscillated during production have tendency for gapping. This because the seesaw type mechanism we described. The current model does not include gapping because it is already very complex and gapping will increase complexity enormously. First of all in order to allow gapping we have to separate radial degrees of freedoms between model layers. This automatically doubles the number of unknown variables. The most time consuming task is solution of the finite elements equations. If there are n unknowns solving the linear system requires $O(n^3)$ flops. If we are doing a cyclic operation like winding simulation then we should solve for $O(1^3+2^3+\ldots+n^3)$ times. This is $O(n^4)$ flops. Hence doubling n means quadrupling the CPU time at the beginning. Moreover stability issues will arise. At every turn a separate iteration must be carried out for gapping control. If there is a gap forming somewhere, degrees of freedoms should be unlocked at that location. If an existing gap is closing corresponding degrees of freedoms should be locked. A very robust gap monitoring algorithm should be employed for properly carrying out these operations. It is not an easy task because the tolerance limits for overlapping regions and voids which should prevent infinite looping for gapping iteration is not known a priori.

- **Faster Roll Compression Models:** The Current model employs 2D nonlinear finite elements for the calculation of spring stiffness for each sector. This takes considerable amount of time in the center winding with nip analyses. A faster method can be employed for sector radial stiffness calculations. We have tried Evans's [42] simple approach but this is proven to yield poor results. Evan's

modeled contact of a tire with a flat surface. He simply assumed that the contact pressure is hydrostatically applied to tire's circumference. Thus he reduced a local contact problem to a well known simple axisymmetrical problem.

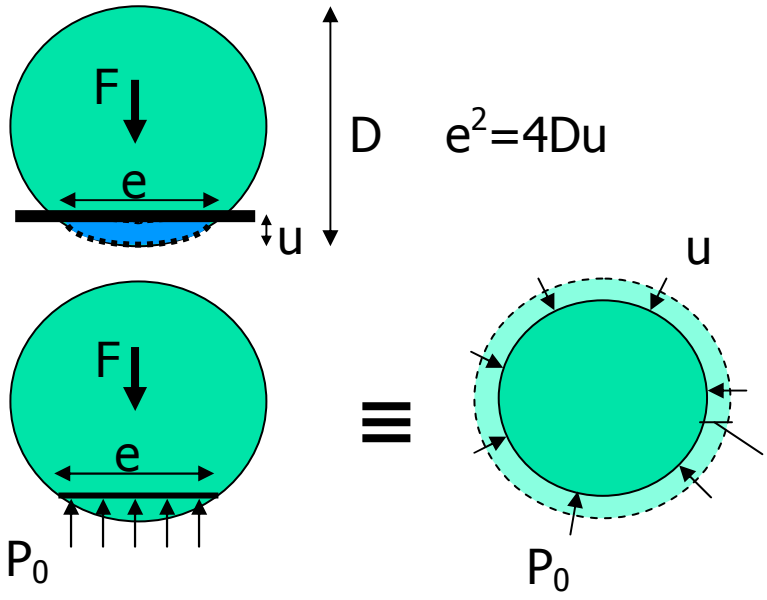

Figure 9.1 Evans Compression Model

We have adopted this approach and implemented a code taking into account material nonlinearity of wound rolls. But apparently after a level of compressive load this simplistic method deviates from the proven 2D FE solution. This may be due to width of contact (e) calculations which are based on linear elastic assumptions. Another potential method would be forming a table which can be used to interpolate for stiffness terms. At the beginning roll compressor code will

run a series of cases with some predefined values of web line tension, roll radius and any other important parameter and will form the table with the corresponding spring stiffness. During winding analysis, instead of running roll compressor code for every sector again, the code will simply use the interpolated values for spring stiffness due to the current parameters.

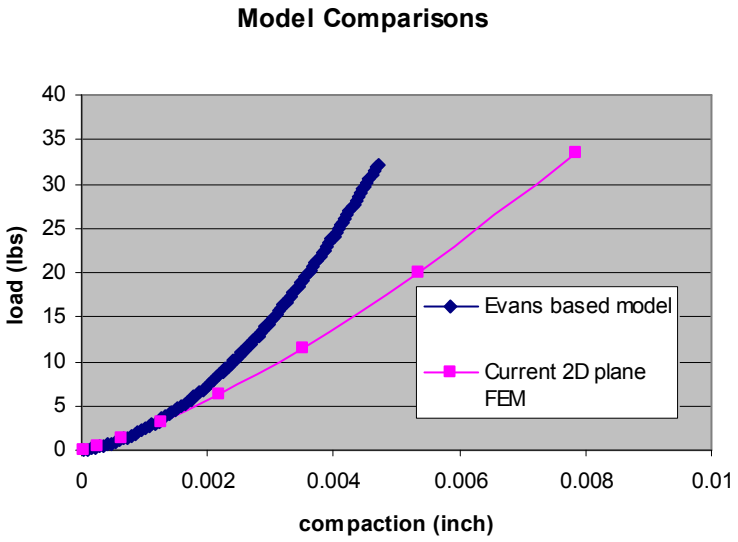

Figure 9.2 Evans vs. Current Compression Model

- **Nip Support Conditions:** As we mentioned earlier the current code assumes rigid supports for the nip beam where as in reality it has some degree of freedom. Flexibility can be introduced such that when nip beam makes contact with the peak locations of wound roll surface it may turn and make contact with another lower location also. This extent of this turning is due to the flexibility of the nip support conditions.

- **Overall Superior Performance:** Solving system of linear equations takes the lion's share from the CPU time. We are currently using a symmetric band solver based on Gauss elimination. Since winding simulation is done layer by layer and for every layer a similar displacement vector is seek one may employ iterative methods. These methods are especially advantageous if the iteration is started from position which is close to actual solution. This may greatly increase the overall performance of the model.

BIBLIOGRAPHY

1. Gutterman, R.P. *Theoretical and Practical Studies of Magnetic Tape Winding tensions and Environmental Roll Stability*. U.S. Contract No. DA-18-119-SC-42, 1959

2. Catlow, M.G. and Walls, G.W. *A Study of Stress Distribution in Pirns*. J. of textile Institute part 3, ppT410-429,1962

3. Pfeiffer, J.D. *Internal Pressures in a Wound Roll of Paper.* Tappi Journal, Vol. 49, No. 8, pp. 342-347, August 1966.

4. Altmann, H.C *Formulas for Computing the Stresses in Center-Wound Rolls.* Tappi Journal, Vol. 51, No. 4, pp. 176-179, April 1968

5. Yagoda, H.P. *Resolution of a Core Problem in Wound Rolls.* Transactions of Asme, Journal of Applied Mechanics, Vol. 47, pp.847-854, 1980.

6. Burns, S.J., Richard, R.M., Lambropoulos, J.C. *Strain-based Formulas for Stresses in Profiled Center-wound Rolls*. Tappi Journal, Vol. 82, No. 7, July 1997

7. Mollamahmutoglu C. *A Novel Algorithm for Predicting Internal Stresses in 2D Axis-symmetrical Wound Roll Models.* Preliminary Exam Thesis, Mech&Aero. Eng. Department, OSU, Jan 2007.

8. Hakiel, Z., *Nonlinear Model for Wound Roll Stresses.* Tappi Journal, Vol. 70, No. 5, pp. 113-117, May 1980.

9. Good J.K. and Pfeiffer, J.D. *Tension Losses During Centerwinding.* Proceedings of the 1992 Tappi Finishing and Converting Conference, pp. 297-306.

10. Benson, R.C. *A Nonlinear Wound Roll Model Allowing for Large Deformation.* Transaction of Asme, Journal of Applied Mechanics, Vol. 62, pp. 853-859, December 1995.

11. Qualls W.R. ,Good J.K. *An Orthotropic Viscoelastic Winding Model Including a Nonlinear Radial Stiffness*. Transactions of Asme, Journal of Applied Mechanics, Vol. 64(1), pp.201-208, Mar 1997.

12. Qualls W.R. ,Good J.K. *Thermal Analysis of a Round Roll*. Transactions of Asme, Journal of Applied Mechanics, Vol. 64(4), pp.871-876, Dec 1997.

13. Good J.K. Holmberg M.W. *The Effect of Air Entrainment in Centerwound Rolls.* Proceedings of the Second International Conference on Web Handling, pp.246-263, 1993.

14. Good J.K. Wu Z. Fikes M.W.R. *The Internal Stresses in Wound Rolls with the Presence of a Nip Roller*. Transactions of Asme, Journal of Applied Mechanics, Vol.61, pp. 182-185, 1992.

15. Olsen J.E. *On the Effect of Centrifugal Force on Winding.* Tappi Journal, Vol. 78, No.7, pp. 191-195, July 1995.

16. Yagoda H.P. *Centrifugally Induced Stresses within Center Wound Rolls – Part I.*

Mechanics Research Communications Vol. 7, No. 3, pp. 181-193, Part I, 1980.

17. Cole A. K. Hakiel Z. *A Nonlinear Wound Roll Stress Model Accounting for Widthwise Web Thickness Nonuniformities*. Asme, Applied Mechanics Division, Vol. 149, 1992.

18. Kedl D.M. *Using A two Dimensional Winding Model to Predict Wound Roll Stresses that Occur Du to Circumferential Steps in Core Diameter or to Cross-Web Caliper Variation.* Proceedings of the First International Conference on Web Handling, pp. 99-112, 1991.

19. Lee Y.M. Wickert J.A. Stress *Field in Finite Width Axisymmetric Wound Rolls.* Transactions of Asme, Journal of Applied Mechanics, Vol. 69, pp. 130-138, March 2002.

20. Hoffecker P. Good J.K. *Tension Allocation in Three Dimensional Axisymmetric Wound Roll Model*. Proceedings of the Eighth International Conference on Web Handling, pp.246-263, 2005.

21. Arola, K. and von Hertzen R. *Two Dimensional Axisymmetric Winding Model for Finite Deformation.* Computational Mechanics, Vol. 40, pp. 933-947, 2007.

22. Good J. K. *The Abilities and Inabilities of Wound Roll Models to Predict Winding Defects.* IWEB 2005. Keynote Presentation. Oklahoma S. U. 2005

23. Pfeiffer, J.D. *Nip Forces and Their Effect on Wound-in Tension.* Tappi Journal, Vol. 60, Issue 2, pp. 115-117, 1977.

24. Rand, T. and Eriksson, L.G. *Physical Properties of Newsprint Rolls during*

Winding. Tappi Journal, vol. 56, pp. 153-156, 1973.

25. Good, J.K. and Wu, Z. *The Mechanism of Nip Induced Tension in Wound Rolls.* Transaction of Asme, Journal of Applied Mechanics, vol. 60, pp. 942-947, 1993

26. Good, J.K. Modeling *Nip Induced Tension in Wound Rolls.* Proceedings of the Sixth International Conference on Web Handling, Web Handling Research Center, Oklahoma State University, Stillwater, Oklahoma, pp. 280-284, 2002.

27. Jorkoma, M. *Contact Mechanical Model for Winding Nip.* Doctoral Thesis, Helsinki University of Technology, 2001.

28. Balaji K.K. *The Development of Wound-on-Tension in Webs Wound into Rolls*. PhD Dissertation Oklahoma State University, July 2006.

29. Good. J.K., Pfeiffer. J.D., Giachetto. R.M. *Losses in Wound-On Tension in the Centerwinding of Wound Rolls.* Proceedings of the Web Handling Symposium, Asme Applied Mechanics Div., Vol. 149, pp. 1-12,1992.

30. Hoffecker P. *Analysis of Nip Impinged Three Dimensional Wound Roll*. PhD Dissertation, Oklahoma State University, May 2006.

31. Johnson K.L., *Contact Mechanics*. Cambridge University Press, 1985

32. Belytschko. T., Liu W.K., Moran B. *Nonlinear Finite Elements for Continua and Structures.* John Wiley&Sons, Ltd., 2000.

33. Bathe K.J., *Finite Element Procedures.* Prentice Hall, Inc. 1996.

34. Chandrupatla T.R. and Belegundu A.D., *Introduction to Finite Elements in*

Engineering, Prentice Hall, Inc.,2002

35. Reddy J.N., *An Introduction to Finite Element Method* McGraw-Hill Education, 3rd Ed. 2005

36. Bhatti M.A., *Advanced Topics in Finite Element Analysis of Structures:With Mathematica and MATLAB Computations.* Wiley,1st Ed. 2006.

37. Mollamahmutoglu C. and Good J.K. *Axisymmetric Wound Roll Models*, Proceedings of 10th International Web Handling Conference, Oklahoma State University, 2009.

38. Mollamahmutoglu C. and Good J.K. *Fully Nonlinear Wound Roll Model* Proceedings of 10th International Web Handling Conference, Oklahoma State University, 2009.

39. Ganapathi S., *Diametral Compression of Wound Rolls with State Dependent Properties*, Ms Thesis, Mechanical Eng., Oklahoma State University, 2007.

40. Wriggers P., *Computational Contact Mechanics*, Springer-Verlag, 2006.

41. Zhong Z., *Finite Element Procedures for Contact-Impact Problems*, Oxford University Press. 1993.

42. Evans I., *The Rolling Resistance of a Whell with A Solid Rubber Tyre*, British Journal of Applied Physics, vol. 5, pp. 187-188, May 1954.

VITA

Cagri Mollamahmutoglu

Candidate for the Degree of Doctor of Philosophy

Thesis: A 2D AXIS-SYMMETRIC WOUND ROLL MODEL INCLUDING NIP EFFECTS

Major Field: Mechanical Engineering

Biographical:

Education: Received Bachelor of Science Degree in Civil Engineering from Istanbul Technical University, Turkey, 2002. Received Master of Science Degree in Civil Engineering from Istanbul Technical University, Turkey in 2005. Completed the requirements for the Doctor of Philosophy in Mechanical Engineering at Oklahoma State University , Stillwater, Oklahoma in December,2009.

Experience: Employed by School of Mechanical and Aerospace Engineering, Oklahoma State University, Stillwater, Oklahoma, as a graduate research assistant since August 2005.

Name: Cagri Mollamahmutoglu Date of Degree: December, 2009

Institution: Oklahoma State University Location: Stillwater, Oklahoma

Title of Study: A 2D AXIS-SYMMETRIC WOUND ROLL MODEL INCLUDING NIP EFFECTS

Pages in Study: 199 Candidate for Doctor of Philosophy

Major Field: Mechanical Engineering

Scope and Method of Study: A 2D axis-symmetric wound roll model including nip effects which is based on a pre-stress finite element analysis has been developed. The combined model consists of three interactive sub-models. In the first sub-model the notion of pre-stress has been utilized to incorporate web line tension as a source of load. The pre-stress formulation allows easy allocation of web line tension in case of CMD thickness nonuniformities. In the second sub-model a roll compression algorithm has been developed via 2D plane finite elements. The roll compression model was used to characterize radial stiffness of the wound roll in the third sub model at various CMD positions. The third sub-model represents the roll and nip contact as a 2D beam spring contact and solves for the nip induced pressures along the CMD. Finally these nip induced pressures were used in the first sub-model in the wound-on tension calculation. This cyclic process between sub-models continues till simulation ends. The model is compared with existing literature and the tests completed at the WHRC of OSU. A segmented instrumented core is constructed and the core pressures were obtained for a polyester web of known thickness variation.

Finding and Conclusions: The Pre-stress formulation was shown to be adequate even for highly compressible materials by comparing with Benson's and Good's model, and Good's experiment. Validity of the pre-stress formulation in 2D wound roll modeling is shown by comparing with Hakiel's model and experiment. It is found that even for high nip wrap angles the roll profile still dominates tension allocation. Roll contact analysis showed that radii of contacting cylinders are important in stiffness calculations. It is shown that thickness data sparsity is important for the modeling of highly irregular and radical webs. Finally it is concluded that the combined model can be used to predict maximum pressure levels and pressure patterns correctly even for poor thickness data.

ADVISER'S APROVAL: Dr. James K. Good